University of Groningen

Master Research Project

MSc Mechanical Engineering

Scaling Effects and Validation of the Ocean Grazer Experimental Wave Tank using CFD

Author:
E.E. Berends
S3261484

Supervisors:
Prof. dr. A.Vakis
Drs. W. Prins

July 9, 2021

Abstract

The goal of this thesis was to investigate whether the Ocean Grazer experimental wave tank can create adequate environments for future testing and validation experiments. The research was performed by developing a full-scale numerical model of the experimental wave tank in OpenFOAM. The study focuses on the observed average wave amplitude and reflection. Multiple cases are presented to investigate the spectrum of waves that is able to be generated, as well as methods to mitigate the reflection at the beach of the wave tank. One of the main findings was that the wave tank was found to be too shallow to generate relevant deep water waves. Its beach was found to be too short for optimal wave absorption for long waves. Furthermore, a partial standing wave was observed to form in every generated wave case as the most dominant form of reflection. The wavelength of the partial standing wave was found to be half the generated waves' wavelength. It was found that the reflection suppresses the average wave amplitude and that the reflection was found to be wave specific and dependent on the wavelength. However, the ability to mitigate the reflection was shown by the implementation of foam layers. The reflection was shown to reduce dramatically, increasing the average wave height. Denser and thicker foams were shown to perform best. Finally, some recommendations were made to improve the performance of the wave tank for future validation and testing experiments.

Acknowledgements

First of all, I would like to thank professor Jayawardhana for making me enthusiastic for the Ocean Grazer and bringing me in touch with the research group and company. I think the Ocean Grazer is a great innovation with large potential.
I would also like to thank professor Vakis and Wout for the opportunity to perform this research and the supervision during my project. The communication and discussion were always relevant, efficient and helpful. Many thanks also to the other members of the Ocean Grazer group for the constructive feedback and fruitful discussions. Thanks in particular to Emiel for the discussion on CFD, as well as off topic conversations during coffee breaks.

Contents

1 Introduction

1.1 Ocean Grazer

The Ocean Grazer is a novel approach to contributing to the energy transition [1]. The Ocean Grazer uses an innovative approach to exploit the abundance of energy present in ocean surface waves in order to harvest and store large amounts of energy. The energy is stored on-site in the form of water with a high potential energy, utilizing proven hydro dam technology. The potential energy can be converted into electrical energy at any time. This enables the ability to match supply and demand, which is one of the major challenges in the energy transition [2]. The working principle of the Ocean Grazer is further elaborated on in the next subsection. The Ocean Grazer is divided into two organisations that work together in close cooperation. At its foundation is the Ocean Grazer research group located at the University of Groningen, led by prof. dr. A. Vakis and drs. W. Prins, as well as prof. dr. ir. B. Jayawardhana. Here, the original concept of the Ocean Grazer was invented and the fundamental knowledge and underlying models are being developed and validated. The Ocean Grazer BV company is a spin-off from the university, aiming to commercialize the innovative technology and increase exposure in order to increase the awareness and support base for the project on a larger scale.

1.2 Working Principle

The main idea behind the Ocean Grazer is to convert the kinetic energy present in off-shore ocean waves into stored potential energy in a volume of fluid. This is done by so-called Wave Energy Converters (WECs). In the Ocean Grazer, the WEC system consists of a set of floaters that float on the surface of the ocean. Incoming waves displace the floaters in the vertical direction. The floater utilizes the vertical motion to displace a volume of fluid from one reservoir to a reservoir with a higher potential energy. The potential energy that is stored can be converted into electrical energy on demand by releasing the fluid through a set of turbines.

1.3 Ocean Grazer 3.0

The current design of the Ocean Grazer is called version 3.0. This design includes a modular approach to combine other off-shore energy harvesting technologies with the Ocean Grazer and its storage application. Figure 1 shows an illustration of the Ocean Grazer 3.0 concept design. Note that in this design the foundation is attached to the ocean floor. The line on which the floaters are positioned indicates the water surface. The main components of the Ocean Grazer are labelled:

1. Floaters
2. Foundation
3. Connection between Floaters and internal system
4. Solid internal reservoir
5. Pumping system between reservoirs
6. Flexible external reservoir
7. Turbine between reservoirs

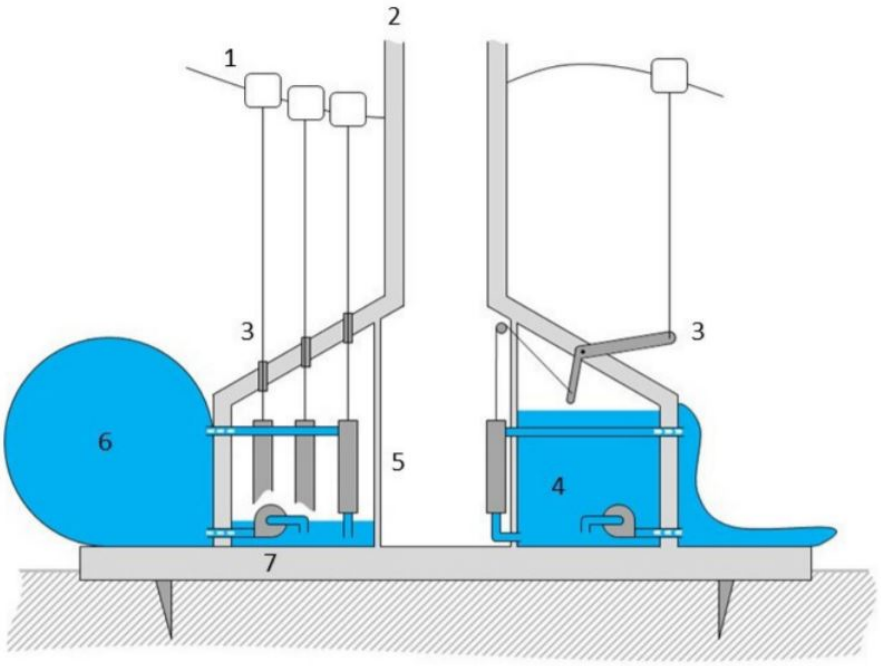

Figure 1: The main components in the Ocean Grazer 3.0 concept design [3].

The array of floaters is designed to capture the wave motion in the vertical direction. The motion is then transferred to the internal system using a set of connectors which translate the motion to the internal pumping system. This system is denoted as the set of Wave Energy Converters (WECs). For every floater, a pumping system is present. The internal system is integrated into the foundation of the Ocean Grazer, which may share its foundation with other energy harvesting technologies such as windmills. The internal reservoir is filled with a certain working fluid and is connected to the atmosphere such that inside the pressure is always atmospheric. In the WECs, the pumping system utilizes the motion of the floaters to pump the working fluid from the internal solid reservoir to the external flexible reservoir. The external reservoir is flexible, such that it inflates when it is filled. There is a large pressure difference between both reservoirs, since the internal reservoir is at atmospheric pressure and the external flexible reservoir feels the hydrostatic pressure of the water column above it. Therefore, a large amount of potential energy is stored in the working fluid in the external reservoir. When there is an electricity demand, the flexible bladder can be deflated, allowing the fluid to flow from the external reservoir to the internal reservoir through a turbine. The turbine harvests the energy from the fluid and converts it into electrical energy.

2 Problem definition

2.1 Problem context

The Ocean Grazer is an innovative approach to harvesting and storage of sustainable energy. Currently (July 2021), the Ocean Grazer is still in the development phase. In order to maximize the energy extraction of the Ocean Grazer by wave energy conversion, it is important to understand the hydrodynamic behaviour of the floater array in different configurations and with different technical parameters for extraction in different oceanic environments. Theoretical and numerical models have already been

developed and are currently still being developed and optimized. However, the (preliminary) results of these models require empirical validation. Full scale experiments are not a viable approach, since the Ocean Grazer is a device with dimensions of tenths of meters. The Ocean Grazer does not have the resources to do full scale quantitative validation experiments on designs in the development phase. Therefore, small-scale testing and validation is required. Currently, an experimental setup for wave energy extraction is property of the Ocean Grazer research group. The setup is consists of a narrow wave tank, dimensions $(9.07 \times 0.77 \times 1.20)m$, in which a flap wavemaker is driven to create regular waves with a certain frequency and amplitude. The wave tank was designed in order to validate a 1:35 scale prototype of the MP^2PTO-system, in the floater-blanket configuration in the first iteration of the Ocean Grazer design [4; 5]. Thus, the wave tank was designed for 1:35 scale experiments on the previous Ocean Grazer iteration. For the Ocean Grazer 3.0, the wave tank could be utilized for scaled down experiments on the floater arrays. However, insufficient knowledge is available about the properties of the wave tank with respect to wave properties, scaling effects and wave reflection mitigation.

2.2 Problem statement

The Ocean Grazer research group, with prof. dr. A. Vakis and drs. W. Prins as project leaders, is interested in whether the Ocean Grazer experimental wave tank can create adequate experimental environments for future validation and testing experiments.

A scaled-down experimental setup is required in order to validate and optimize the Ocean Grazer WEC systems. The foundation for WEC experiments is the simulation of ocean waves in a wave tank. Currently, a wave tank is present at the Ocean Grazer laboratory. The wave tank was build with the objective to create waves to validate the first iteration of the WEC technology at a 1:35 scale. For future validation experiments and testing, it is essential to possess a thorough understanding of the wave tank. In order to perform accurate experiments on small scale prototypes, it is of great importance that the wave tank is able to produce a well-defined and desired environment that simulates expected ocean behaviour up to certain approximations and limitations. Furthermore, it is important to understand the details of the approximation of the wave tank and whether the assumptions made are adequate for validation purposes. It is especially important to fully understand the experimental wave tank setup, because the Ocean Grazer is continually being developed and adapted and many new design iterations may be subject to experimental validation. This research project aims to study the properties of the Ocean Grazer experimental wave tank in comparison with full scale oceanic environments in order to determine whether the wave tank can be adapted for future experiments. In the worst case, the limitations of the wave tank are detrimental to the accuracy of the experiments and a redesign of the wave tank should be considered. More specifically, this project aims to investigate:

- The wave spectrum and wave properties of the wave tank and its relation to ocean waves
- The properties of scaled-down waves compared to full scale ocean waves
- Wave reflection mitigation methods and their effectiveness in the wave tank

2.3 Methodology

The research will be conducted by performing a computational fluid dynamics (CFD) study on the wave tank. A CFD study was chosen for several reasons. First of all, the infrastructure for doing computationally expensive studies is present at the university. Therefore, it is relatively cost efficient to perform numerical simulations. Furthermore, adaptations to the wave tank are straightforward

in numerical simulation, whereas the physical wave tank has to be physically adapted and materials are required, which is more elaborate and expensive. Finally, during a period of a global pandemic (COVID-19), the ability to work remotely is also convenient.
The wave tank will be simulated using the open-source CFD toolbox OpenFOAM. In the numerical simulation, the wave tank will be recreated on a 1:1 scale. Before an analysis is performed, the wave tank is validated using real data from the experimental wave tank from previous work. After validation, the wave tank will be simulated and adapted to investigate different properties. These include the scaling of the wave height and wavelength, the observed reflection and resulting distortion of the waves and the motion of the particles. The set of proposed experiments are based on and introduced after the validation and intermediate results section. This is done in order to extract relevant data about the wave tank and the produced waves based on what is expected in theory and what is observed in the intermediate results.

3 Theory

3.1 Water waves

In order to correctly compare ocean waves to the waves that are produced in the wave tank, a thorough understanding of waves is required. For water waves, it is required to distinguish between water surface elevations and a wave. Surface elevation is defined as the elevation of the water surface at a single instance in time. Waves are considered when the surface elevation profile is periodic. A single wave is defined by two consecutive downward crossings of the mean surface elevation [6]. This definition is illustrated in Figure 2, where t is time, $\eta(t)$ is the time-dependent surface elevation and the zero line is the mean surface elevation. Note that the surface elevation can be negative, whereas a wave can not.

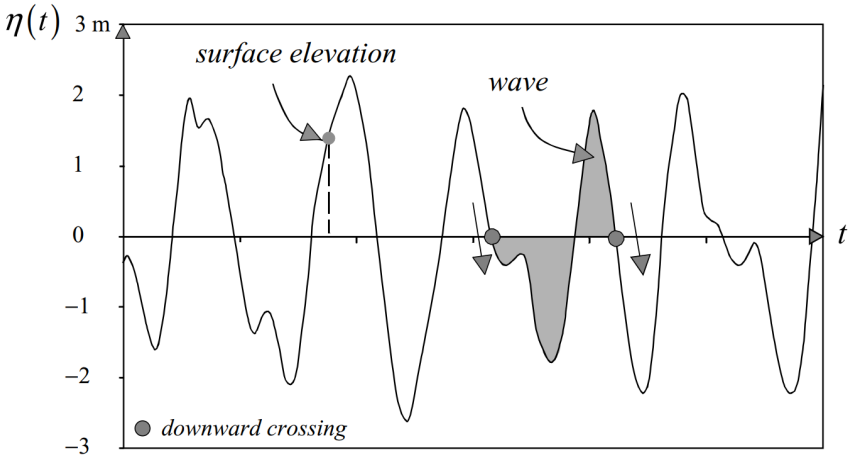

Figure 2: Illustration of the definition of a wave, shown in a record of surface elevation as a function of time [6].

Waves can be described using two characteristics, wave period and height. The wave period is defined as the time between two zero crossings. The wave height is defined as the vertical distance between the lowest surface elevation and highest elevation within the wave period of a given wave. The highest and lowest point are defined as the crest and the trough, respectively. The wave height H and period

T are illustrated in Figure 3.

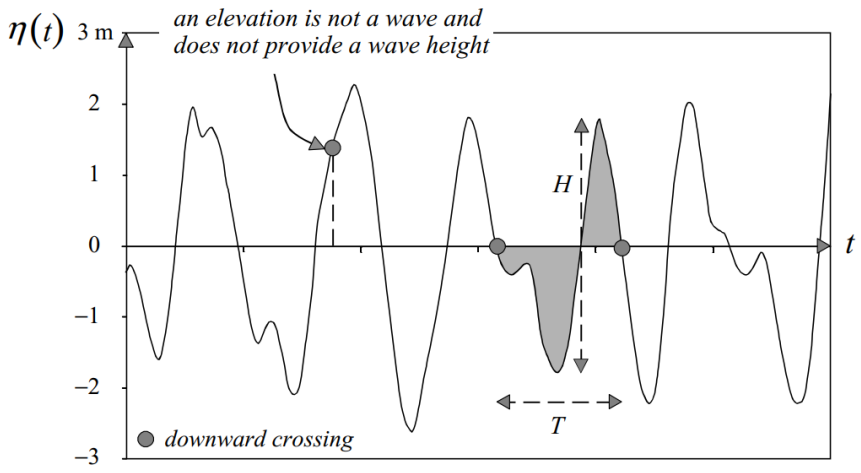

Figure 3: Illustration of the definition of a wave height and period, shown in a record of surface elevation as a function of time [6].

Alternatively, the length of a wave can be expressed in units of length. The wavelength (λ) is defined as the horizontal distance between two consecutive crests or troughs. The amplitude A is the absolute vertical distance between the crest or trough of a wave and the mean surface elevation. The amplitude equals half the wave height.

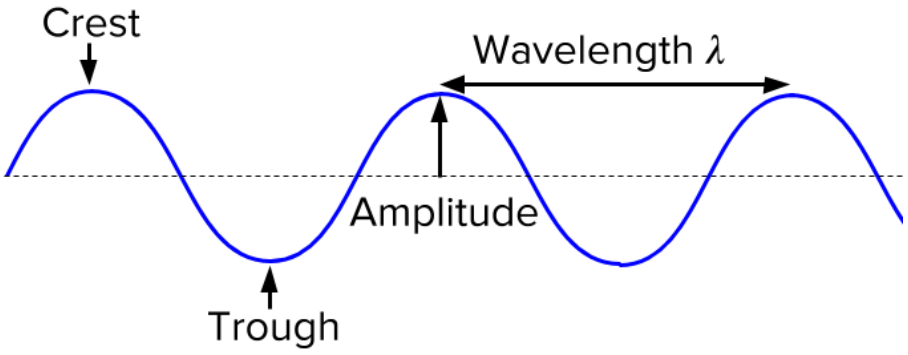

Figure 4: Illustration of the definition of crest, trough, amplitude and wavelength in a 2D spatial coordinate system [7].

3.2 Regularity

It is important to distinguish regular and irregular waves. Regular waves can be described using a simple sinusoidal function. The wave height and period remain constant or can be described with simple equations. These waves typically travel in a single direction. Irregular waves are the result of multiple regular waves originating from multiple sources, travelling in different directions. The sum of many different regular waves may result in irregular waves which have a more complex shape with varying wave heights, multiple hard to define periods and multiple travel directions. An illustration of the resulting shape of multiple regular waves is shown in Figure 5.

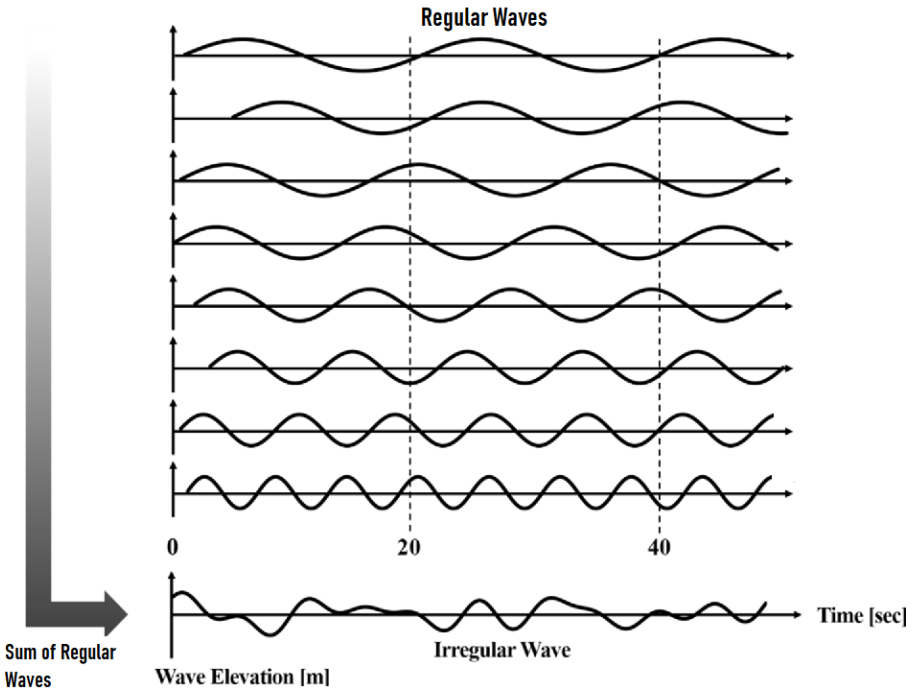

Figure 5: Illustration of the sum of multiple regular waves resulting in irregular wave shapes in a simplified 2D schematic [8].

3.3 Ocean wave spectrum

Ocean waves result from a multitude of phenomena including, but not limited to: fluctuations in the earth's crust and atmosphere, gravitational forces of the sun and moon, earthquakes, atmospheric pressure differences, wind generation and even other waves. All of these phenomena induce waves with periods ranging from days to tenths of seconds. Ocean waves are classified by period length into categories [9]. These are described in the following subsections. The classifications are also provided in Table 1.

Classification	**Period**
Trans-tidal waves	24 hrs and up
Ordinary tides	12 hrs - 24 hrs
Long-period waves	5 min - 12 hrs
Infra-gravity waves	30s to 5 min
Surface gravity waves	0.25s - 30s
Capillary waves	<0.25s

Table 1: Wave classification by period length [9].

Trans-tidal waves

Trans-tidal waves are the longest type of waves. They are generated by the low-frequency fluctuations in the earth's crust and atmosphere. These effects typically occur during a time period of several days or more.

Ordinary tides

Ordinary tides are the result of the gravitational force from both the sun and the earth's moon, as well as the interaction between the oceans. Their period ranges from a few hours up to a day.

Long-period tides

Typical long-period waves have a period of a few minutes up to 12 hours. They are often correlated to the ordinary tides. Within long-period tides we define storm surges, tidal waves and seiches. Storm surges are large scale elevations of the sea surface due to the reduced atmospheric pressure from the storm. The period of the generated wave is therefore equal to the covered surface area of the storm, often ranging from a few hours to 1-2 days. Tidal waves, better known as tsunamis, are the result of a submarine landslide or earthquake. Tsunamis are unpredictable waves and hardly noticeable on the open ocean surface, but dramatically increase their wave height when approaching shallow waters. Seiches are the standing waves that result from the natural frequency of the basin in which they are generated. These basins range from harbours to seas, with periods of a day to a few minutes. They are activated by waves from the open ocean.

Infra-gravity waves

Infra-gravity waves are associated with surf beat at surf zone beaches. They are generated by groups of wind generated waves, and are greatly affected by the macroscopic topography of the ocean floor.

Surface gravity waves

These waves originate from the wind. These are the typical waves the Ocean Grazer aims to harvest energy from. Two types of surface gravity waves are distinguished. Wind sea is the definition for the surface gravity waves while they are being generated. Due to the generation by the wind, they are irregular and have short crests. As they propagate over the sea surface and leave the area of generation, their shape becomes more regular and long-crested. These waves are called swell and are by definition generated by distant weather systems. Wind sea and swell contain the highest amount of harvestable energy and are therefore the main subject of the Ocean Grazer. The periods for surface gravity waves range from $0.25s$ to $30s$, with wind sea and swell having periods of seconds to tenths of seconds, as illustrated in Figure 6.

Capillary waves

Finally, capillary waves are waves that are strongly affected by surface tension. Capillary waves are caused by the wind. Surface-active agents dominate their behaviour. Their periods are smaller than $0.25s$ and very little energy is present in these waves. These waves are responsible for what could be denoted as the water surface roughness, affecting the influence of the wind on the water.

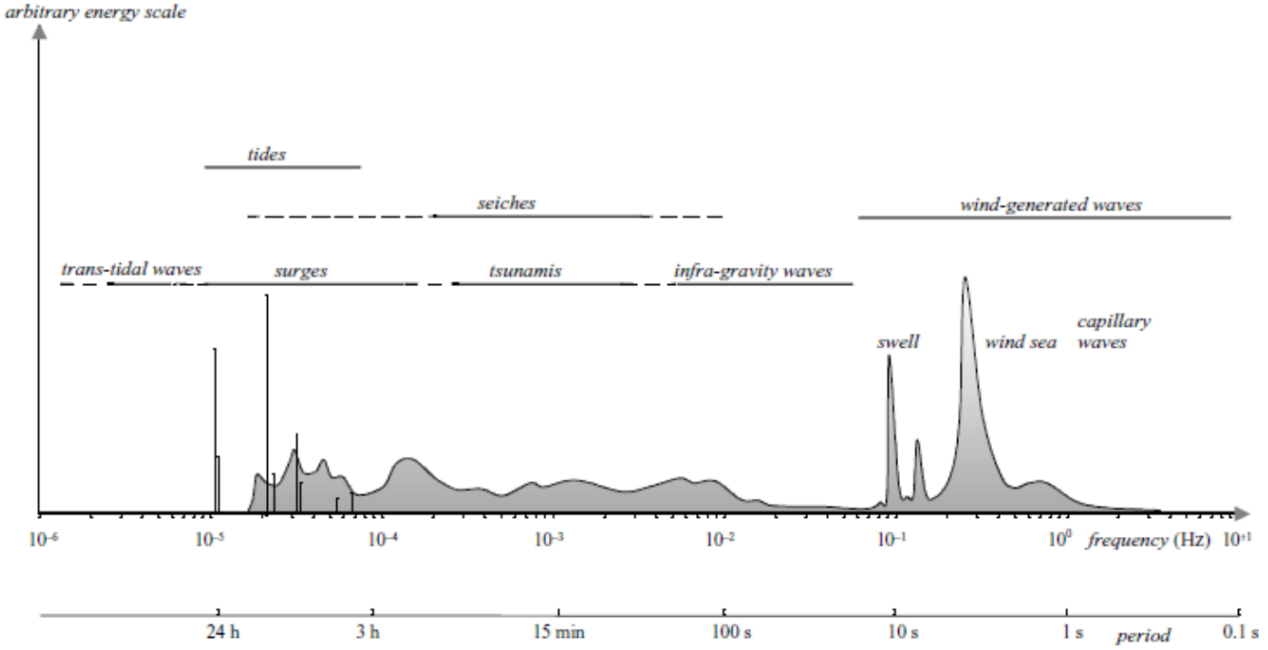

Figure 6: Wave categories by frequency and period, plotted against an arbitrary energy scale [6].

3.4 Linear Wave Theory

3.4.1 Introduction

In this thesis, an attempt is made at the numerical simulation of a real world application. However, for any simulation, validation is required in order to confirm that what was calculated is a representation of the real world and what its limitations and approximations are. Therefore, it is important to possess a theory that describes the phenomena of what is attempted to be modelled. The linear wave theory is a relatively simple approach to describing general ocean wave behaviour. The theory is widely applied to ocean engineering and coastal engineering and gives a relatively good description of the wave kinematics and dynamics in order to anticipate real wave behaviour. In this report, the linear wave theory will act as a way to validate the behaviour that is observed in the numerical wave tank.

3.4.2 Assumptions

Ocean waves are mostly irregular. They are the result of multiple regular waves colliding into a wave spectrum. However, their wave properties are the direct result of the regular waves that formed them. Therefore, an ocean wave theory can be constructed based on the regular harmonic waves that shape the irregular ocean waves. Oceanic waves are described using a relatively straightforward approach to wave theory called linear wave theory. The linear wave theory requires a few assumptions in order to formulate a concise but robust description of ocean waves [6].
First of all, the fluid is assumed to be an ideal fluid. This means that the fluid is incompressible, has zero viscosity and the fluid particles are irrotational. Note that water is generally considered incompressible, however the viscosity of water is non-zero. The linear wave theory still applies to good approximation for water for the purposes of this thesis, since its viscosity is relatively small. Also note that the fluid particles are irrotational, which means that the individual water particles are assumed to not rotate about their center of mass. However, the flow of these particles, defined as the fluid flow

or particle motion, is allowed to follow a rotary trajectory which is a characteristic behaviour observed in fluid particles in waves. This will be discussed more elaborately in Section 3.4.6. Secondly, the fluid is assumed to be homogeneous. Together with the assumption of incompressibility, this implies the fluid density is constant. It must be acknowledged that densities are not constant for different water temperatures. Therefore it is necessary to assume a homogeneous temperature distribution in order to satisfy this assumption.
Furthermore, the wave amplitude is assumed to be relatively small compared to the wavelength, this includes most ocean waves except for extremely large waves and tidal waves. Also, capillary waves are not included because surface tension effects are neglected.
The wave profile is assumed to be two dimensional and invariant in time and space. This implies the waves are described locally and propagate in a single direction without development or energy losses. This also excludes external forces from the Coriolis effect for example.
Pressure at the fluid surface is assumed to be constant and uniform such that there are no additional driving forces for the waves.
Finally, the linear wave theory assumes a horizontal, fixed impermeable bottom or seabed such that the fluid flow is zero at the bottom. This also implies that there are no topological shapes present that could alter the wave properties.

3.4.3 Balance Equations

The basis for the linear wave theory are the balance equations associated with fluid mechanics. In order to formulate the linear theory, mass and momentum need to be conserved. The mass balance equation is given by

$$\frac{\partial \rho}{\partial t} + \frac{\partial \rho u_x}{\partial x} + \frac{\partial \rho u_y}{\partial y} + \frac{\partial \rho u_z}{\partial z} = S_\rho, \tag{1}$$

where ρ is the fluid density, $u_{x,y,z}$ are the velocities in the x,y and z direction, respectively. S_ρ is a source or sink term, representing the generation or dissipation of fluid per unit volume per unit time. The first term describes the local rate of change of the density, which we assumed to be zero. The remaining terms are the advection terms which describe the transport of fluid in all three directions. We assume that there is no production or dissipation of water. Therefore we can reduce the mass balance equation to a continuity equation, given by

$$\frac{\partial u_x}{\partial x} + \frac{\partial u_y}{\partial y} + \frac{\partial u_z}{\partial z} = 0. \tag{2}$$

The momentum balance equation is similar to the mass balance equation. For the x-direction it is given by

$$\frac{\partial(\rho u_x)}{\partial t} + \frac{\partial u_x(\rho u_x)}{\partial x} + \frac{\partial u_y(\rho u_y)}{\partial y} + \frac{\partial u_z(\rho u_z)}{\partial z} = S_x, \tag{3}$$

where S_x is the net production of momentum in the x-direction. A change of momentum is equal to applying a force, since

$$F = ma = \frac{d(mv)}{dt}, \tag{4}$$

with m being mass. Therefore mv equals the momentum of the fluid, with a change in momentum equal to an applied force. Therefore, the momentum balance equation for the x-direction can be rewritten as

$$\frac{\partial(\rho u_x)}{\partial t} = F_x, \tag{5}$$

where F_x equals the applied body force on the fluid per unit volume. In order linearize the theory, the advection terms are omitted as they represent the velocities of the fluid in quadratic combinations, which are non-linear.
The linear wave theory describes the wave behaviour after the wave was produced. Therefore, the only force acting on the waves is due to the pressure gradient as a result of gravity, such that

$$F_x = -\frac{\partial p}{\partial x}. \tag{6}$$

Therefore, substituting Equation 6 into Equation 5, the momentum balance equation in the x-direction can be rewritten as

$$\frac{\partial u_x}{\partial t} = -\frac{1}{\rho}\frac{\partial p}{\partial x}. \tag{7}$$

The same holds for the y and z direction, however gravity should be added to the z-direction, because the weight of a volume of fluid is an additional external force in the z-direction, apart from the gravity induced pressure gradient. Therefore, the linearized momentum balance equations in all three directions are given by

$$F_x = -\frac{\partial p}{\partial x}, \tag{8}$$

$$F_y = -\frac{\partial p}{\partial y}, \tag{9}$$

$$F_z = -\frac{\partial p}{\partial z} - g. \tag{10}$$

3.4.4 Boundary Conditions

Three boundary conditions are defined within linear wave theory. The boundary conditions are the results of the aforementioned assumptions in order to formulate a concise linear theory. First of all, particles at the surface of the fluid are not allowed to leave the surface. This boundary condition can be described using a kinematic condition on the surface layer

$$u_z = \frac{\partial \eta(t)}{\partial t} \qquad \text{at } z = 0, \tag{11}$$

with η being the surface level, u_z the fluid particle velocity in the vertical direction and t time. Note that $z = 0$ defines the origin to be placed at mean surface elevation. Therefore, this condition restricts the vertical movement of the fluid particles to the general vertical velocity due to the waves.
Secondly, it is assumed that the bottom or seabed is horizontal, fixed and impermeable. Therefore, the vertical fluid particle velocity at the bottom should be zero. The bottom is located at $z = -d$, for a water depth of d, with the origin at the water surface. The second kinematic boundary condition is then given by

$$u_z = 0 \qquad \text{at } z = -d. \tag{12}$$

Finally, it assumed that the atmospheric pressure above the fluid should remain constant and no external forces are applied apart from gravity. A constant pressure will ensure that the waves propagate freely and keep an invariant shape. The value of the pressure in this case is irrelevant, since the pressure will remain constant and the fluid is assumed to be incompressible. This implies that the value of the pressure has no effect on the properties of the fluid, such as density and viscosity. Therefore, it is convenient to define the pressure (p) at the surface of the fluid to be

$$p = 0 \qquad \text{at } z = 0. \tag{13}$$

3.4.5 Velocity Potential Function

The analytical solution for the aforementioned balance equations and boundary conditions uses a function called to velocity potential function. The velocity potential (ϕ) function is based on the assumption that the fluid particles are irrotational. The function is defined as a function of which the spatial derivatives are equal to the fluid particle velocities, such that

$$u_x = \frac{\partial \phi}{\partial x}, \tag{14}$$

$$u_y = \frac{\partial \phi}{\partial y}, \tag{15}$$

$$u_z = \frac{\partial \phi}{\partial z}. \tag{16}$$

From this definition, the continuity equation as a result of the mass balance equation (Equation 2) can be rewritten in terms of ϕ, resulting in the Laplace equation

$$\frac{\partial^2 \phi}{\partial x} + \frac{\partial^2 \phi}{\partial y} + \frac{\partial^2 \phi}{\partial z} = \Delta \phi = 0. \tag{17}$$

Introducing the velocity potential function into the three momentum balance equations described in Equations 8, 9 and 10 and rearranging the terms yields the linearised Bernoulli equation for unsteady flow

$$\frac{\partial \phi}{\partial t} + \frac{p}{\rho} + gz = 0. \tag{18}$$

Note that the spatial derivatives disappear, since this equation is equal in every direction, because the gravity component disappears when differentiating with respect to x and y. The aforementioned boundary conditions can then also be rewritten in terms of the velocity potential function, which result in

$$\frac{\partial \phi}{\partial z} = \frac{\partial \eta}{\partial t} \qquad at\ z{=}0, \tag{19}$$

$$\frac{\partial \phi}{\partial z} = 0 \qquad at\ z{=}0, \tag{20}$$

$$\frac{\partial \phi}{\partial t} + g\eta = 0 \qquad at\ z{=}0. \tag{21}$$

Concluding, two equations are provided to describe the fluid behaviour in terms of a velocity potential function. The mass balance equation resulting in the Laplace equation together with the kinematic boundary conditions provide the kinematic behaviour of the fluid particles. The kinematic behaviour of the particles is an important tool in the validation of the numerical simulations as well as wave tank experiments. This behaviour will be further elaborated on in the next section. Additionally, the dynamic aspects of the waves are dealt with using the linearised Bernoulli equation, together with the linearised dynamic boundary condition.

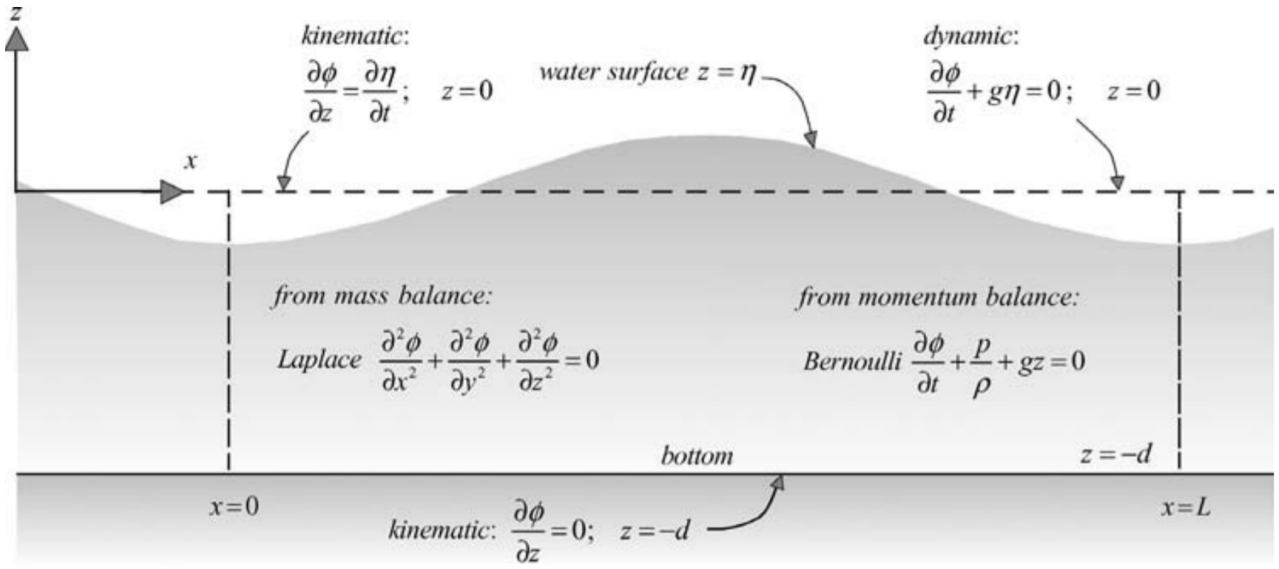

Figure 7: The linearised equations and boundary conditions as a result of linear wave theory [6].

3.4.6 Particle Motion

The fluid particle motion can be described using solely the Laplace equation and the kinematic boundary conditions. One of the solutions to the Laplace equation and kinematic boundary conditions is a long-crested harmonic wave propagating in the positive x-direction. Note that 2D waves are assumed, therefore the waves propagate in a planar manner and we will omit the y-direction. The corresponding surface elevation η is therefore given by a simple sinusoidal function

$$\eta(x,t) = asin(\omega t - kx), \tag{22}$$

where a denotes the wave amplitude, ω the angular frequency and k the wavenumber. The corresponding velocity potential function is given by

$$\phi = \frac{\omega a}{k}\frac{cosh[k(d+z)]}{sinh(kd)}, \tag{23}$$

with d the depth of the water and z the vertical position relative to the mean surface elevation at $z = 0$. The particle motion is described by the local velocities in the water. These values are obtained directly from the velocity potential function. The resulting particle motion is then given by the following two equations

$$u_x = \omega a\frac{cosh[k(d+z)]}{sinh(kd)}sin(\omega t - kx) \tag{24}$$

$$u_z = \omega a\frac{sinh[k(d+z)]}{sinh(kd)}cos(\omega t - kz) \tag{25}$$

Apart from the apparent complexity of the equation, the particle movement is relatively simple. It is important to note that the velocity potential function is dependent on the depth of the water, as well as the vertical position. In the most simple case, $z = 0$ at the mean surface level. If we assume very deep water, such that $kd \to \infty$, then $\frac{cosh(kd)}{sinh(kd)} \approx 1$. In this case, both velocity components become a simple harmonic function with either a sine or cosine. The two equations together describe a perfectly

circular orbit, which is exactly what is observed in water particles of deep water waves. Deep water is defined as water where the depth of the water is larger than half the wavelength of the waves, such that the relative depth $d/\lambda > \frac{1}{2}$. Since the water is relatively deep, the influence of the bottom on the particle motion is negligible. At the surface of the wave, the radii of the orbits are equal to the amplitude of the wave. The particle orbit radii decrease exponentially with depth such that

$$r(z) = A \exp\left(\frac{-2\pi z}{\lambda}\right), \tag{26}$$

where r is the radius of the orbit and z the vertical position of the particle relative to the surface. A and λ are the amplitude and wavelength of the wave, respectively.
Three relative depth categories are distinguished: deep water, intermediate depth water and very shallow water. The shape of the orbital is dependent on the relative depth, d/λ. For intermediate depth to very shallow waters, $d/\lambda < \frac{1}{2}$, the influence of the seabed or bottom on the particle motion becomes relevant. The particle motion becomes an ellipsoid, which becomes flatter for particles towards the bottom. For particles located near the bottom, the particle motion will approach an horizontal motion, conforming to our assumption that the vertical velocity component should be zero at the bottom. The degree of flatness of the ellipsoid is dependent on the shallowness of the water, with shallower waters having flatter elliptic particle motions. The particle motion for different water depths is further illustrated in Figure 8. Since the Ocean Grazer will operate in the deep water condition, it is important to satisfy the deep water condition for waves generated in the wave tank.

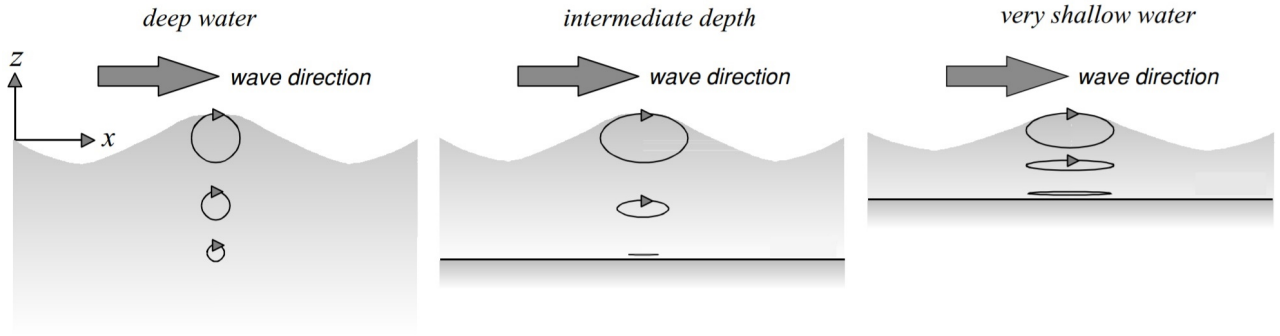

Figure 8: The motion of the water particles in propagating waves for different water depths [6].

3.4.7 Wave propagation

Waves propagate with a certain speed called the phase velocity. The phase velocity is a vector indicating the direction and magnitude of the propagation velocity. For 2D waves, the direction is trivial, therefore it is sufficient to just denote the magnitude, which is called the wave celerity c. From the velocity potential function (Equation 23), together with the harmonic surface profile (Equation 22) and the dynamic surface boundary condition (Equation 21) a dispersion relation is defined,

$$\omega^2 = gk\ tanh(kd), \tag{27}$$

which relates the wave number k to the angular frequency ω. This is an implicit expression in terms of the wave number, with no trivial solutions. In order to solve this, an iterative procedure is required to calculate the wave number for a given frequency and depth. An alternative is to use the approximation

$$kd \approx \frac{\alpha + \beta^2 (cosh(\beta))^{-2}}{tanh(\beta) + \beta (cosh(\beta))^{-2}}, \tag{28}$$

with $\alpha = \frac{\omega^2 d}{g}$ and $\beta = \alpha(tanh(\alpha))^{-\frac{1}{2}}$, which yields the exact solutions for the deep and very shallow water cases, and has a relative error of less than 0.0005 for cases in-between. The celerity ($c = \omega/k$) can then be directly obtained from the dispersion relation, resulting in

$$c = \frac{g}{\omega} tanh(kd) = \sqrt{\frac{g}{k} tanh(kd)}. \tag{29}$$

This equation shows that the phase velocity or celerity of the waves is dependent on the frequency and therefore also on the wave number. Waves with a high frequency travel slower than waves with a low frequency, and thus long waves travel faster than short waves. For deep water, $kd \to \infty$, $\tanh(kd) \to 1$ and the celerity reduces to

$$c = \sqrt{\frac{g}{k}} = \frac{g}{\omega} = \frac{g}{2\pi} T = 1.56T \ [\frac{m}{s^2}, s]. \tag{30}$$

In very shallow water, for very small kd, $tanh(kd) \to kd$, the celerity reduces to

$$c = \sqrt{gd}. \tag{31}$$

Therefore, in very shallow waters, the celerity is not dependent on the wavelength or frequency.

3.5 Wavemaker Theory

In order for wave propagation to occur, it is required to have a wave source. Typically, for the physical generation of waves for experimental purposes, two wavemaker types are distinguished: a piston wavemaker and a flap wavemaker. Both wavemakers are located at the beginning of the wave tank, where they produce waves by displacing the fluid periodically to create regular waves as described in the aforementioned linear wave theory. The piston wavemaker is and remains perpendicular to the wave tank bottom. It creates waves by moving periodically back and forth in the propagation direction. The wavemaker displaces the fluid independent of the depth, therefore all of the fluid will be part of the wave. This is characteristic of very shallow water, where the waves feel the bottom of the tank. The piston wavemaker and the resulting wave and particle motion is shown are Figure 9.
The flap wavemaker, also denoted as hinge wavemaker, is fixed to the bottom of the tank with a hinge type joint. The waves are created by periodically tilting the flap in the positive and negative x-direction. Since the amount of displaced fluid is larger towards the surface of the water, most of the wave energy is confined to the fluid located towards the surface. In this case, the wave remains unaffected by the bottom of the tank as long as the wavelength remains smaller than twice the depth. This is the definition of deep water waves, which is represented by the resulting particle motion, as illustrated in Figure 10.

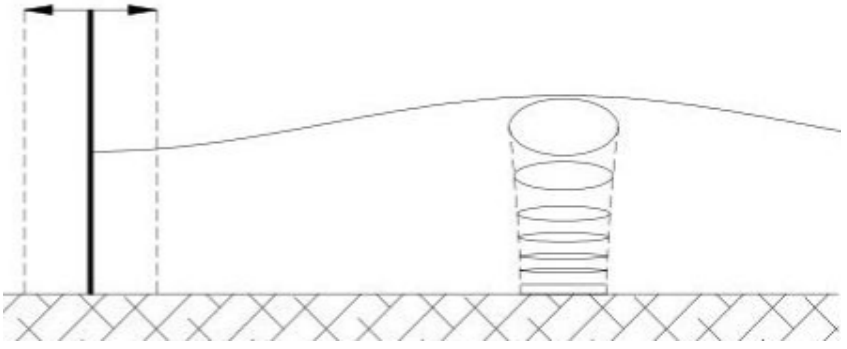

Figure 9: An illustration of a piston wavemaker and the resulting wave and particle motion [10].

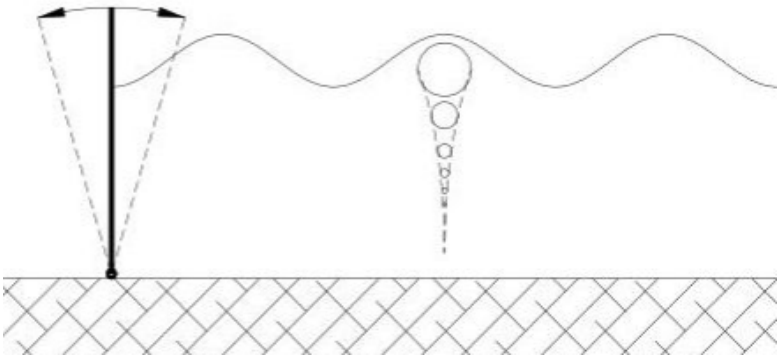

Figure 10: An illustration of a flap wavemaker and the resulting wave and particle motion [10].

The wave height and period produced by either type of wavemaker is dependent on wavemaker motion. A shape function $U(z)$ is defined in order to describe the movement of the wavemaker [11]

$$U(z) = \frac{1}{2}S\omega \qquad \text{for piston wavemakers,} \tag{32}$$

$$U(z) = \frac{1}{2}S\omega(1 + \frac{z}{d}) \qquad \text{for flap wavemakers,} \tag{33}$$

where ω is the angular frequency of the wavemaker. The angular frequency of the wavemaker and the resulting wave will be equal for both wave makers. S is the stroke of the wave maker, defined as the distance between the flap wavemaker maxima in the x-direction at the water surface level. d is the water depth, illustrated in Figure 11.

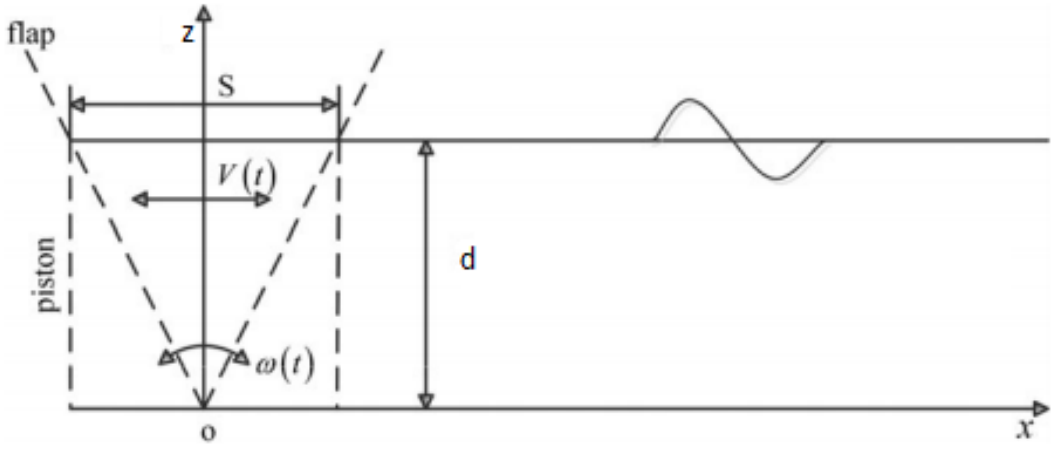

Figure 11: An illustration of a stroke S for both wavemakers [11].

The resulting wave height can be found by the use of the hydrodynamic transfer function Tr, which

directly relates the wave height to the wavemaker stroke [12].

$$Tr = \frac{H}{S} = \frac{2(cosh(2kd) - 1)}{sinh(2kd) + 2kd} \quad \text{for piston wave makers,} \tag{34}$$

$$Tr = \frac{H}{S} = \frac{4sinh(kd)}{kd} \frac{kdsinh(kd) - cosh(kd) + 1}{sinh(2kd) + 2kd} \quad \text{for flap wavemakers,} \tag{35}$$

where d is the water depth and k is the wavenumber as obtained from the dispersion relation in Equation 27.

3.6 Physical modeling

This thesis aims to understand the properties and limitations of the OG experimental wave tank. Therefore it is important to posses a good understanding of the physical modelling of waves. Wave flumes, which is the definition of wave tanks that have a width much smaller than their length, attempt to model 2D waves propagating in a single direction. Wave tanks or flumes typically contain three sections, a wave generation zone, a free surface zone and an absorption zone. In the first zone, the waves are generated and developing. In the free surface zone, the wave are fully developed "free waves" and propagate through the tank undisturbed. This is typically where experiments are performed with WECs for example. In the final zone, an attempt is done to absorb the wave, preventing reflection off the wall, such that the free waves are not disturbed by the reflected waves. An illustration of the three zones is shown in Figure 12.

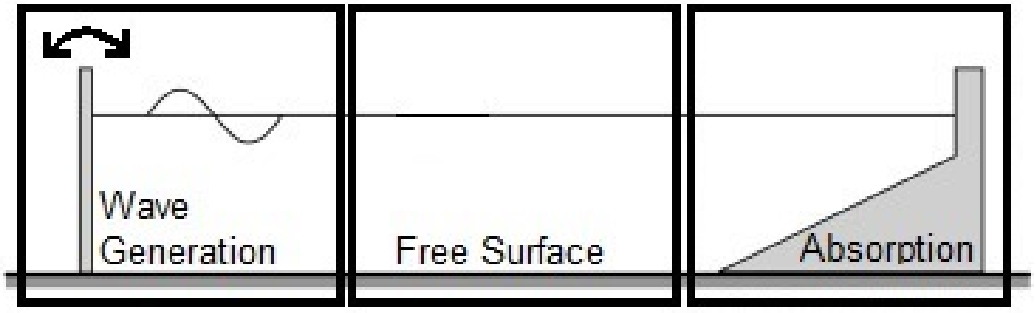

Figure 12: Schematic of a generic wavetank including the wave generation, free surface and absorption zones [13].

Typically, these models are created at a scale ranging from 1:30 to 1:100, depending on the wave tank, wave parameters and available resources[14]. However, dimensional scaling is not equal for all parameters within the model. It is important to retain the relative magnitude of the dynamics and kinematics that drive the to-be-observed phenomena. In order to scale properly, Froude's scaling law is applied:

$$Fr = \frac{u_0}{\sqrt{gl_0}} = \frac{u_{scaled}}{\sqrt{gl_{scaled}}}, \tag{36}$$

where u equals the velocity, g the gravitational constant and l any characteristic length scale. 0 and *scaled* denote either the original case or the scaled case, respectively. Keeping Froude's number constant during scaling ensures that the driving dynamics and kinematics retain their relative influence. From Froude's law, we can derive a simple scaling condition

$$\left(\frac{u}{\sqrt{l}}\right)_0 = \left(\frac{u}{\sqrt{l}}\right)_{scaled}, \tag{37}$$

from which we can find the scaling factors for all relevant parameters, which are shown in Table 2. Even though the driving parameters are scaled properly, other parameters are still present. One notable parameter is surface tension, which is a negligible force for the original case, however it becomes more prevalent as the scaling factor increases. As mentioned before, waves that are dominated by surface tension (capillary waves) have a wave period of less than a quarter of second. In order to ensure surface tension does not influence the model in a significant way, it is important to have a sufficiently large model. Also, viscosity does not scale appropriately to small scales and its effect is often overestimated at these scales [15]. As a result, a discrepancy is often observed when comparing the empirical results to analytical results or numerical results. It is possible to tune numerical simulations using empirical data, however this is not a reliable approach. In general, a scaled physical model should be as large as possible for the most representative results. Furthermore, the parameters of the wave tank are also of importance in the accuracy of the physical model. A few general rules in order to generate fully developed deep water waves are:

- The wave tank length should be at least twice the hinge depth of the flap wavemaker.
- The length of the beach should be at least half a wavelength for optimal (up to 90%) wave absorption.
- The depth of the wave tank needs to be half the wavelength.

Parameter	Scale
Wave Height	N^1
Wave Period	$N^{0.5}$
Wave Frequency	$N^{0.5}$
Mass	N^3
Force	N^3

Table 2: Scaling factors for relevant parameters according to Froude's scaling law. N denotes the scaling factor.

3.7 Experimental Wave Tank

The Ocean Grazer experimental wave tank was built by hand by OG employees, in the first place to show a proof of concept of the WEC and power take-off (PTO) system. Later it was also used to perform some testing on a 1:35 scale model of a floater blanket design. The dimensions of the wave tank are $(9.57\times0.77\times1.20)m$ and are also shown in the schematic of the wave tank in Figure 13. The waves are generated by the flap wavemaker, located at $0.5m$ from the start of the wave tank. The waves can then freely propagate for $6.35m$ until they reach the beach. A short ramp of $0.42m$ leads to the beach which completes the tank. The water level is typically at $0.9m$.

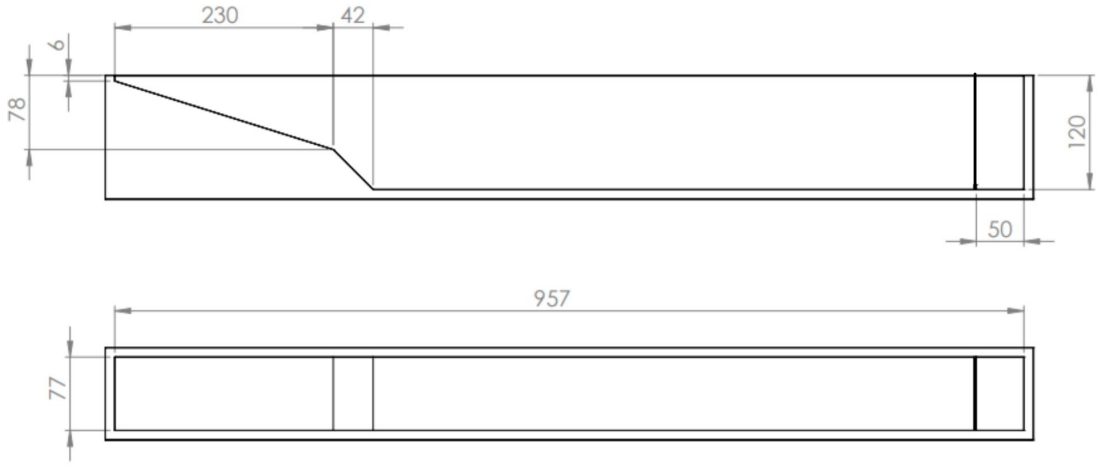

Figure 13: Schematic of the OG experimental wave tank from a side and top view, respectively [5].

In one of the side walls of the wave tank, two acrylic glass planes act as windows to monitor what happens inside the wave tank. These planes are $(1.70 \times 0.75)m$. The top of the plane is about $0.25m$ from the top the of the wall. Therefore, that non-visible part should not be included in the wave height, since it is unable to be monitored. These planes are shown in Figure 14.

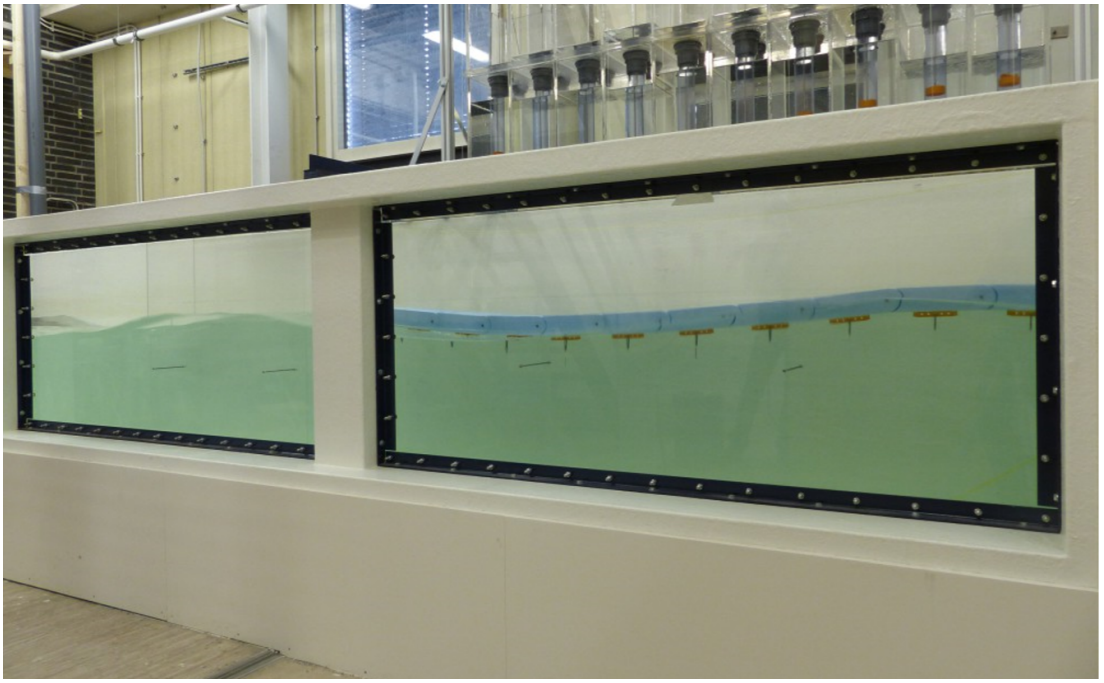

Figure 14: The acrylic glass planes in the wall of the wave tank.

The flap wavemaker is driven by a motor. The motor rotates an adjustable arm, to which the wavemaker is connected using a rod. The rotating arm can be extended up to $0.25m$. The motor frequency can also be adjusted to a maximum of 60Hz [16]. The wavemaker angle is restricted to about 22 degrees, before it will collide with the back of the wave tank. This is not a restriction to the waves

that can be produced, since realistically scaled waves will require only a few degrees of wavemaker movement, as will be described later.
At the beach, a foam layer can be installed for additional absorption. The foam layer is a porous filter material typically used to filter small ponds. The foam layer is installed at $0.31m$ from the beginning of the beach, as can be seen from Figure 15. The layer extends till the end of the tank, and is partially submerged. The beach length is defined as the part of the beach that is submerged in the rest position, and is equal to $1.31m$.

Figure 15: The foam layer installed at the beach in the wave tank.

The foam layer's base height is $0.04m$. On top of the base a profile of rectangular wedges is present, with a height and length of $0.03m$, at $0.03m$ from each other, as illustrated in Figure 16. Properties such as density, porosity and mean hole diameter are unknown.

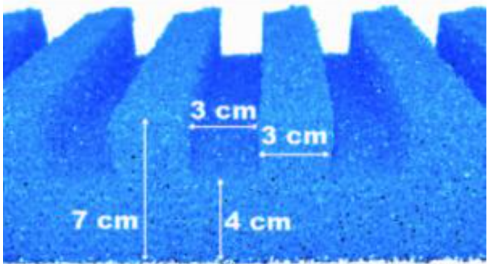

Figure 16: The foam layer dimensions.

4 Numerical Model

4.1 olaFlow

The numerical model is developed in OpenFOAM®. OpenFOAM is an open-source toolbox for computational fluid dynamics (CFD). Typically, this software is used for aerodynamic and hydrodynamic

problems focusing on flows around objects. For wave dynamics a specialized CFD suite was used, called olaFlow [18]. olaFlow is specifically designed to model two incompressible, isothermal immiscible fluids for wave generation, wave interactions, wave-structure interactions and also wave absorption including porous materials.

4.2 Courant Number

olaFlow computes the three dimensional Volume-Averaged, Reynolds-Averaged Navier-Stokes (VARANS) equations using finite volume discretization. Discretization is performed on both time and space. The time is divided into discrete time steps Δt. The space is also discretized into cells of a finite volume with characteristic length Δh. For every time step, the local solution is computed in every cell, based on either the initial conditions or the result of the previous time step. The time step size is variable and dependent on the rate of information that "flows" through the domain. The Courant number defines how much information is allowed to pass through one cell in a given time step. It is defined as [19]:

$$C = \frac{v\Delta t}{\Delta h}, \tag{38}$$

where v is the flow velocity of information, Δt is the variable discrete time step, and Δh denotes the characteristic length of a mesh cell in one dimension. Therefore for C<1, information can not cross more than one cell in one time step. This is illustrated in Figure 17. In order to ensure no interactions are missed, the Courant number for this model is set at 0.3.

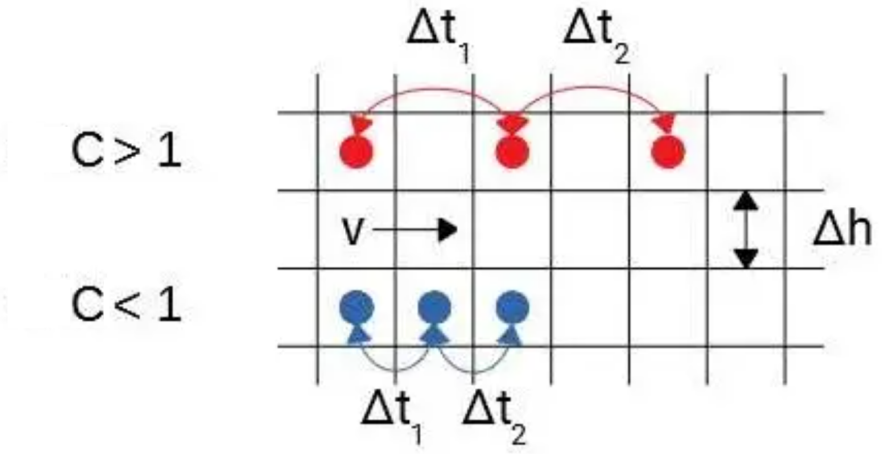

Figure 17: Illustration of the Courant number and its implication on the size of the time step Δt in a discretized domain with characteristic cell length Δh [20].

4.3 Volume of Fluid

Two immiscible fluids form a free surface by definition. The free surface is a discontinuous layer between the two fluids, water and air for the models described in this thesis. In olaFlow, the free surface is modelled using a Volume Of Fluid (VOF) technique. VOF defines an indicator function α to indicate the fraction of the cell that is occupied by the fluid of interest. For α=1 would indicate the cell is completely filled with the volume of interest, water in this case. α=0.5 would indicate the cell is half water, half air. In this way, the free surface can be described using a continuous transition layer

where α decreases from 1 to 0. This relatively simple approach enables relatively complex free surface configurations without requiring complex movement of the mesh. The movement of the fluid fractions is then defined as the local change of α, as a result of the fluid velocity. The resulting advection equation is given by:

$$\frac{\partial \alpha}{\partial t} + \nabla \cdot (\alpha \boldsymbol{u}) = 0 \tag{39}$$

4.4 VARANS Equations

Similar to linear wave theory, the VARANS equations are based on the two balance equations for mass and momentum. The continuity equation as a result of the mass balance equation is given by

$$\frac{\partial u_i}{\partial x_i} = 0, \tag{40}$$

which is the Einstein notation equivalent of Equation (2) in Cartesian coordinates. u_i indicates the flow in the x_i direction, with $x_{1,2,3}$ corresponding to x, y, z. The momentum mass balance equation (Equation (3)), in all three directions leads directly to the general Reynolds-averaged Navier-Stokes equations (RANS) [17]. The general RANS equations are given by

$$\frac{\partial \rho u_i}{\partial t} + u_j \frac{\partial \rho u_i}{\partial x_j} = -\frac{\partial p}{\partial x_i} + \rho g_i + + \frac{\partial}{\partial x_j}\left[\mu \frac{\partial u_i}{\partial x_j}\right] - \frac{\partial}{\partial x_j}[\rho \overline{u_i' u_j'}], \tag{41}$$

with ρ the density, μ the viscosity and g the gravity which is only non-zero in the third direction. u' indicates the turbulent or fluctuating part of u. The terms in the above equations represent the local acceleration, convective acceleration, pressure gradient, body forces due to gravity, and the viscous and Reynolds stresses, respectively. The product of the last term will results in the Reynolds stress tensor, which includes turbulence and is often modelled as additional viscosity, denoted by μ_t. That would result in the following equations [21]:

$$\frac{\partial \rho u_i}{\partial t} + u_j \frac{\partial \rho u_i}{\partial x_j} = -\frac{\partial p}{\partial x_i} + \rho g_i + \frac{\partial}{\partial x_j}\left[(\mu + \mu_t)\frac{\partial u_i}{\partial u_j}\right]. \tag{42}$$

The continuity equation and general RANS equations are then volume-averaged (VA), to end up with the VARANS equations. Volume-averaging is performed in order to deal with flow inside porous media in a discretized calculation. This way, the micro behaviour of the fluid through porous media in a certain control region is averaged over its volume to a value at a single specific point. This is illustrated in Figure 18.

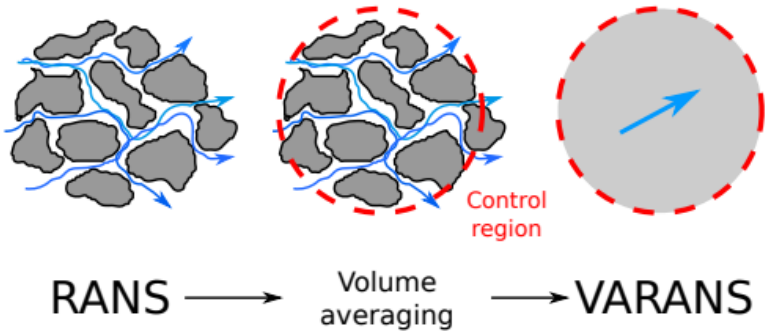

Figure 18: Illustration of volume averaging in porous media[22].

Volume averaging of a certain parameter a is defined as applying a mathematical operator denoted by $\langle\rangle$ such that

$$\langle a \rangle = \frac{1}{V} \int_{V_f} a dV. \tag{43}$$

The resulting volume-averaged continuity equation is then simply given by

$$\frac{\partial \langle u_i \rangle}{\partial x_i} = 0. \tag{44}$$

The derivation of the volume-averaged RANS equations is more elaborate and complex. The derivation is beyond the scope of this thesis, however an important thing to note is that certain terms can not be solved analytically. These parts are dealt with using closure laws. The volume-averaged RANS equations result in [22]

$$\frac{\partial \rho \langle u_i \rangle}{\partial t} + \frac{\partial}{\partial x_j}\left[\frac{1}{\phi}\rho \langle u_i \rangle \langle u_j \rangle\right] = -\phi \frac{\partial \langle p \rangle^f}{\partial x_i} + \phi \rho g_i + \frac{\partial}{\partial x_j}\left[\mu \frac{\partial \langle u_i \rangle}{\partial x_j}\right] - \frac{\partial}{\partial x_j}[\rho \langle \overline{u_i' u_j'} \rangle] + [CT]_{ST} + [CT]_{DY}, \tag{45}$$

where $\langle p^f \rangle$ is the intrinsic pressure and ϕ the porosity. The appearance of porosity is the direct result of volume-averaging the density inside porous media. CT indicates a closure term, which are the unsolvable parts of the VARANS equations that capture physics such as frictional forces, pressure forces and added mass of the porous media. This is the result of volume averaging with static porosity (ST) and dynamic porosity (DY). Static porosity appears in porous media from coastal structures that remain fixed. The dynamic porosity corresponds to porous media such as sand, which have a changing porosity due to particles that can move. In cases where the flow is completely laminar, these additional terms equate to zero and can be omitted. However, in this model turbulent effects are expected since the model should predict waves being absorbed at a beach, predominantly by crashing.

4.5 Turbulence model

Closure models for turbulent effects in the RANS equations are commonly referred to as turbulence models. These models attempt to approximate the turbulent effects in a numerical model by two partial differential equations tuned to empirical values. Different models approach turbulence differently and perform differently depending on the region of interest. Two models are generally discussed within the context of the RANS equations; $k-\epsilon$ and $k-\omega$. Both models attempt to approximate the solution of the RANS equations in turbulent flow. The $k-\epsilon$ model does this by approximating the turbulent flow characteristics based on calculating two transport parameters: the turbulent kinetic energy k and the dissipation of kinetic energy ϵ. The model assumes a solution close to the walls based on the flow characteristics using wall functions, to determine the solution away from the wall. This is generally an accurate method for calculating turbulent flow characteristics, but is relatively inaccurate close to the walls. The $k-\omega$ model works similarly, with k being the turbulent kinetic energy and ω the rate of energy dissipation, similar to ϵ. The difference is that the $k-\omega$ model is actively calculating the wall effects rather than approximating it based on the flow characteristics. This model is generally more accurate around the walls, however it is also computationally more expensive. olaFlow supports both models. The closure model elected for this model is the $k-\omega$ SST model, which is a combination of both. This is model was developed by Menter [23], and attempts to take advantage of the best of both models. Close to the walls it will apply the $k-\omega$ model, which is important during absorption at the beach. For calculations relatively far away from the walls, the model will be identical to the $k-\epsilon$ model. This way, the computational cost is limited while still retaining good turbulence prediction

at the walls, which is especially important at the beach where the waves should be absorbed. The (non-volume averaged) partial differential equations for k and ω are given by:

$$\frac{\partial k}{\partial t} + \mathbf{u} \cdot \nabla k - \nabla \cdot (D_k \nabla k) + \beta_k k = F_k, \tag{46}$$

$$\frac{\partial \omega}{\partial t} + \mathbf{u} \cdot \nabla \omega - \nabla \cdot (D_\omega \nabla \omega) - (1 - F_1) C D_{k\omega} + \beta_\omega \omega = F_\omega, \tag{47}$$

where k and ω are the turbulent kinetic energy and frequency scale, respectively. D_k and D_ω are the diffusion coefficients, β_k, β_ω are the dissipation terms and F_k and F_ω are the production terms. This thesis will not go through the intermediate expression for the aforementioned coefficients or the implementation of volume-averaging on the turbulence model. This is done in detail by Higuera [22]. The limitation of this model is that it has not been developed for dynamic porosity cases. Therefore, for the $k - \omega$ SST model, it is assumed that the porosity is constant. This is a valid assumption, because within the wave tank there should be no particle-like sediment, only an absorbing sloping beach which may or may not have a fixed porous absorption layer with a constant porosity.

4.6 Porosity

The flow through porous media is computed by considering a set of drag forces generated by the material. The flow through a porous medium is defined using a hydraulic gradient I, which is proportional to the pressure drop. The (volume-averaged) hydraulic gradient is given by

$$I = A\langle u_i \rangle + B\,|\langle u \rangle|\,\langle u_i \rangle + C\frac{\partial \langle u_i \rangle}{\partial t}, \tag{48}$$

where u is the flow velocity. A is the friction coefficient related to the pressure loss in different materials with laminar flow (low Reynolds number). B is associated with transitional and turbulent flows (high Reynolds number). C is the parameter for the third term, which considers the formulation for unsteady flow to a certain extent. The friction coefficients require calibration for different cases. Their values are calculated using the following formulas which were developed by Engelund [24]:

$$A = \alpha \frac{(1-\phi)^3}{\phi^2} \frac{\nu}{D_{50}^2}, \tag{49}$$

$$B = \beta \frac{1-\phi}{\phi^3} \frac{1}{D_{50}}, \tag{50}$$

where ϕ is the porosity of the material, ν is the kinematic viscosity in m^2/s and D_{50} is the mean nominal diameter of the porous material in m. α and β characterize the friction terms and require calibration with experimental results. Finally, friction coefficient C has been proven to be less significant to variations than A or B for most applications and is assigned a default value of $C = 0.34$ [25].

5 Model Description

5.1 Domain

5.1.1 Dimensions

The domain of the wave tank is replicated in the olaFlow suite. The wave tank dimensions are reduced to $(9.07 \times 0.77 \times 1.20)m$. The length of the tank is reduced with $0.5m$, omitting the space behind the flap wavemaker, see Figure 13. This is done because the space behind the wave maker should have

no impact on the created waves. Omitting this space will save computational cost by reducing the domain and simplify the model by integrating the wave maker as a moving boundary. The boundary will be a moving wall which will rotate around an axis fixed at the bottom, replicating the flap wave maker. This boundary condition will be further elaborated on in Section 5.2. The remaining part of the wave tank is created identical to the OG experimental wave tank described in Section 3.7. The resulting domain is visualized in Paraview and shown in Figure 19.

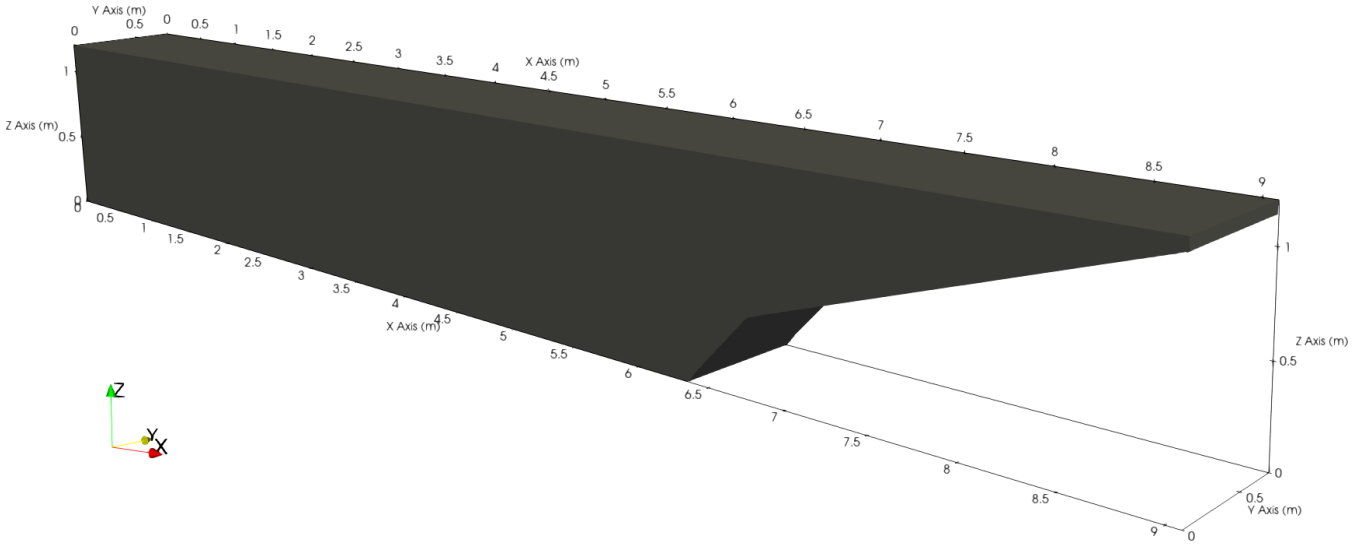

Figure 19: Illustration of the numerical domain of the wave tank.

5.2 Boundary Conditions

5.2.1 Boundary labels

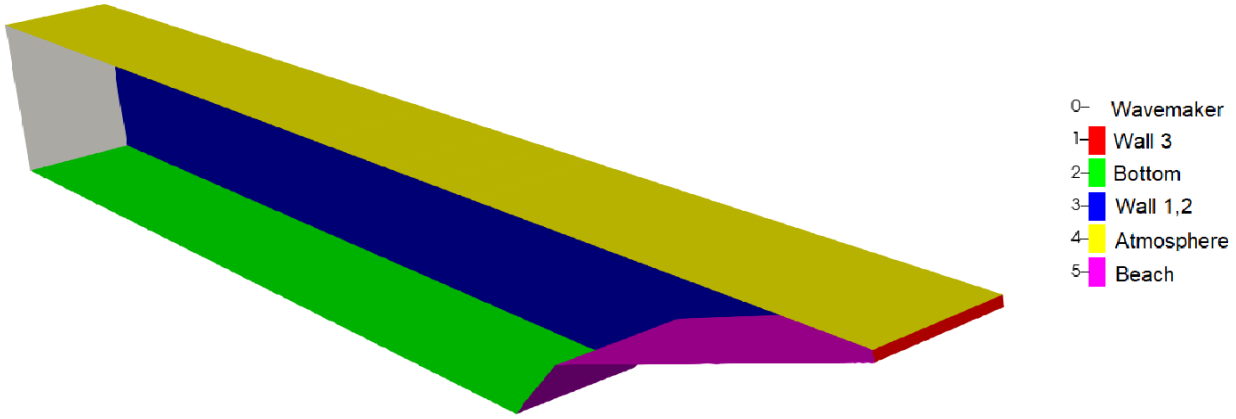

Figure 20: Illustration of the labelling of the boundaries.

The domain boundaries are given labels such that defining boundary conditions is straight-forward. We define 5 different boundaries as illustrated in Figure 20 and shown in Table 3, along with their function. Note that Wall 2 is not visible in the Figure, but it is symmetric with Wall 1 (blue). The

wavemaker is defined as the moving wall that generates the waves. The complete structure starting from the initial slope until the end of the wave tank is denoted as the beach. The bottom is the floor before the beach, starting at the wavemaker. The top, or lid of the domain is defined as the atmosphere, as it is required to have an "open" domain for pressure dissipation. The function of the boundaries is further elaborated in the next subsections.

Label	Function
Wavemaker	Moving wall to generate waves
Walls 1,2,3	Contain the water
Beach	Absorb the incident waves
Bottom	Contain the water
Atmosphere	Dissipate pressures

Table 3: Labels of the different domain boundaries in the model.

5.2.2 Fluid volume

For the fluids, it is important that they are contained within the walls. Therefore, a *zero-gradient* boundary condition is applied on all walls, the bottom, wavemaker and the beach. This contains the volume of the fluid at the mentioned boundaries and ensures the total volume of water remains constant. The condition on the atmosphere is an *inlet-outlet* condition. Since both fluids (water and air) are defined as incompressible fluids, a closed domain would restrict the airflow. The incompressibility of the air together with a forced airflow as a result of a closed domain could influence the water surface. Furthermore, the experimental wave tank also has an open top. Note that the water will also leave the domain if the surface elevates above the domain boundary.

5.2.3 Pressure

In olaFlow, the dynamic pressure $p_{\rho gh}$ is calculated, which is defined as

$$p_{\rho gh} = p - \rho g h, \tag{51}$$

with ρ the density of the fluid, g the gravitational constant and h the position in the z-direction. Their product equates to the hydrostatic pressure. Therefore, olaFlow calculates the pressure without the hydrostatic pressure. The dynamic pressure boundary conditions are *fixed-flux* pressure conditions with a fixed value of zero on all boundaries, except for the atmosphere. The *fixed-flux* condition restricts the exchange of pressure in and out of the domain to a fixed value, in this case zero, so no exchange is possible. The atmosphere has a *total-pressure* condition, which adapts the flux of pressure over the boundary in order to keep the total pressure over the boundary constant. In this case, the total pressure is set to zero for simplicity. Since both fluids are assumed incompressible, this implies that the pressure on the surface of the water will always be zero. This assumption is justified in Section 3.4.4.

5.2.4 Velocity

In CFD it is common to distinguish two wall conditions: slip and no-slip. This boundary condition determines the velocities of the fluid near the boundaries. In reality, the walls in the wave tank have a certain surface roughness. Due to the surface roughness, water particles adhere to the wall, creating a layer of water particles with velocity $v = 0$. The fluid particles farther from the wall are

attracted to the stationary particles due to cohesive forces. This slows down the particles that pass the stationary particles and creates shear stresses in the fluid. The result is a velocity gradient where the velocity of the fluid particles is greater further away from the wall, which is illustrated in Figure 21. This gradient is called a boundary layer, and is modelled using the no-slip condition. In olaFlow, the no-slip condition is defined as a fixed fluid velocity of zero at the wall, denoted as the *fixed-value* condition. The *fixed-value* boundary condition (no-slip) is applied to the walls, beach and bottom. For the wavemaker, a similar boundary condition is applied: the *moving-wall* velocity condition. This condition corrects the flux through the boundary to be zero. The correction is necessary because of the movement of the boundary. Finally, a *pressure-inlet/outlet* velocity condition is defined on the atmosphere. Similar as for pressure and fluid volume, this condition allows the atmosphere boundary to behave like an open top. The *pressure-inlet/outlet* velocity condition works in tandem with the zero *total-pressure* condition and allows for velocities in and out of the boundary. These are known as self-stabilizing boundary conditions.

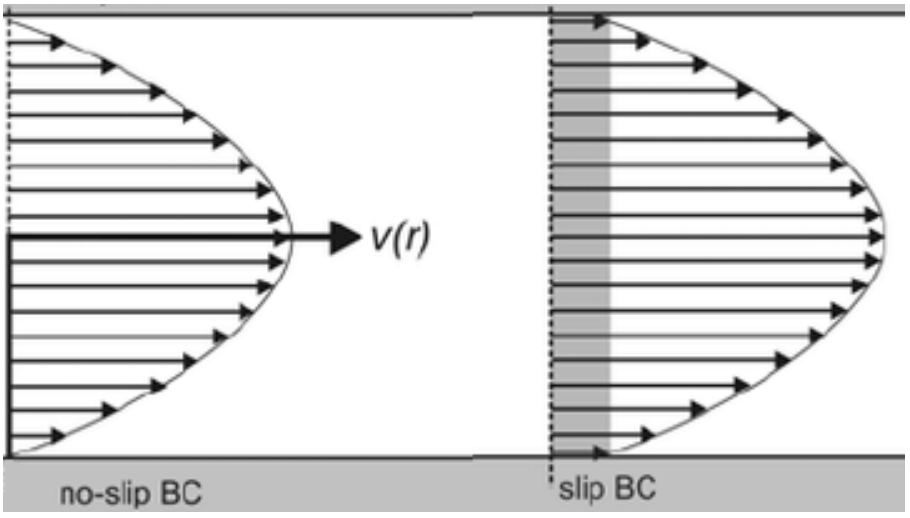

Figure 21: Illustration of the difference between velocity wall conditions [26].

5.2.5 Turbulence

As mentioned before, the turbulence is modelled using a $k-\omega$ SST model. The two variables k and ω are calculated at every time step. For boundary conditions, both variables have a default wall function available for the no-slip boundary condition similar to the velocity boundary condition denoted *kqRWallFunction* and *omegaWallFunction* for k and ω, respectively. These wall functions are the no-slip boundary condition for turbulence modelling within the $k-\omega$ SST model, where close to the wall the turbulence is modelled using a $k-\omega$ model. The no-slip wall functions are applied to the walls, bottom, wavemaker and beach. Similar to previous variables, the atmosphere boundary is assigned an *inlet/outlet* condition in order to dissipate turbulence and create an open boundary.

5.3 Displacement

The final boundary condition defines the ability of the domain to be displaced relative to its initial position. This is the condition that enables the wavemaker to move. For the wavemaker, a *wavemaker-movement* condition is applied. This is a condition that reads a file with predetermined movement positions for every time step, prescribing the angle of the wavemaker boundary over time and thus

defining its movement. The atmosphere and Wall 3 are defined to be fixed by a zero-gradient condition. The wavemaker movement causes stretching and compression of the mesh. In order to ensure the model can converge, parts of the domain are required to be allowed to move. This allows the domain and the mesh to be stretched and compressed without divergence of the simulation due to inverted meshes, boundary collisions or similar errors. Therefore, on the other walls, beach and bottom a *fixed-normal-slip* is applied, which fixes the surface normal of the boundary, such that it is unable to rotate. Small translational movements within the other constraints are still allowed.

5.4 Initial conditions

The setup of the model requires some initial state that defines from which state the numerical model will start. For this model, the computation will always start from time $t = 0s$. The first initialization step is the setting of the fluid properties. First, the amount of phases are determined to be two, denoted water and air. Water and air are computed during the simulation using the volume of fluid method described in Section 4.3, with a parameter α, where $\alpha = 1$ equals water and $\alpha = 0$ equals air. The model uses a Newtonian model for the transport in and between fluids and assumes a constant viscosity and density at 20°C. The properties of the fluids are given in Table 4. The surface tension between the two fluids is $0.07N/m$.

Fluid	α	Kinematic viscosity (m^2/s)	Density (kg/m^3)
Water	1	1×10^{-6}	1000
Air	0	1.48×10^{-5}	1

Table 4: Properties of the two fluids.

In olaFlow, first the default fluid value is defined. Initially, the default fluid will fill the entire domain. In this model, the default fluid is $\alpha = 0$, which is air. Then the volume of the other fluid is defined. The water volume is defined as a cuboid with dimensions $(9.07 \times 0.77 \times 0.9)m$, and is located at the origin. This is equal to filling the wave tank with water up to a level of $d = 0.9m$. This cuboid would also includes part of the beach, however since this volume is defined outside the domain, olaFlow will discard it.
The initial values for the velocity, dynamic pressure and displacement are zero in all three directions, everywhere. Therefore, also the wavemaker is still in its initial position at an angle of 0°. The hydrostatic pressure is non-zero, which is directly computed after defining $g = -9.81m/s^2$ in the z-direction. Finally, the k and ω variables requires a non-zero number in order to avoid an error due to division by zero. This stems from the fact that the turbulence is finally modelled as additional viscosity. Since the initial state is stationary, no turbulence should be present. Therefore, for the initial condition very small numbers are chosen, with $k = 1 \times 10^{-8}m^2s^{-2}$ and $\omega = 1 \times 10^{-3}s^{-1}$ throughout the domain including the boundaries.

Boundary	Volume of Fluid (α)	Pressure ($p_{\rho gh}$)	Velocity (U)
Wavemaker	Zero-gradient	Fixed-flux	Moving-wall
Beach	Zero-gradient	Fixed-flux	Fixed-value
Bottom	Zero-gradient	Fixed-flux	Fixed-value
Atmosphere	Inlet-outlet	Total-pressure	Pressure-inlet/outlet
Wall 1	Zero-gradient	Fixed-flux	Fixed-value
Wall 2	Zero-gradient	Fixed-flux	Fixed-value
Wall 3	Zero-gradient	Fixed-flux	Fixed-value

Table 5: Conditions on the boundaries for the volume of fluid, pressure and velocities.

Boundary	Turbulence (k)	Turbulence (ω)	Displacement (ΔX)
Wavemaker	Inlet/outlet	Inlet/outlet	Wavemaker-movement
Beach	kqRWallFunction	omegaWallFunction	Fixed-normal-slip
Bottom	kqRWallFunction	omegaWallFunction	Fixed-normal-slip
Atmosphere	Inlet/outlet	Inlet/outlet	Zero-gradient
Wall 1	kqRWallFunction	omegaWallFunction	Fixed-normal-slip
Wall 2	kqRWallFunction	omegaWallFunction	Fixed-normal-slip
Wall 3	kqRWallFunction	omegaWallFunction	Zero-gradient

Table 6: Conditions on the boundaries for the $k-\omega$ SST model parameters and the displacement.

5.5 Mesh

The domain is discretized into cells, a process called meshing. The final solution is highly dependent on the quality of the mesh. A good quality mesh is defined as a mesh that is refined sufficiently such that an increase in the number of cells will not yield a significant change in results or accuracy. An increase in number of cells will come with a penalty in computational cost, therefore it is important to acquire a good result with a minimum number of elements. OpenFOAM and therefore also olaFlow, performs best using an as simple-as-possible mesh using quadrilaterals denoted as a "block mesh" within the software. The block mesh prefers orthogonal cells. Solutions are computed efficiently, and sufficiently small quadrilaterals are adequate at capturing wave dynamics.

5.5.1 Interface

In wave dynamics modelling, a rule of thumb is to have approximately 80 cells along the wavelength, and 15 cells along wave height at the wave fluid surface [27]. This amount of cells should be adequate at calculating the wave height in a good order of magnitude as well as capture properties such as wavelength, celerity and periodicity. Additionally, since the magnitude of the velocity is decreasing towards the bottom of the wave tank, the mesh size can be coarser towards the bottom. Especially for deep water conditions, the bottom should have a negligible influence on the waves. This will result in high aspect ratio cells, where the length in the x-direction is much longer than the height in the z-direction. Contrary to typical CFD, this is not an issue for wave dynamics. This is because the scale of effects in the wave height direction are much smaller than the effects on the scale of the wavelength. The final mesh has 40 cells in the expected wave height, and 88 cells in the predicted wavelength. The resulting mesh is shown in Figure 22, where the cell height and width are $0.002m$ and $0.042m$, respectively. Note the additional refinement at the beach, which will be covered in Section 5.5.2.

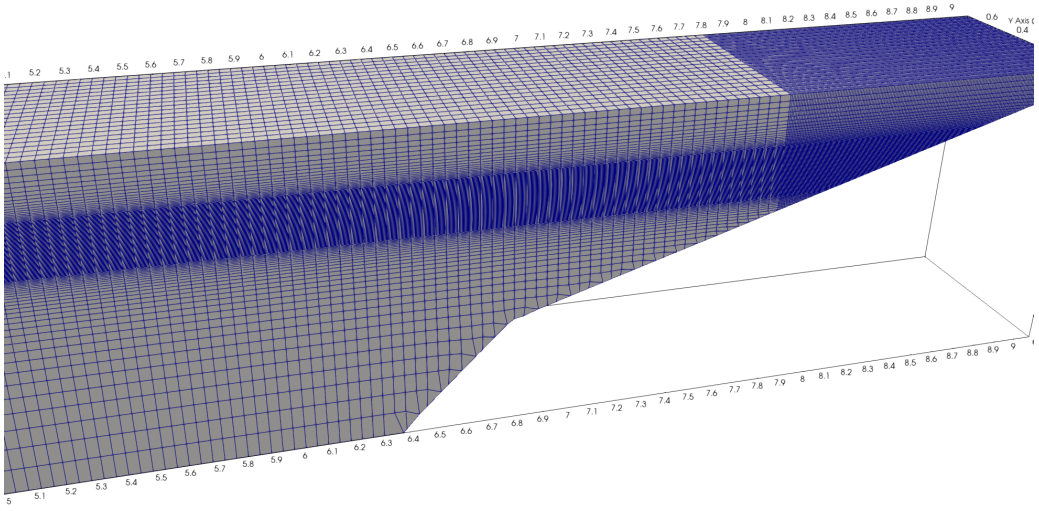

Figure 22: View of (part of) the generated mesh for the numerical model of the wave tank.

Refining the mesh towards the water surface, has the additional effect that the fluid transition layer representing the interface is improved. The interface will typically use 2 cells, therefore a finer mesh will represent the interface better, approaching a thin discontinuous layer. The reduction in transition layer thickness is shown in Figures 23 and 24.

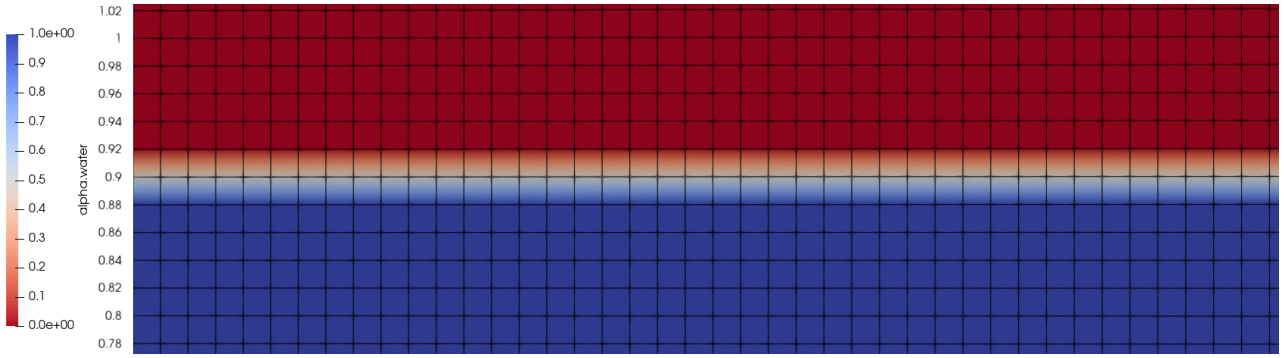

Figure 23: View of the mesh at the interface between water (blue) and air (red), for an unrefined mesh with cell height of $0.02m$.

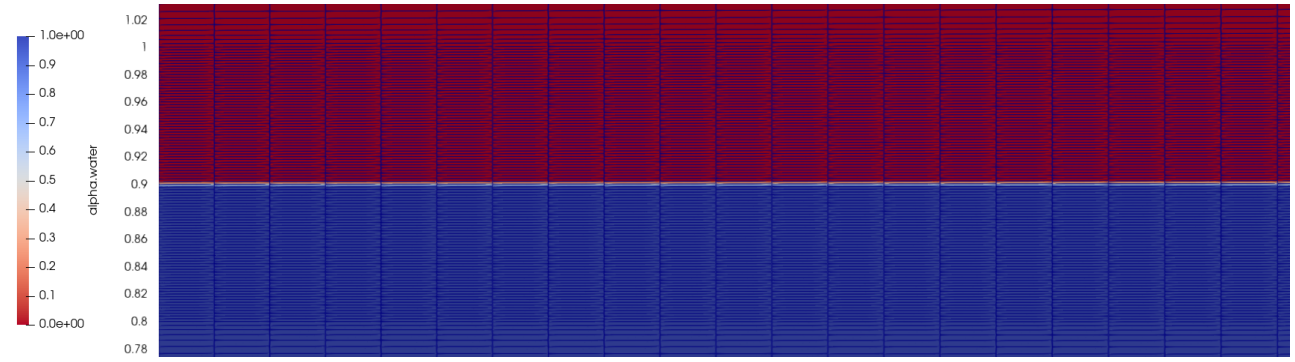

Figure 24: View of the mesh at the interface between water (blue) and air (red), for a refined mesh with cell height of $0.002m$.

5.5.2 Absorbing beach

At the end of the wave tank, the waves crash. This is where most of the turbulence is expected, which is by definition a more chaotic type of flow. Due to the unpredictable nature of the flow at the beach, small scale flows can influence how the wave are reflected off the beach. Therefore, at the beach an additional refinement is applied. The refinement is shown in Figure 25.

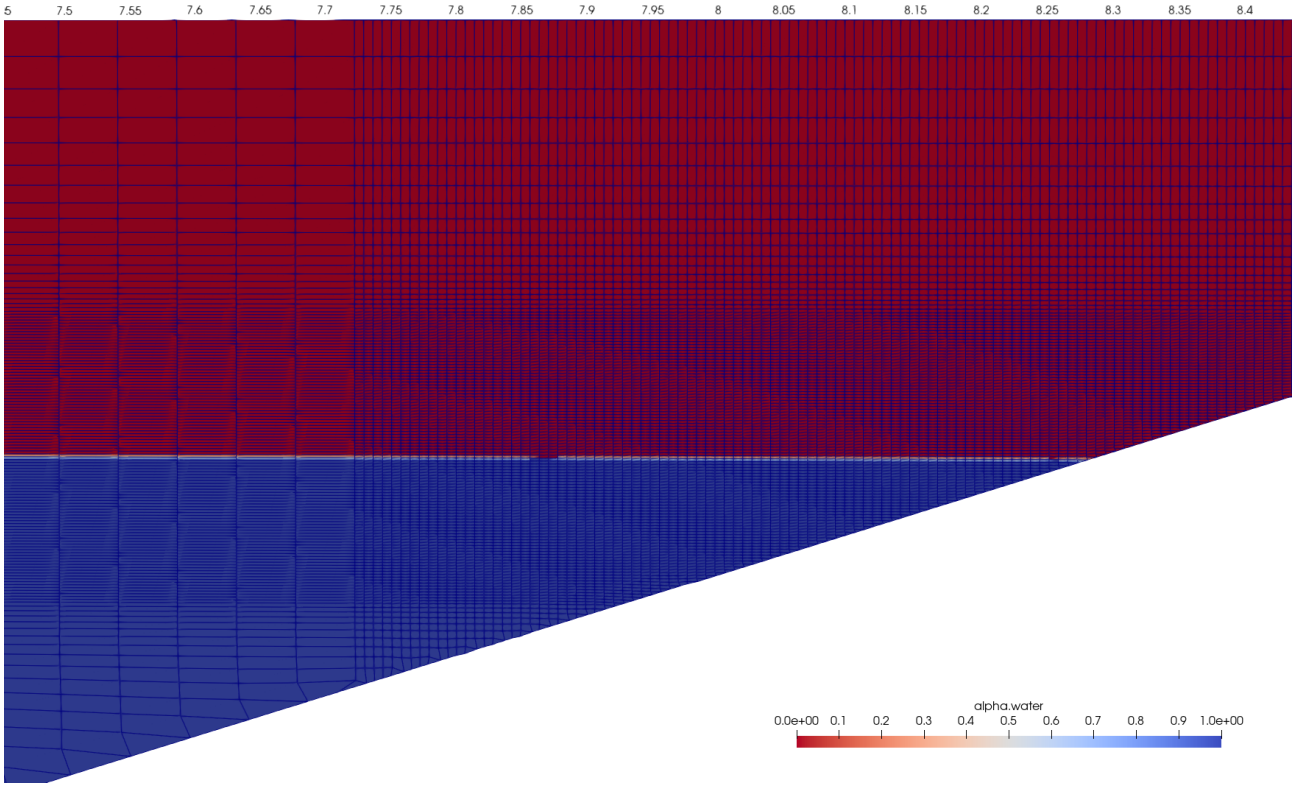

Figure 25: View of the mesh at the beach where additional local refinement is applied.

It can also be observed that along the domain edge at the beach the cells are skewed as a result of the rectangular cell shape. In theory this should not pose accuracy problems, however some cell volumes could approach zero, which would make the computational cost approach infinity. Moreover, the cells could become inverted during generation, because they are instructed to "snap" to the domain boundary. Non-orthogonal angles could pose the same issue. OpenFOAM supplies a "checkMesh" command which will evaluate the quality of the mesh on a few conditions in order to predetermine whether the simulation has a good probability of converging as a result of the generated mesh. This mesh was made conform the checkMesh requirements. The resulting mesh has a total of 750880 cells.

5.6 Foam Layer

In the experimental wave tank, a foam layer is present at the beach in order to mitigate the reflection. The foam layer is modelled in olaFlow as a porous layer region at the beach. The foam layer is located at the same position as in real life, with a layer height of $0.07m$. The surface profile of the foam layer is omitted, since the current mesh will not allow such fine geometry definition, as will be seen shortly. The foam layer implementation is illustrated in Figure 26. The foam layer's properties are unknown, but for the model default olaFlow values were used. The porosity was set at 0.49, with the mean nominal diameter being $0.0159m$. The default porosity modelling values are $\alpha = 50$, $\beta = 2$ and $C = 0.34$.

Figure 26: Location of the foam layer (black) in the numerical model domain.

Due to limitations of the mean cell size in the domain, the foam layer is distorted during discretization. The resulting foam layer is shown in Figure 27, where the color grading indicates the level of porosity. It can be seen that the mesh is unable to follow the porous surface in the regions where the mesh is not, or partially, refined. This is because of the inclination of the beach to the foam layer in tandem with the use of rectangular mesh cells. In the refined region where the waves are supposed to crash, the foam layer was generated as defined.

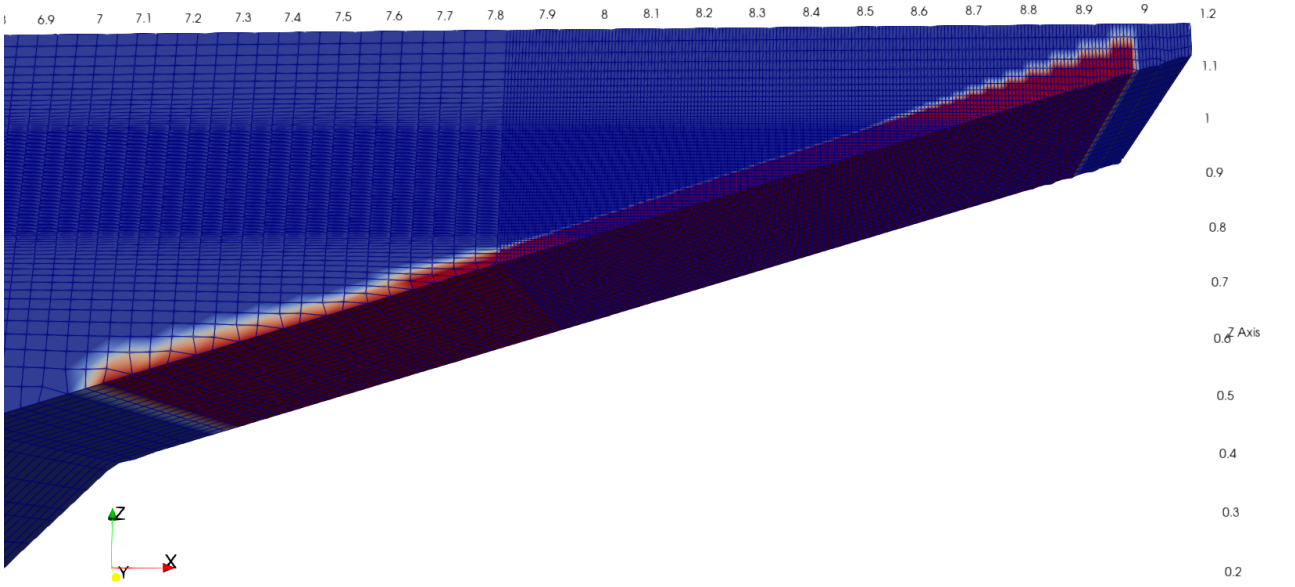

Figure 27: The porosity plotted in the domain together with the mesh, to show the generated foam layer as a consequence of meshing the domain.

5.7 Domain Decomposition

Finally, the domain is decomposed into sub domains. This is done in order to achieve higher computational efficiency by parallel computing the solution of every sub domain at the same time. The solutions at the boundaries of one sub domain are than used as initial values for the adjacent domains. This way, the computational time is severely reduced. The domain is decomposed into 24 sub domains. Therefore, the model is run on 24 separate processors. This is proven to be the most efficient, since the high performance cluster where the computation is run has nodes with 24 processors. Consequently, the decomposition requires exactly 1 node, so no inter-node information exchange is required which decreases the overall computational efficiency due to read/write times. Moreover, more resources yield higher queue times before the computation is started. Therefore, it is overall quicker to run on 24 cores for this mesh rather than using more cores or even nodes. The decomposition of the domain is shown in Figure 28, where every sub domain has approximately an equal amount of cells. Therefore, more domains are located in the center and the beach, where the mesh is refined.

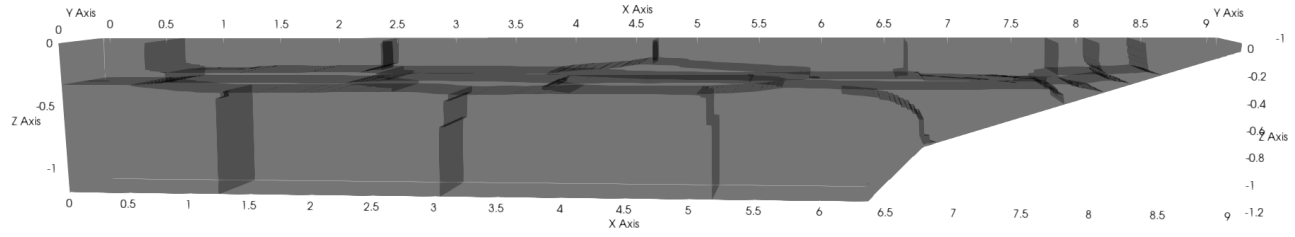

Figure 28: View of the 24 sub domains after decomposition for parallel computing.

6 Model Validation and Preliminary Results

In this section, validation of the numerical model is done using experimental data of the wave tank which are documented in the work of J. Brenes and M. Manresa [4; 5]. Moreover, linear wave theory is consulted to determine the physicality of the model. Additionally, this section will describe some preliminary results from which a set of different model configurations are derived to investigate. For the validation, the wavemaker movement in the numerical wave tank is created identical to the movement performed in the experimental results which is described in the thesis of Manresa:

$$\alpha(t) = -\left[4sin\left(t\frac{2\pi}{1.62}\right) + 3.4\right], \tag{52}$$

where $\alpha(t)$ is the angle of the wavemaker with respect to the equilibrium position, as a function of time. This is an asymmetrical movement, where the wavemaker moves periodically from a back-angled position to passing the equilibrium. The periodicity of the wavemaker movement will also determine the wave period, which is $1.62s$. The wavemaker movement is illustrated in Figure 29.

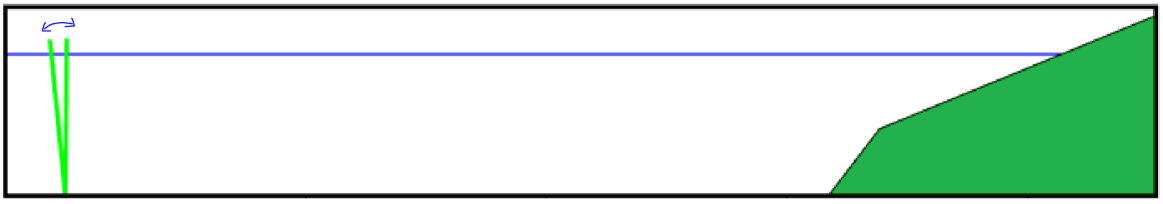

Figure 29: Illustration of the asymmetrical movement of the wavemaker [5].

The reported wave height corresponding to this wavemaker movement is $0.08m$ with a period of $1.62s$. These values correspond to a full scale wave with an height of $2.8m$ and a period of $9.584s$ scaled 1:35 using Froude's scaling law. It must be noted that the validation of the initial numerical model is performed without additional reflection mitigation methods such as the foam layer that was present in the wave tank during the physical experiments reported. Furthermore, it must be noted that the reported empirical values from the theses are reported as a single digit number without any indication about the uncertainty or measurement method. In order to investigate the effect of reflection over time, the model was run for 90 seconds. The solutions were saved and evaluated at intervals of $0.1s$ in order to save space. Note that the time step is adaptive and dependent on the speed of the flow of information through the cells using the Courant number. This is independent of the save interval.

6.1 Wavelength

Previous theses do not report the observed wavelength of the waves. However, from Equation (29), we can calculate the theoretical celerity c for a wave with a period of $1.62s$ in a tank with depth $0.9m$ to be $(2.298 \pm 0.002)ms^{-1}$, where the uncertainty is the result of the approximation described in Equation (28). Consequently, the wavelength is given by

$$\lambda = Tc, \tag{53}$$

with λ the wavelength of the wave and T the wave period. For a period of $1.62s$ with a celerity of $2.298ms^{-1}$, the theoretical wavelength equals $(3.723 \pm 0.002)m$.
The wavelength in the numerical model was measured from crest to crest. A measurement of multiple wavelengths over a larger length would have been preferred, however the wave tank is not long enough

to fit two or more wavelengths. The wavelength was measured to be $(3.71 \pm 0.02)m$, which is illustrated in Figure 30. The measurement was performed on developed waves around $10s$, where the reflection is not affecting the waves significantly yet. Therefore, the wavelength is consistent with linear wave theory. This also implies that the celerity is also consistent with theory. Consequently, the wave does not satisfy the deep water condition, since the depth $(0.9m)$ is not equal or larger than half the wavelength. This is also shown in Section 6.6. Additionally, the beach should be at least half the wavelength for optimal absorption. The beach is $1.31m$, which is less than half the wavelength. Therefore, sub optimal wave absorption is expected.

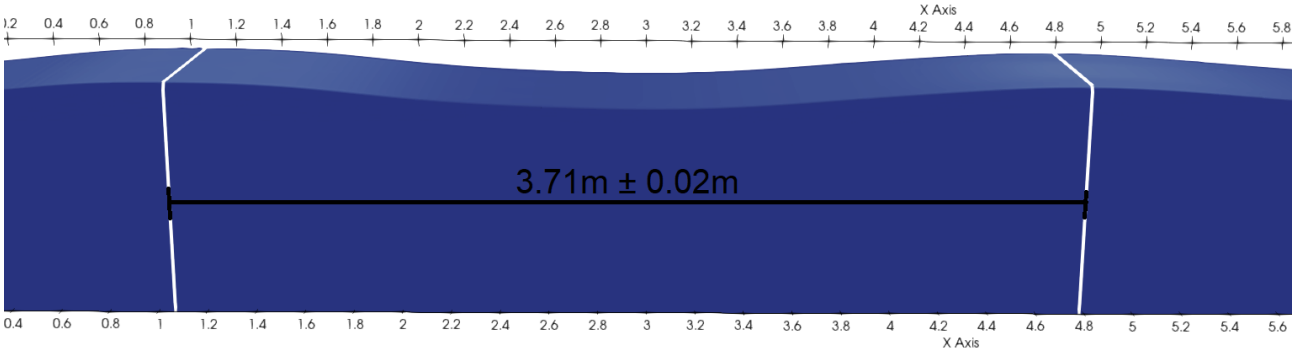

Figure 30: Crest-to-crest wavelength measurement in the numerical model.

6.2 Wave Amplitude and Reflection

The average wave amplitude throughout the wave tank was determined to be $0.0398m$, with a corresponding wave height of $0.0796m$. It was measured from surface elevation data between $(0-6)m$ from the wavemaker, to avoid increased wave heights from the beach. The observed value deviates from the reported experimental value of $0.08m$ by 0.05%. However, the wave amplitude is not uniform, but varies greatly at various locations throughout the tank. In Figure 31, the surface elevation over time is plotted at two locations in the numerical wave tank; at $4.5m$ and $5.5m$. These are locations where the wave should be fully developed, but should not yet feel the beach. Therefore these should be representative for the wave properties. The value of the amplitude is calculated from tracking the water surface coordinates. The depth $(0.9m)$ is then subtracted from the set of coordinates and is averaged over the y-axis (width), yielding a single amplitude value. Assuming the amplitudes are consistent over the width of the wave tank is a reasonable assumption as will be discussed in Section 6.6.1. The data was saved every $0.1s$.

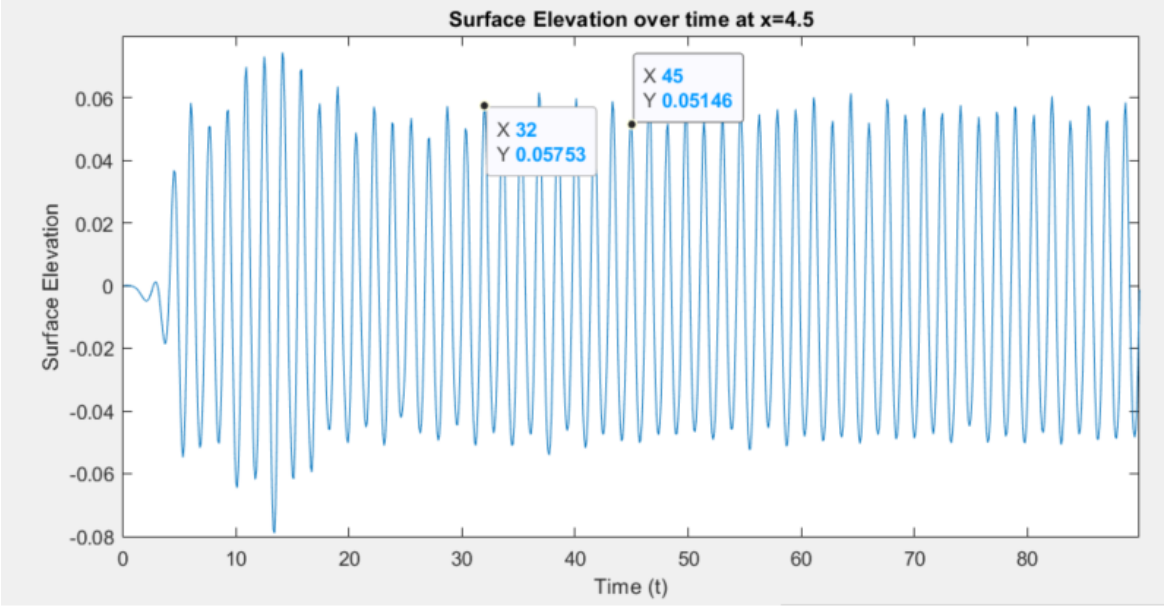

(a) The surface elevation with respect to the mean surface level over time, at $4.5m$ from the wavemaker.

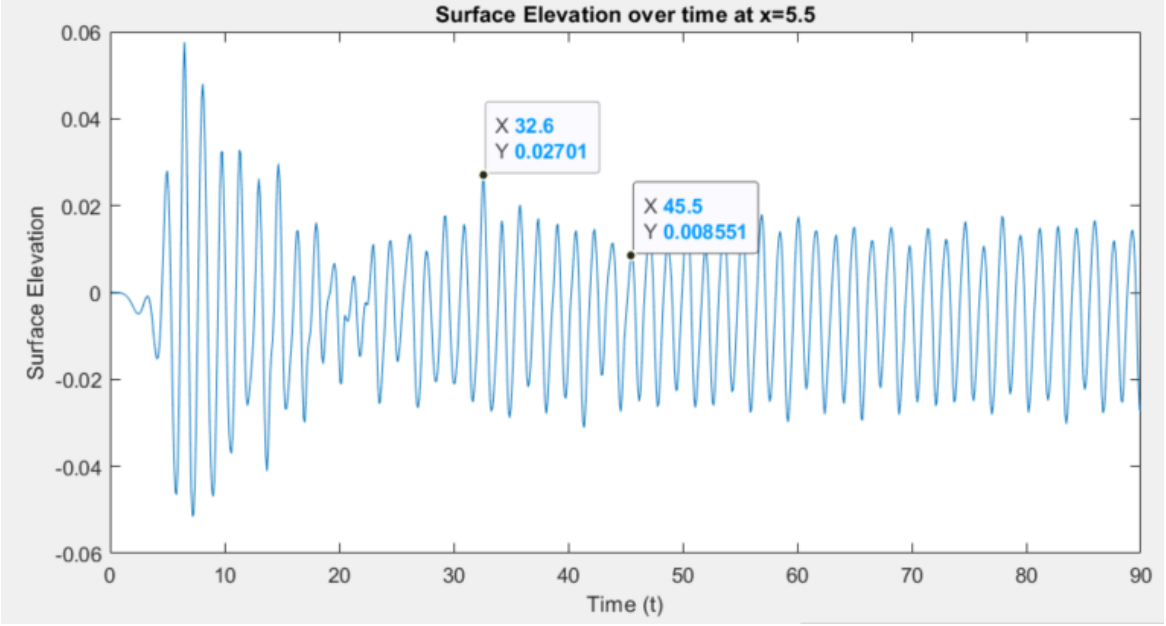

(b) The surface elevation with respect to the mean surface level over time, at $5.5m$ from the wavemaker.

Figure 31: Two points where the developed free surface elevation is determined.

First of all, a large deviation in surface elevation is observed in the first 30 seconds, where the waves are started to be generated. First the wavemaker has to start generating the waves (0-7 seconds). The first few waves will gradually increase in height. Then the wave heights for both locations decrease again, until it stabilizes. After approximately 30 seconds, the surface elevation is relatively constant for both locations. This is due to the interaction between the incident and reflected waves becoming more stabilized over time. In the stabilized state ($t > 30s$), it can be seen that the average wave amplitude differs between the two locations. The wave amplitudes at $x = 5.5m$ are consistently lower

than the wave amplitudes at $x = 4.5m$. Furthermore, the wave amplitude also varies as a function of time at a both locations. This is true throughout the wave tank with wave amplitudes varying between $(0.0118 - 0.0667)m$ for different locations. This is shown in Figure 32, where the amplitudes are extracted from the surface elevation data for every location, averaged over all periods and plotted as a function of location in the wave tank. Note that towards the end of the wave tank this graph is not representative of a wave amplitude anymore, since this is where the waves crash at the beach, therefore it is omitted. Additionally, the amplitude value for the period with the highest and lowest amplitude for each location are plotted as maximum and minimum, respectively. This indicates the range of amplitudes that occur. Finally, the reported empirical value is plotted as a constant wave amplitude, as well as the total average amplitude throughout the wave tank. Note that for perfect regular waves, without any reflection, the wave amplitude should not vary throughout the wave tank and should result in a straight line in the graph.

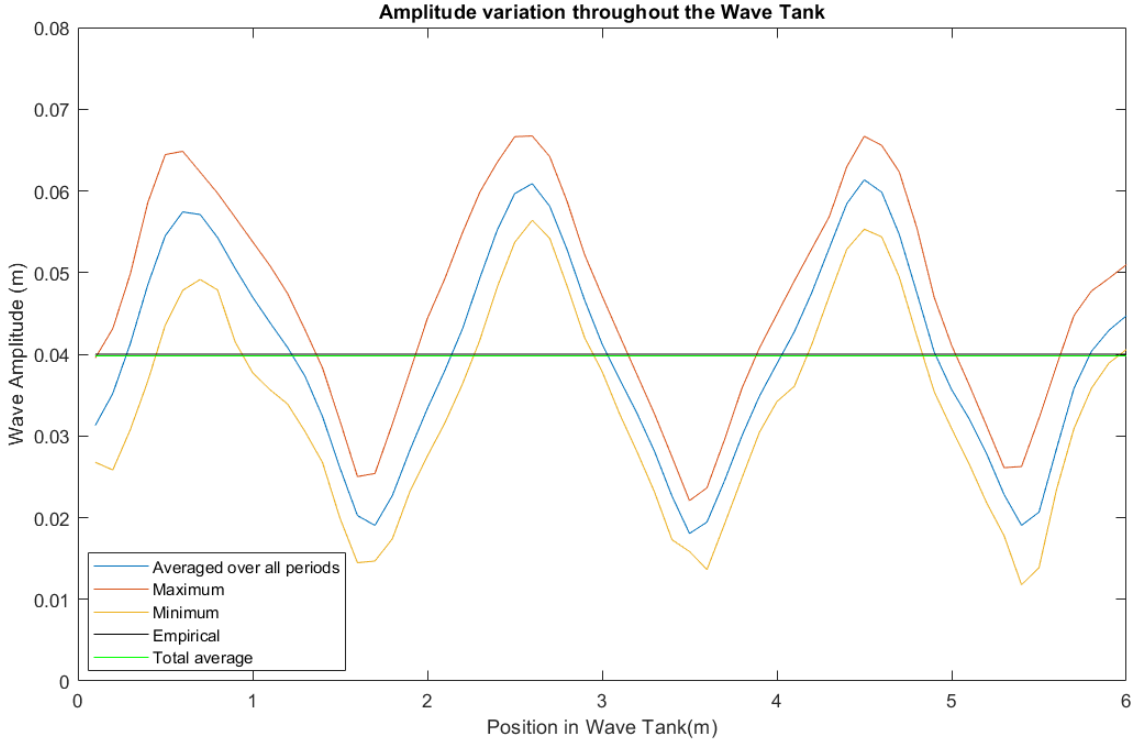

Figure 32: The wave amplitude plotted as a function of location in the wave tank.

The amplitude variation appears to be periodic as a function of distance. Note that the data was extracted at intervals of $0.1m$, therefore the curves are not completely smooth. The variation of the wave amplitude along the length of the wave tank is the result of reflection. The incident waves with amplitude $A1$ are partially reflected at the beach, and the reflected waves travel back through the wave tank with the same velocity. Since a part of the wave is absorbed, the reflected waves have less energy, thus a lower amplitude $A2$. The waves form a superposition, which is known as a partial standing wave. The amplitude of the wave is then dependent on the sum and difference of the amplitudes of the incident and reflected wave. This is illustrated in Figure 33.

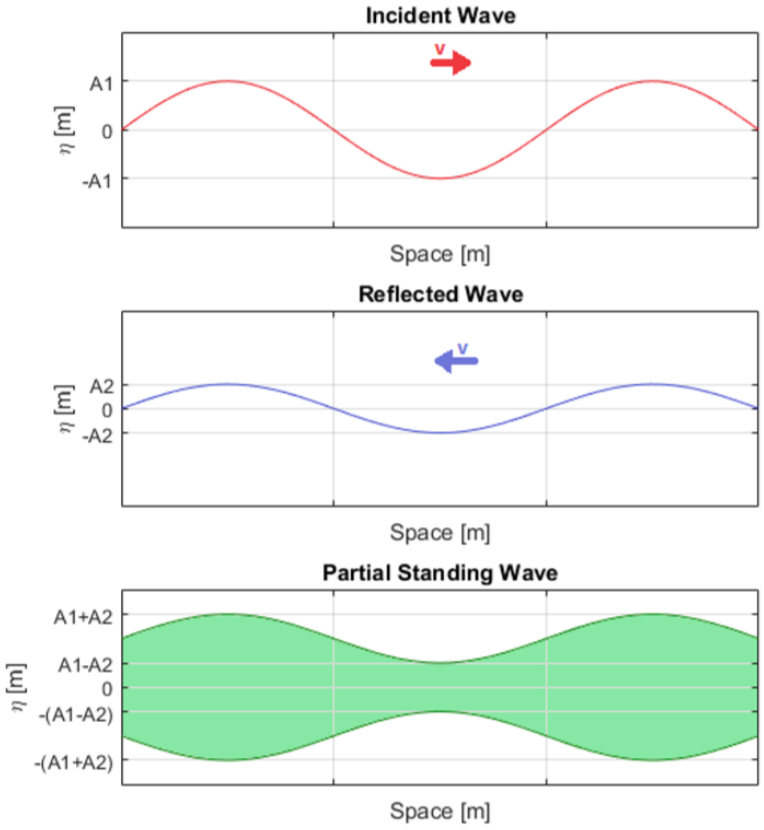

Figure 33: Illustration showing the incident and reflected wave that form a superposition in the form of a partial standing wave [5].

Note that the resulting variation of amplitudes is also periodic, due to the fact that both waves travel with the same speed and have the same periodicity. The observed wavelength of the standing wave is $(1.9 \pm 0.1)m$, which is consistent with being half the wavelength of the incident wave. The points in space where the wave amplitude is lowest $(A1 - A2)$ are denoted the nodes of the partial standing wave. The points with the highest amplitude $(A1 + A2)$ are the anti-nodes. The amplitude of the of incident and reflected waves can be calculated from the observed values of the nodes and anti-nodes at positions until and including $6m$, to avoid interactions with the beach. The observed values for the nodes are averaged to arrive at $A1 - A2 = 0.0187m$. The average amplitude of the anti-nodes equals $A1 + A2 = 0.0607m$. Therefore, the amplitude of the incident and reflected waves are $A1 = 0.0397m$ and $A2 = 0.0210m$, respectively. There is only a marginal difference between the average observed wave amplitude $(0.0398m)$ and the calculated original wave amplitude of the incident wave without reflection$(0.0397m)$. In theory the average wave height should be equal to the wave amplitude of the original wave. In this case, the difference is negligible if we take the cell height $(0.002m)$ into account. The reflection in the tank can be quantified using the ratio of amplitudes, such that

$$R = \frac{A2}{A1}, \tag{54}$$

with the reflection coefficient R equating 0.529. The energy in a wave is given by

$$E = \frac{1}{2}\rho g A^2. \tag{55}$$

The energy in a wave scales quadratically with the amplitude. 52.9% of the amplitude is reflected, therefore 28.0% of the incident wave energy remains in the reflected wave. Moreover, the waves crash at the beach releasing energy in a disordered manner, creating additional irregular waves that also travel in a direction opposite to the incident wave, but which are not taking into account in this calculation. These additional back traversing waves could also explain part of the variation in wave amplitude between locations and over time.
Please note again that the empirical value of the observed wave height in the experimental wave tank was only stated as a single digit number without any indication of uncertainty or note of variation as a function of location. An earlier thesis by M. Visser of the wave tank did report observing reflection effects in the surface profile of the waves, see Figure 34 [28]. However, no quantification of the reflection was reported. Furthermore, in the numerical model used for validation the absorbing foam layer is still absent, therefore the reflection and its effect on the observed wave amplitude should still be exaggerated with respect to the empirical values, where the foam layer was implemented.

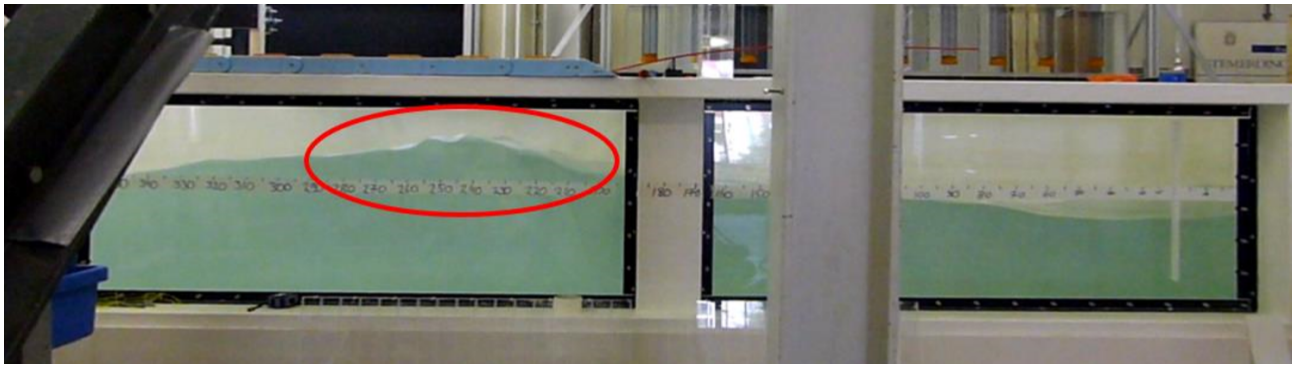

Figure 34: A picture provided by M. Visser in his thesis reporting the observation of reflection in the surface profile [28].

Finally, wavemaker theory predicts wave amplitudes of $0.05m$ for flap wave makers with a stroke corresponding to this angle using Equation (35). The observed average amplitude is 20.0% lower, however wavemaker theory is defined for symmetrical wavemaker movement. Therefore, it is possible that wavemaker theory overestimates the wave amplitude if the wavemaker movement is not symmetrical, since both the physical and numerical model show a lower wave amplitude. Another hypothesis is that the reflection not only creates a partial standing wave, but that the interaction between the incident and reflected waves also decreases the average wave height.

6.3 Fast Fourier Transform

The Fast Fourier Transform (FFT) is an algorithm to compute the Discrete Fourier Transform (DFT) to convert data in a certain domain to the frequency domain. In this case, the time domain is converted. Transforming the data into a frequency domain reveals periodicities in the data. The DFT is given by

$$F_n = \sum_{k=0}^{N-1} f_k e^{-i2\pi kn/N} \qquad \text{with} \quad n = 0, ..., N-1, \tag{56}$$

where f_k are the individual data values at time $t_k = k\Delta t$ with $k = 0, ..., N-1$. N is the data size and F_n are the transformed values. The data is sampled using a sampling rate of $67Hz$. The transformed

data is symmetric, therefore only a single side of the transformed values will be shown. The single-sided transformed data at $x = 4.5m$ is shown in Figure 35. Note that the FFTs of other locations yielded similar results.

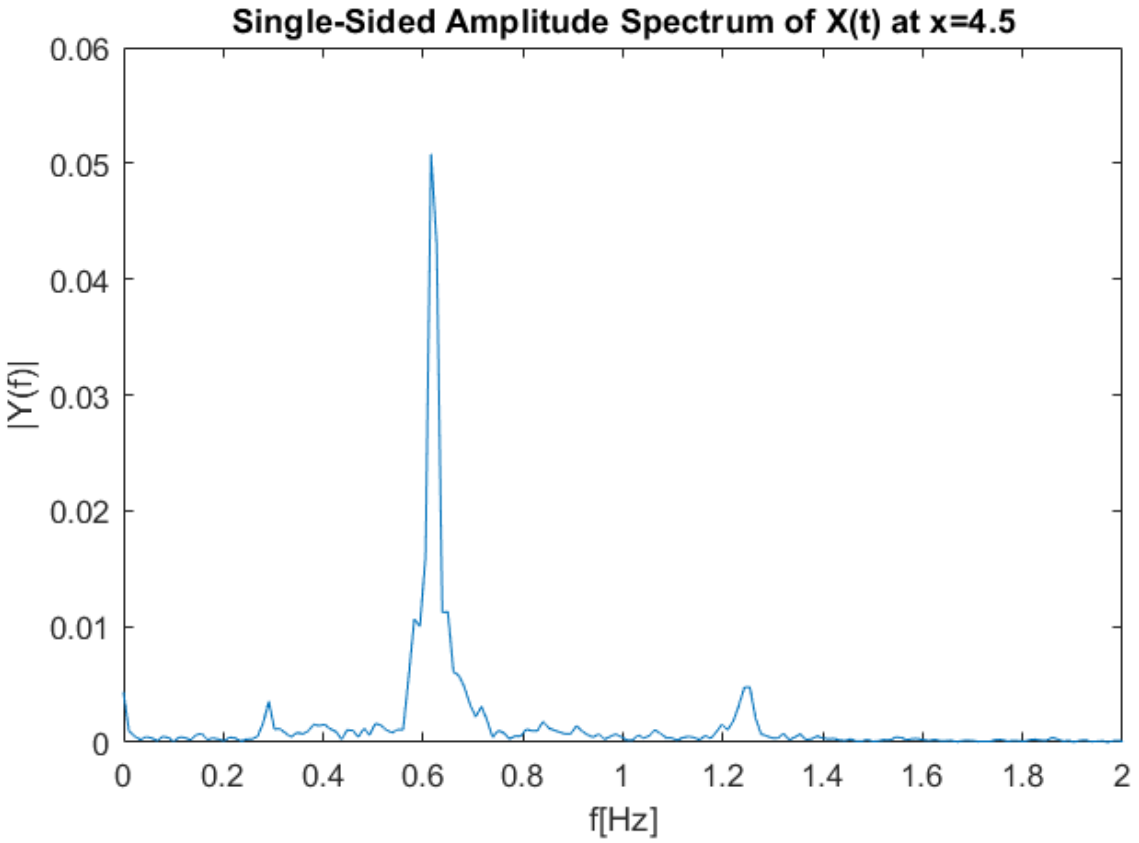

Figure 35: Fast Fourier transform of the surface elevation at $x = 4.5m$

In the plot, the periodicities are plotted as frequencies in Hz with their relatively strength $|Y(f)|$. The main peak is the wave frequency. Note that the waves have a periodicity of $T = 1.62s$, equating to a frequency of $f = 0.62s^{-1}$, which is where the largest peak is located. This is the periodicity of the incident wave, as well as of the reflected wave. This also known as the first harmonic. At double the frequency $f = 1.24s^{-1}$ of the first harmonic we find the second peak. This corresponds to the second harmonic, indicating that a complex wave field is formed. This frequency is related to the partial standing wave. It was observed that the wavelength of the partial standing wave is half of the incident wavelength, therefore the frequency is doubled. Therefore, the partial standing wave is oscillating in the second harmonic of the original wave.
Finally, a third peak is observed in the low frequency range at $f = 0.29s^{-1}$. No evidence is present that indicates that this is some sort of zeroth harmonic, where the frequency is half that of the first harmonic. The frequency is also not exactly half that of the main peak. A more probable explanation could be that the waves crashing at the beach flow back, causing effects at lower frequencies than the wave frequency. Another phenomenon observed in closed bodies of water is a long-period wave denoted as a seiche. Seiches are standing waves in a (partially) enclosed body of water which are activated by other waves, often imperceptible to the naked eye [29]. In seiches, the surface elevation at one boundary is elevated slightly and lower at the other boundary with a linear gradient between

them, illustrated in Figure 36.

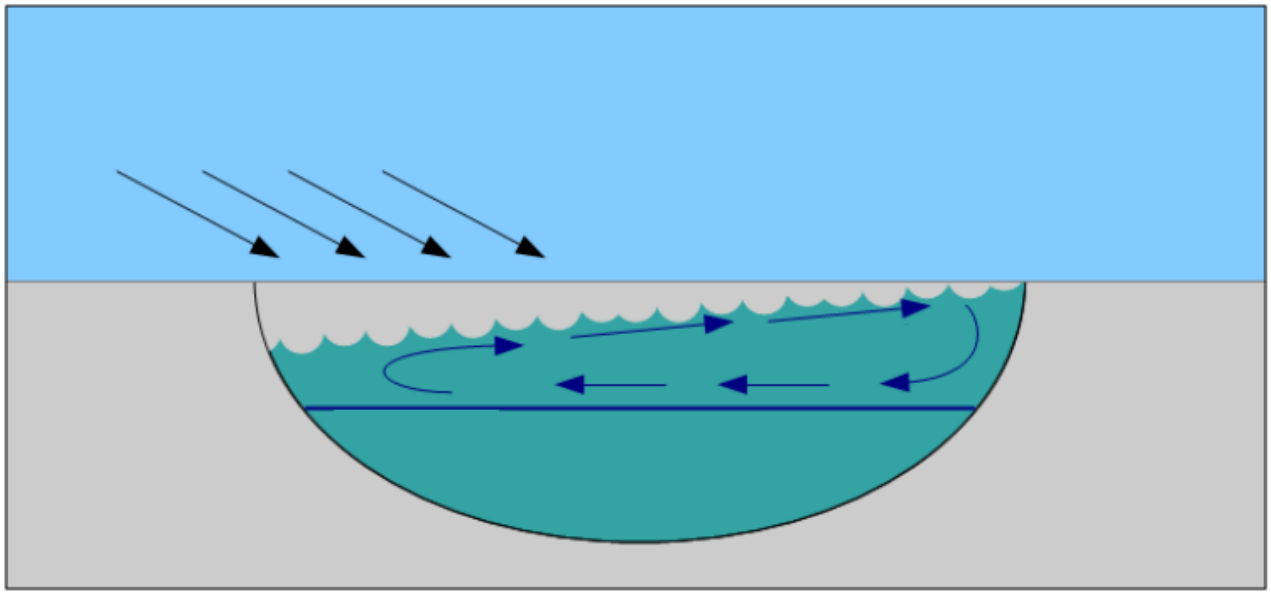

Figure 36: Illustration of an example of a seiche in a close body of water [30].

The period of a seiche can be estimated using the following equation

$$T = \frac{2L}{\sqrt{gd}}, \tag{57}$$

where L is the length of the water enclosure, g the gravitational constant and d the depth of the water. If we neglect the beach, the length of the tank is $6.4m$. For a depth $d = 0.9$, the seiche period should then be $T = 4.51s$, corresponding to a frequency of $f = 0.22s^{-1}$. This is in the same order of magnitude as the observed frequency, however it is significantly smaller. For a higher seiche frequency, the wave tank should be shorter. Therefore it is unlikely that the lower frequency is caused by a seiche, but a similar behaviour could be the cause.
Finally, some higher order frequencies are also expected, since the wave crashes at the beach and flows back, generating small capillary waves on the surface. However, their frequencies will be distributed and they will only be a very small fraction of the total periodicities in the wave tank that it is lost in the noise.

6.4 Pressure

The dynamic pressure $p_{\rho gh}$ is plotted in Figure 37. As expected from linear wave theory, the dynamic pressure is larger at the wave crests. In Figure 38, the total pressure is also plotted. This now includes the hydrostatic pressure, which dominates the pressure profile. The hydrostatic pressure follows the wave profile as is expected since at the crests, a larger volume of water is located at a higher position, therefore ρgh increases.

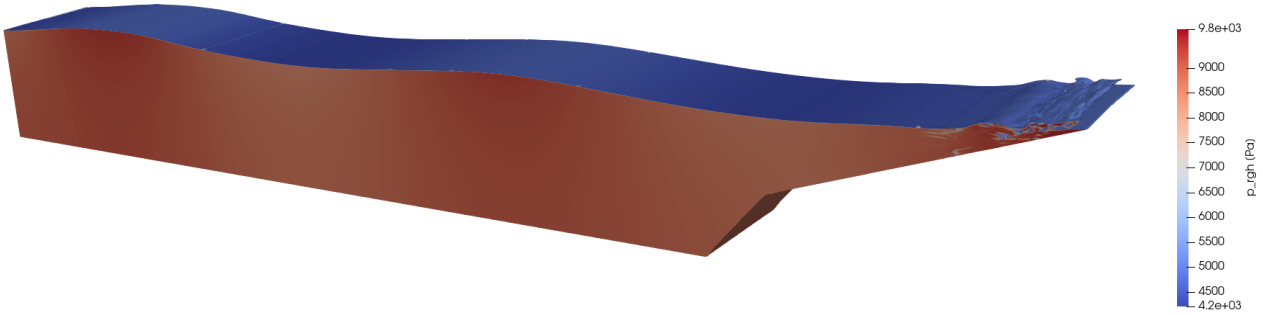

Figure 37: Plot of the dynamic pressure $p_{\rho gh}$ in the wave tank.

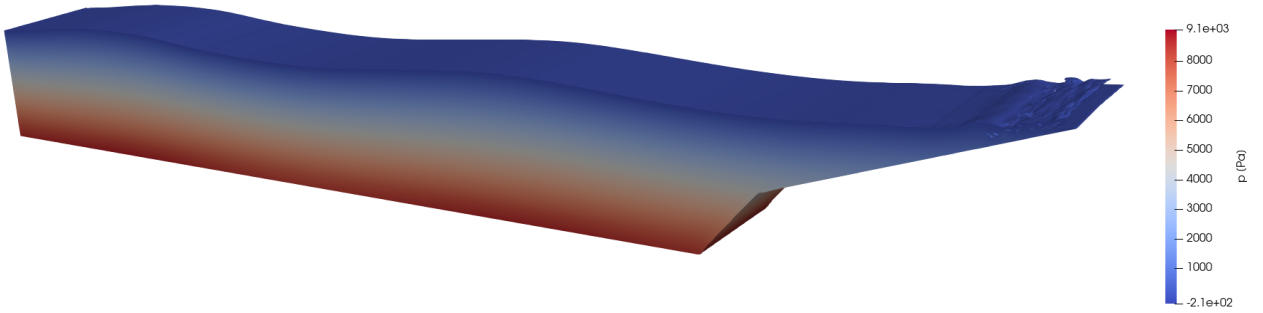

Figure 38: Plot of the total pressure p in the wave tank.

6.5 Turbulence

The model was run with and without the $k-\omega$ SST turbulence model enabled. For both models, the surface elevation at $x = 3.65m$ was calculated as a function of time. Both surface elevations are plotted in Figure 39.

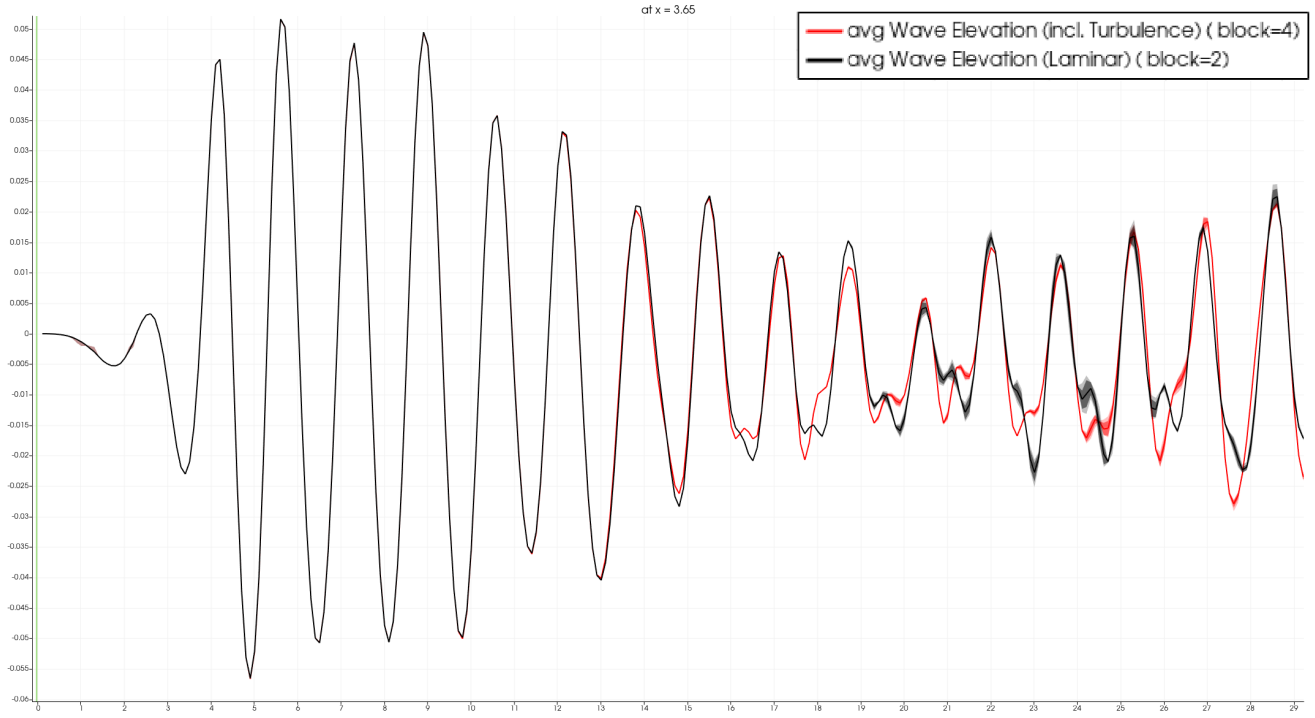

Figure 39: The surface elevation of a model without turbulence modelling and with turbulence modelling, plotted against time at $x = 3.65m$

Plotted in black is the model without the turbulence model, denoted "Laminar". In red is the model with turbulence, denoted "incl. Turbulence". The plotted lines show the wave elevation for $x = 3.65m$, averaged over the width of the tank. The thickness of the line indicates the range of values over the width of the tank at this location. The first thing to observe is that both cases are identical during the first 12 seconds of the simulation. This confirms the hypothesis that the flow is laminar up until the waves crash at the beach, so the turbulence model should be idle and have no effect. After this initial period, the first waves properly crash at the beach, and their reflections travel back over the water surface. From this moment onward, the addition of the turbulence model yields a different result than a fully laminar case. This is also shown in Figure 40, 41 and 42, where the turbulent kinetic energy k, the turbulent energy dissipation rate ω and the resulting additional viscosity ν_t are plotted in the wave tank. It can be seen that the only significant amount of turbulence is present at the beach where the waves crash.

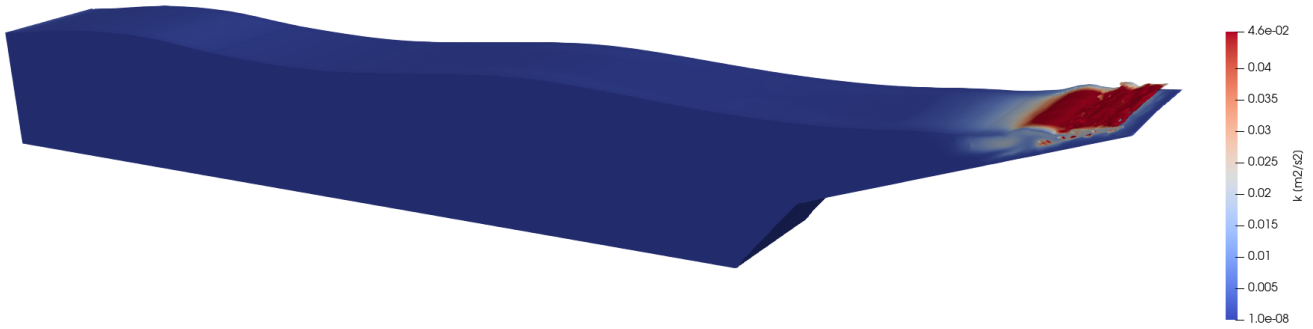

Figure 40: The turbulent kinetic energy k plotted in the wave tank.

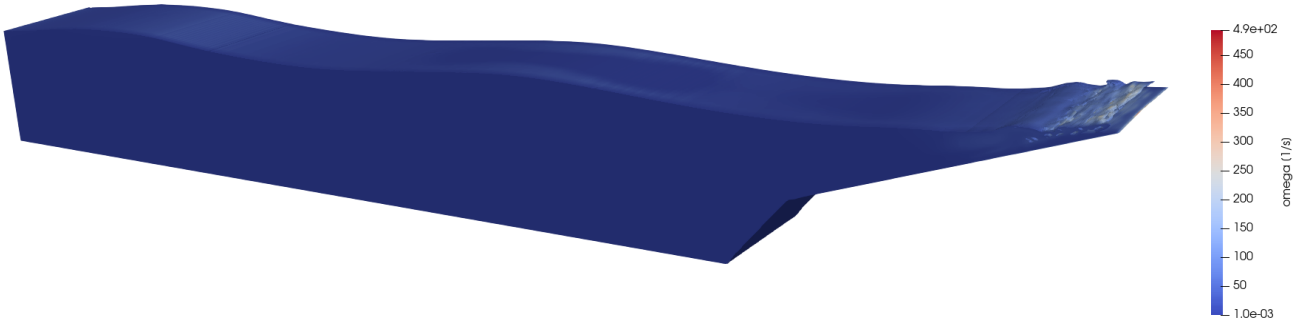

Figure 41: The turbulent energy dissipation rate ω plotted in the wave tank.

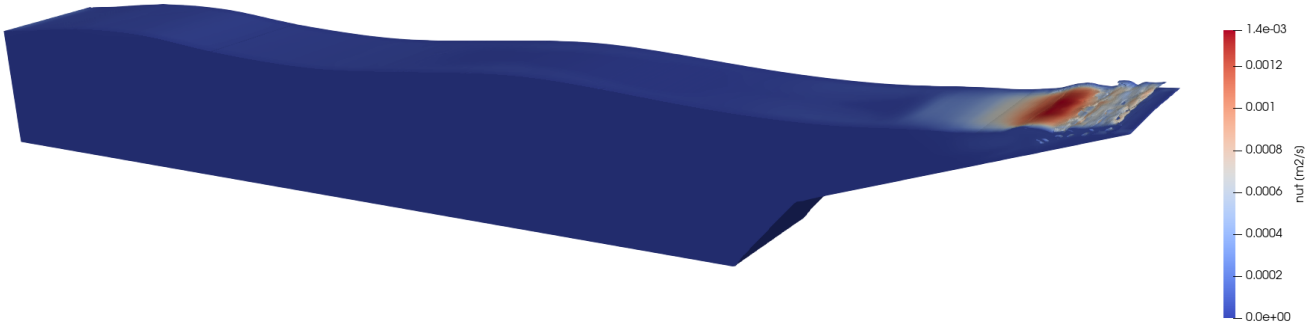

Figure 42: The resulting additional viscosity ν_t due to k and ω plotted in the wave tank.

6.6 Velocity

6.6.1 Wall condition

In order to validate the wall conditions set on the walls of the wave tank, the velocity magnitude is plotted. Figure 43 shows the velocity magnitudes of a wave crest travelling towards the right, as seen from a top view. First of all, it can be seen that at the walls the velocity magnitude equals zero. Moreover, a boundary layer is formed where the velocity magnitude increases towards the center of the wave tank. This is also what is expected for a no-slip boundary condition on the walls. No empirical values or qualitative analysis of the velocity magnitude or wall effects are available. An interesting

additional observation is that there appears a rectangular shape with rounded edges with a close to uniform velocity magnitude in the middle of the wave crest. This is where the velocity magnitude is the largest in the wave.

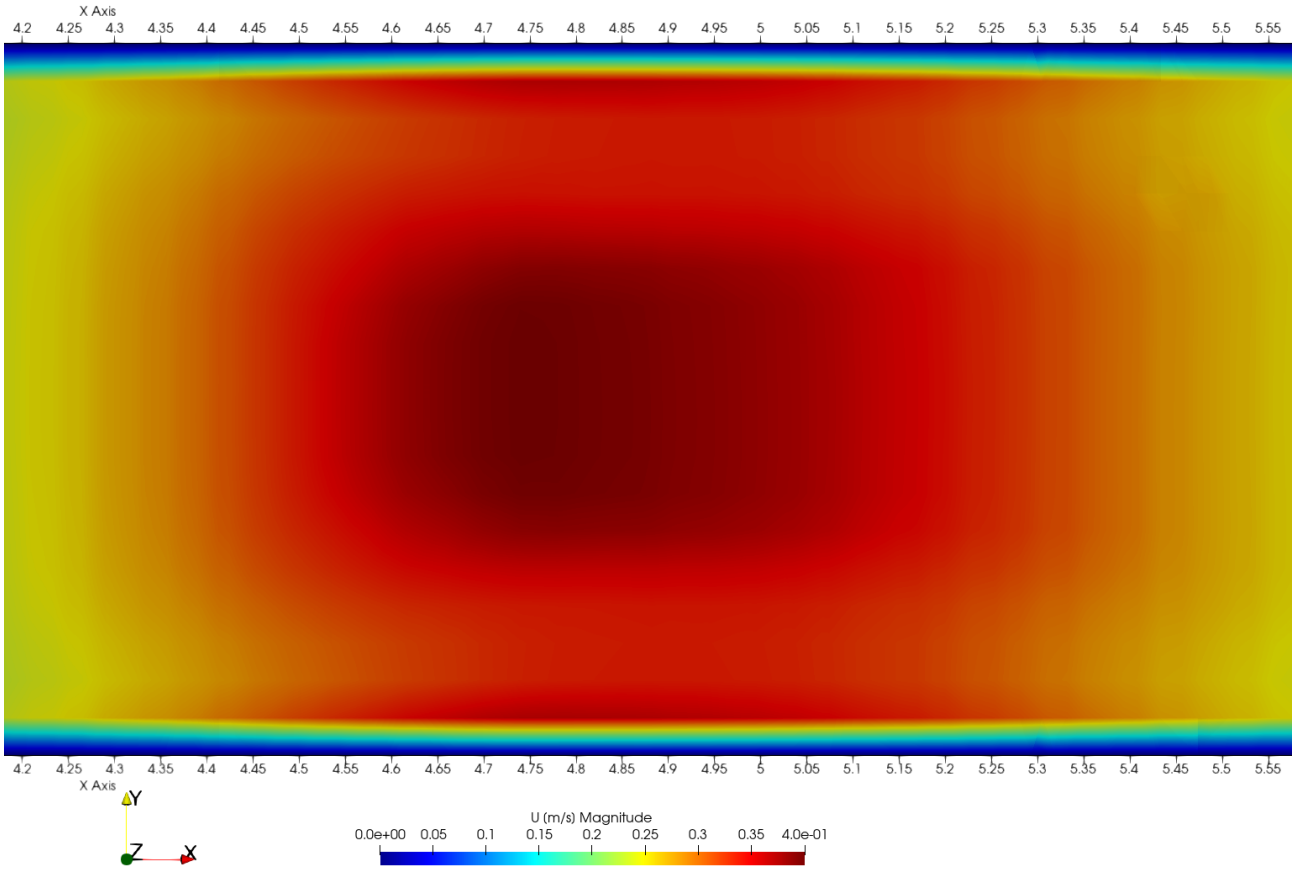

Figure 43: The velocity magnitude plotted on a top view of a wave crest.

Even though a velocity boundary layer is formed at the walls, the wave height remains uniform over the width of the tank. This is shown in Figure 44, where the surface elevation is plotted as a function of distance in the width (y-direction). The plot was generated from a slice of the wave tank at $x = 5.1m$ at $t = 49.1s$. Note the scale on the y-axis, the surface elevation along the width of the tank is variable, but the maximum difference is $1 \times 10^{-4}m$. This is beyond the cell size and therefore a result of the limitations of computational accuracy. Data from other moments in time show similar results.

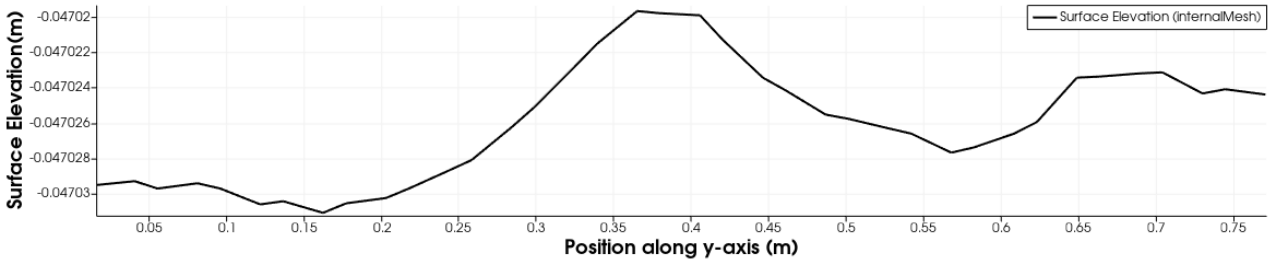

Figure 44: Surface elevation over the width of the wave tank at $x = 5.1m$ at $t = 49.1s$.

6.6.2 Particle Motion

The particle motion is the consequence of the velocity field. The velocity field is plotted in Figure 45. Here the velocity is plotted as a vector. The length of the vector represents the velocity magnitude. The plot was made at $t = 9s$, where the reflection should not have a significant influence on the wave properties yet.

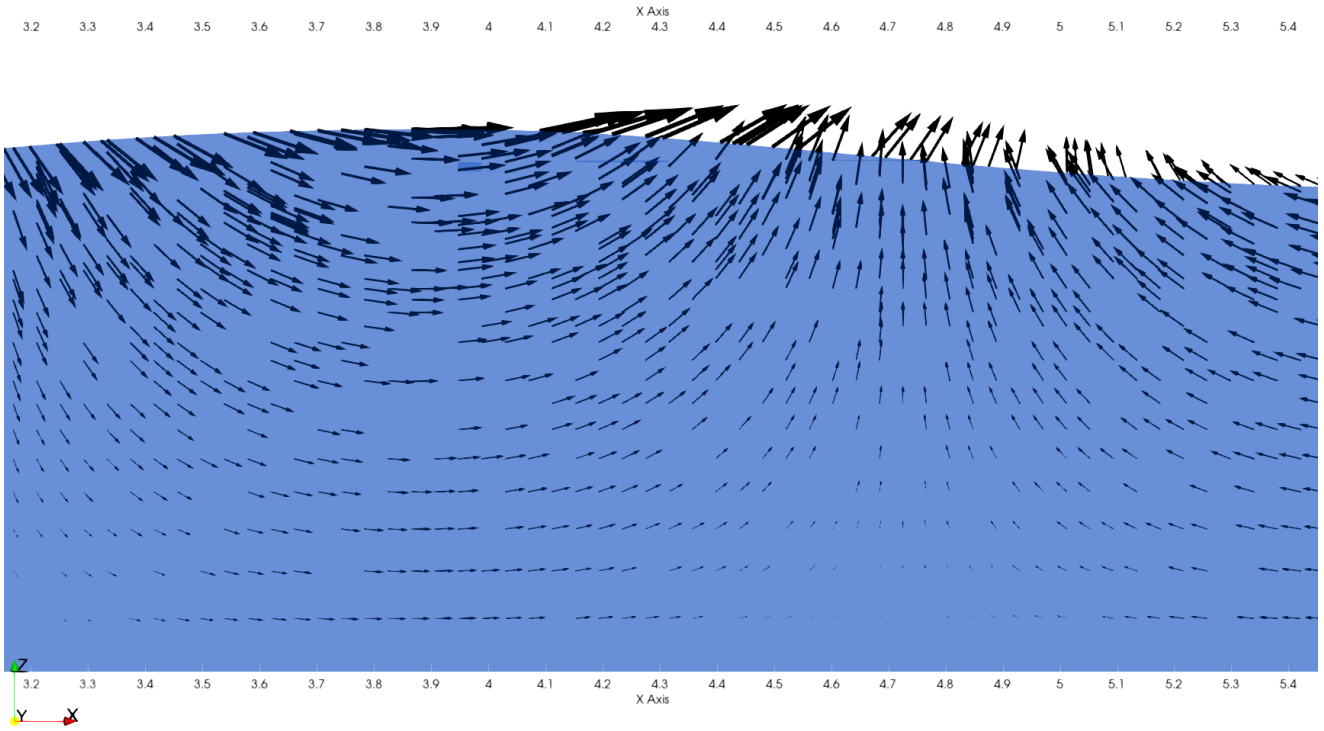

Figure 45: The velocity profile of a section of the wave tank at $t = 9s$.

The first thing to observe is the rotational movement of the particles throughout the wave. As predicted by linear wave theory, the water particles move in an orbital motion periodically as the waves propagate. However, for deep water conditions, theory predicts the particle orbit radius to decrease exponentially towards the bottom, where close to the bottom the radius should be negligible. In the numerical model, the vertical motion of the orbits towards the bottom is negligible, however the horizontal motion is not. Furthermore, the horizontal component of the orbital motion is larger than the vertical component at every water depth. This observation becomes more apparent when the velocity components at a single location are plotted over time. In Figure 46, the velocity profile is plotted over a single slice at $x = 3.85$, where the crest is located at $t = 9s$. The four different plots show the velocity profile at the same location for four quarters of a period. The period of the wave is $1.62s$ and the data is saved in time steps of $0.1s$, therefore every $0.4s$ a plot was created.

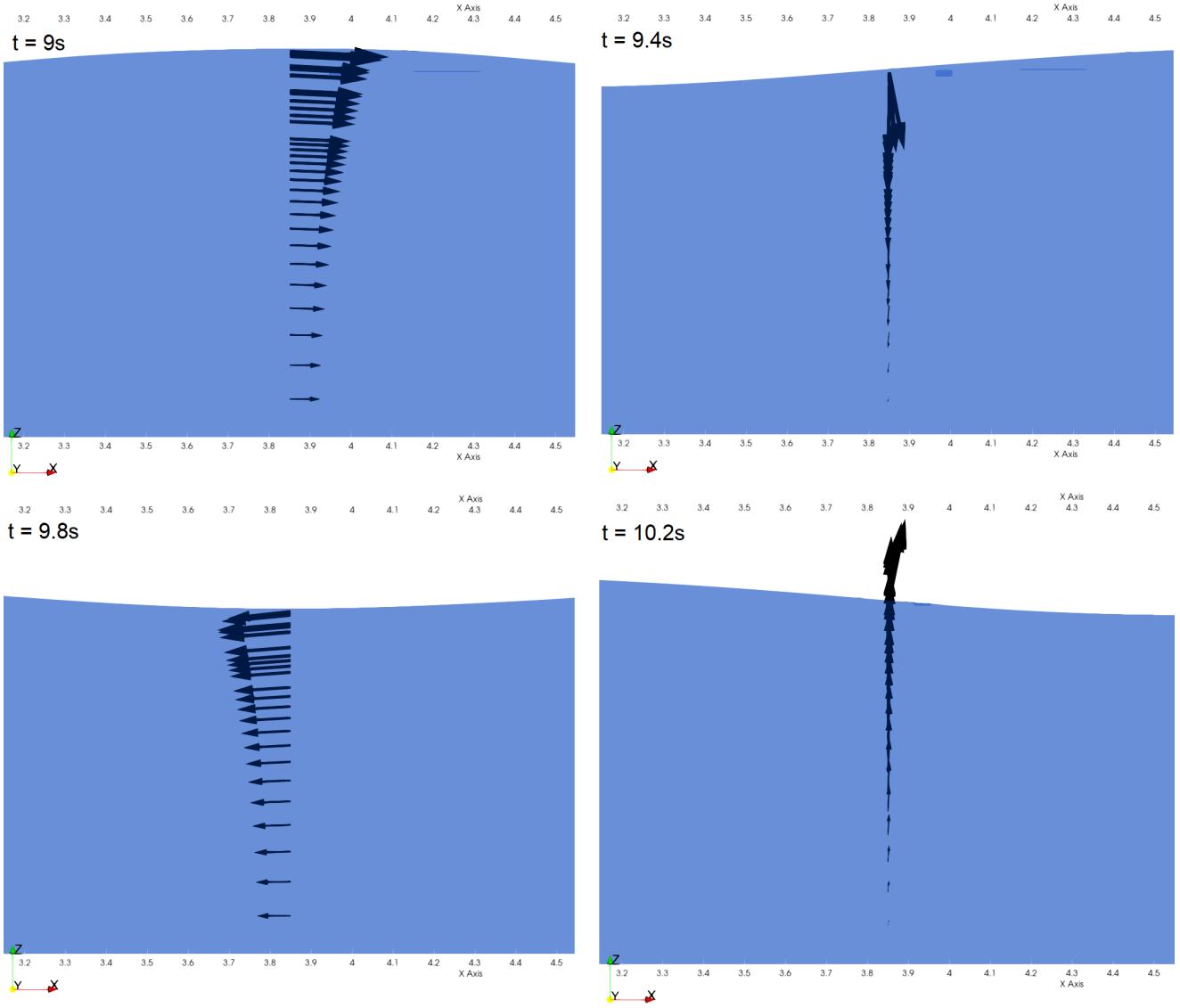

Figure 46: The velocity profile at a slice of the wave tank plotted at intervals of a quarter period ($T = 1.62s$).

First of all, the direction of the velocity for every quarter period is almost completely uniform. A small deviation is observed at the surface, where a small constant velocity in the propagation direction is observed. This is consistent with theory, as the waves propagating will carry small amount of mass transport over the surface in the propagation direction. This is a second-order drift motion observed in water waves, usually denoted as the mass-transport velocity [31]. Moreover, the vertical magnitude (at $t = 9.4s$, $t = 10.2s$) decreases exponentially with the depth. However, the horizontal magnitude seems to be inversely related to the depth, where the decrease in magnitude stagnates towards the bottom. This is indicative of an intermediate depth condition, where the orbital motion of the particles is elliptical because they "feel" the bottom. This implies that the generated waves have a wavelength λ that is significantly longer than twice the depth d, such that the deep water condition is not satisfied. The wavelength of the wave was calculated and measured to be approximately $3.7m$. The depth of the wave tank is $0.9m$. Therefore, the relative depth is approximately $\frac{d}{\lambda} = 0.24$, which is significantly less

than $\frac{1}{2}$ which is required for the deep water condition. Since the wavelength is consistent with linear wave theory, the wavelength must be of the same order in the experimental wave tank. Therefore, it is concluded that the waves as they are generated by the aforementioned wavemaker movement described by previous work do not satisfy the deep water condition.

6.7 Intermediate Conclusion

A 1:1 numerical model of the experimental wave tank was developed within olaFlow, a wave dynamics suite for OpenFOAM. The model was compared to linear wave theory and experimental results provided by previous work for identical wavemaker movement. The wavelength was measured to be $(3.71 \pm 0.02)m$ and is consistent with theory. Furthermore, the average wave amplitude was determined to be $0.0398m$, with a corresponding wave height of $0.796m$, a deviation of the reported empirical value of $0.08m$ by 0.05%. It was noted that it is not described how the empirical value was obtained or what the uncertainty of the measurement is. Additionally, the observed average wave amplitude differs from wavemaker theory which predicts the wave amplitude to be $0.05m$. Moreover, the wave amplitude has been shown to vary at different locations throughout the wave tank, developing a partial standing wave as a result of the reflection. The wave reflection coefficient was determined to be 0.529, where the energy in the reflected wave contains 28.0% of the energy of the incident wave. The partial standing wave is also represented in the FFT plot, as well as a lower frequency periodicity from which the origin cannot be fully defined. The velocity boundary conditions, the pressure and turbulence were confirmed to behave as expected. The beach was determined to not function optimally, since the wavelength is longer than twice the beach length. Finally, the particle motion was determined to be corresponding to intermediate depth conditions. This was determined to be consistent with theory, where the relative depth d/λ is 0.24, which is significantly less than 0.5. Therefore, the deep water condition is not satisfied for the waves generated by this wavemaker movement.

7 Results

In this section, multiple model configurations are presented and analyzed. First of all, as a consequence of not satisfying the deep water condition, a set of smaller scale waves is proposed. This way, a large part of the generated waves should satisfy the deep water condition, enabling the analysis of scaling effects and evaluation of the possible spectrum of waves in the wave tank. In the second part of the results, the addition of a foam layer at the end of the tank is investigated for enhanced reflection mitigation. Four cases are proposed to investigate the effect of the denseness of the foam, as well as the thickness.

7.1 Wave Spectrum

The spectrum of waves investigated are based on wave data from off the coast of Scotland [32]. The wave data contains the occurrence of waves, providing their significant wave height and peak period. These are properties of irregular waves, where the significant wave height is the average wave height of the highest one-third of the waves. The peak period is the period of the most energetic wave in a given wave spectrum at a given time. The irregular waves are approximated by regular waves according to the significant wave height and peak period. This is justified, because the aforementioned irregular wave properties describe the most energetic waves. Energetically higher waves are more interesting for the Ocean Grazer. This is supported by the fact that the energy in wave scales quadratically with its amplitude. The occurrence of waves are plotted in a scatter diagram in Figure 47, where the

wave height is plotted against the peak period. The color grading indicates the relative occurrence of specific waves averaged over a year. In the wave tank, only regular waves can be generated.

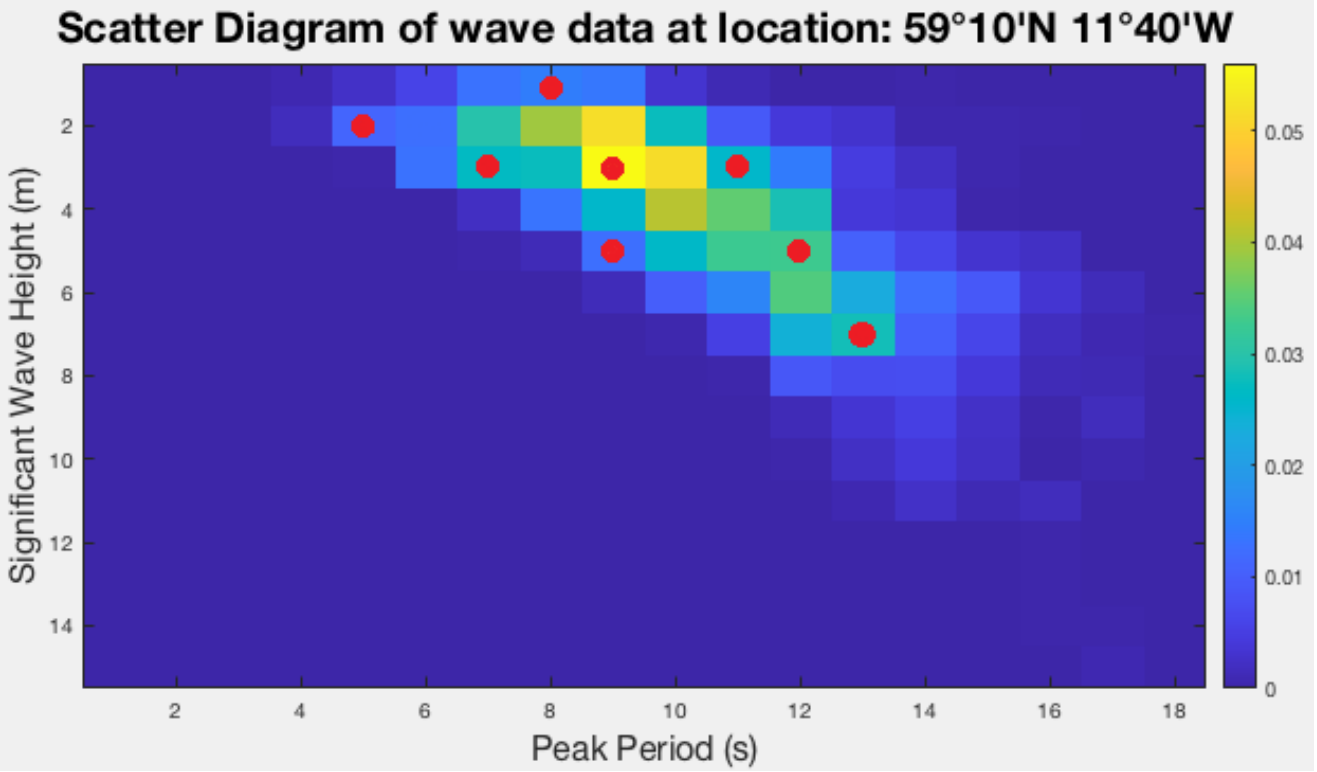

Figure 47: Selected waves from a scatter diagram of wave occurrence off the coast of Scotland averaged over a year [32].

From the "common" waves that are observed, 8 waves are selected to be simulated at a 1:70 scale in the numerical wave tank. According to linear wave theory, the deep water condition should now be satisfied for periods up to 9 seconds. It was decided to scale down to 1/70th, because it is twice as small as the original scaling, which should be sufficient to include the most common wave ($3m$, $9s$) in the deep water condition. Scaling even further, to satisfy the deep water condition for even longer periods, will have limited effect, since the Froude's scaling of the period scales with the square root of the scaling factor. Even for smaller scales, the larger common waves will not satisfy the deep water condition, whereas scaling effects will increase. For the selected waves, the wave properties will be investigated throughout the wave tank, to gain insight on the possible spectrum that can be created in the wave tank and the effects of going to a smaller scale. The selected waves are given in Table 16, along with their relative depth, which should be less than 0.5 to satisfy the deep water condition.

Case	Period	Wave height	d_{rel}
1	5	2	1.61
2	7	3	0.82
3	8	1	0.63
4	9	3	0.50
5	9	5	0.50
6	11	3	0.34
7	12	5	0.29
8	13	7	0.26

Table 7: The spectrum of waves that will be investigated in the numerical model, along with their relative depth in the wave tank.

The wave spectrum was generated in the same configuration as described in the model description. The absorbing foam layer is still excluded. Only the wavemaker movement was changed according to wavemaker theory to produce the desired waves. It must be noted that in this case, also the used mesh remains unchanged. This is a major concern, since we require at least 15 cells in the wave height, and 80 in the wavelength. The wave heights are now twice as small, and the periods are now $\sqrt{2}$ as small. The original full-scale wave was a $H = 2.8m$, $T = 9.584s$ wave on a 1:35 scale, using a mesh with 40 cells in the wave height and 88 in the wavelength. Therefore, similar waves such as the selected $H = 3m$, $T = 9s$ should have twice as many cells in the wave height and $\sqrt{2}$ more cells in the wavelength for a 1:70 scale. If the same mesh scaling is applied for the smallest wave properties, $H = 1m$ and $T = 5s$, the resulting mesh would equate to more than 10 million cells. Currently, 0.8 million cells are used. This would increase the computational time, power and space required beyond the scope of this project. The estimated computation time would be in the order of 2 weeks (14 days). Also, the mesh generation is a delicate process that requires special attention and it was not possible to perform this process multiple times for these simulations, especially on such a refined level. Therefore, the simulations were run on the same mesh as the initial case, with the effect of a sub optimal mesh becoming more apparent as the waves become smaller.
For every case, the Froude's scaled period T_{scaled} is given as well as the expected scaled wave amplitude A_{theory} by wavemaker theory and the observed average wave amplitude A_{avg}. Note that the selected spectrum was provided with significant wave heights, whereas the results will provide the wave amplitude, which is half the wave height. Furthermore, the amplitudes $A1$ and $A2$ are given, corresponding to the calculated values of the wave amplitudes of the incident wave and the reflected wave, respectively. They are calculated using the description of a partial standing wave, using the node and anti-node values. Based on A1 and A2, the reflection coefficient is calculated. The wavelength of the waves λ as well as the wavelength of the partial standing wave $\lambda_{standing}$ are given. Moreover, the average amplitude variation for every case is plotted, together with the maximum and minimum amplitude. Furthermore, the theoretical and average amplitude are also plotted. All cases are evaluated from time $t = 30s$ t0 $t = 50s$, where the reflection should have stabilized. Solely data from locations in the wave tank up to $6m$ are evaluated to minimize the influence of the beach on the calculated results. The observations are made and discussed in the following sections, however a summarized table of the results is shown in Table 8.

Case	$T_{scaled}(s)$	$A_{theory}(m)$	$A_{avg}(m)$	$A1(m)$	$A2(m)$	R	$\lambda(m)$	$\lambda_{standing}(m)$	d_{rel}
$13s$, $7m$	1.554	0.050	0.051	0.051	0.026	0.49	3.49	1.7±0.1	0.26
$12s$, $5m$	1.434	0.036	0.026	0.025	0.013	0.51	3.06	1.5±0.1	0.29
$11s$, $3m$	1.315	0.022	0.017	0.015	0.011	0.77	2.66	1.3±0.1	0.34
$9s$, $5m$	1.076	0.036	0.028	0.027	0.009	0.34	1.80	0.9±0.1	0.50
$9s$, $3m$	1.076	0.022	0.016	0.015	0.007	0.47	1.80	0.9±0.1	0.50
$8s$, $1m$	0.956	0.007	0.009	0.009	0.005	0.60	1.43	0.7±0.1	0.63
$7s$, $3m$	0.837	0.022	0.016	N/A	N/A	N/A	1.09	0.5±0.1	0.82
$5s, 2m$	0.598	0.015	0.0048	N/A	N/A	N/A	0.56	N/A	1.61

Table 8: Overview of the presented values for all cases.

7.1.1 Case 1: $T = 13s$, $H = 7m$

$T_{scaled}(s)$	$A_{theory}(m)$	$A_{avg}(m)$	$A1(m)$	$A2(m)$	R	$\lambda(m)$	$\lambda_{standing}(m)$
1.554	0.050	0.051	0.051	0.026	0.49	3.49	1.7±0.1

Table 9: Properties of the resulting scaled waves corresponding to a wave with $T = 13s$, $H = 7m$.

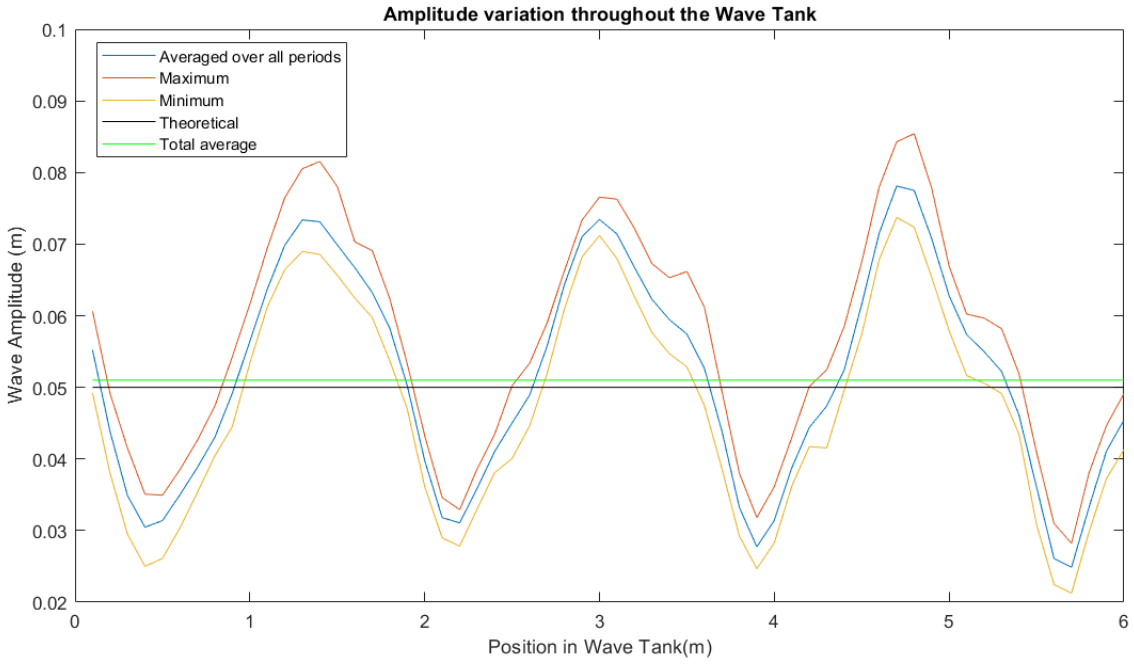

Figure 48: The wave amplitude variation throughout the wave tank of the resulting scaled waves corresponding to wave with $T = 13s$, $H = 7m$.

Starting with the largest wave of the selected spectrum, it can be seen that the amplitude A_{theory} as predicted by wavemaker theory and the average wave amplitude A_{avg} are consistent with each other, since the mesh height is $0.002m$ and the difference between them is $0.001m$. This is in contradiction with other results, as will be shown in the following subsections. Moreover, there appears a partial

standing wave similar to the one observed in the intermediate results. In addition, the wavelength of the partial standing wave $\lambda_{standing}$ is consistent to be half the wavelength of that of the waves λ. This was also observed in the intermediate results, as well as in the following results. The reflection coefficient was determined to be 0.49. Finally, it is observed that the shape of the partial standing wave is distorted. This is likely the result of the measurement discretization of $0.1m$ steps, as well as other reflection effects due to the crashing of the waves. Note that these waves are considered intermediate water waves, since the relative depth is only 0.26. This is also reflected in the particle motion shown in Figure 49, where the magnitude of the velocity components is not uniform in all directions, but stronger in the horizontal motions. This creates an orbital motion, rather than a circular motion. This is similar to what is observed in the intermediate results. Additionally, also similar to the intermediate case, a constant velocity in the wave propagation direction is observed at the surface.

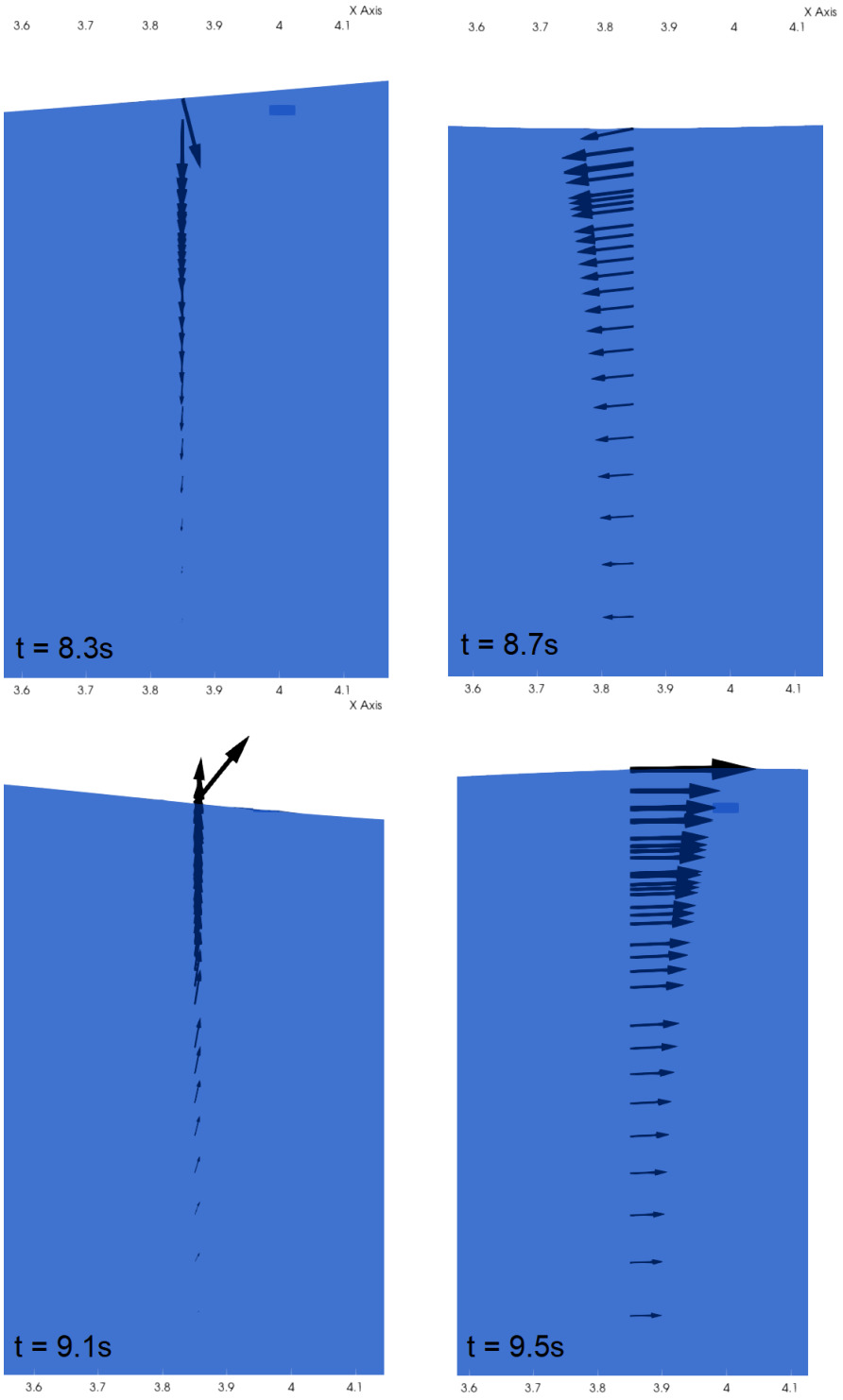

Figure 49: The velocity profile at a slice of the wave tank plotted at intervals of a quarter period ($T = 1.554s$).

7.1.2 Case 2: $T = 12s$, $H = 5m$

$T_{scaled}(s)$	$A_{theory}(m)$	$A_{avg}(m)$	$A1(m)$	$A2(m)$	R	$\lambda(m)$	$\lambda_{standing}(m)$
1.434	0.036	0.026	0.025	0.013	0.51	3.06	1.5±0.1

Table 10: Properties of the resulting scaled waves corresponding to a wave with $T = 12s$, $H = 5m$.

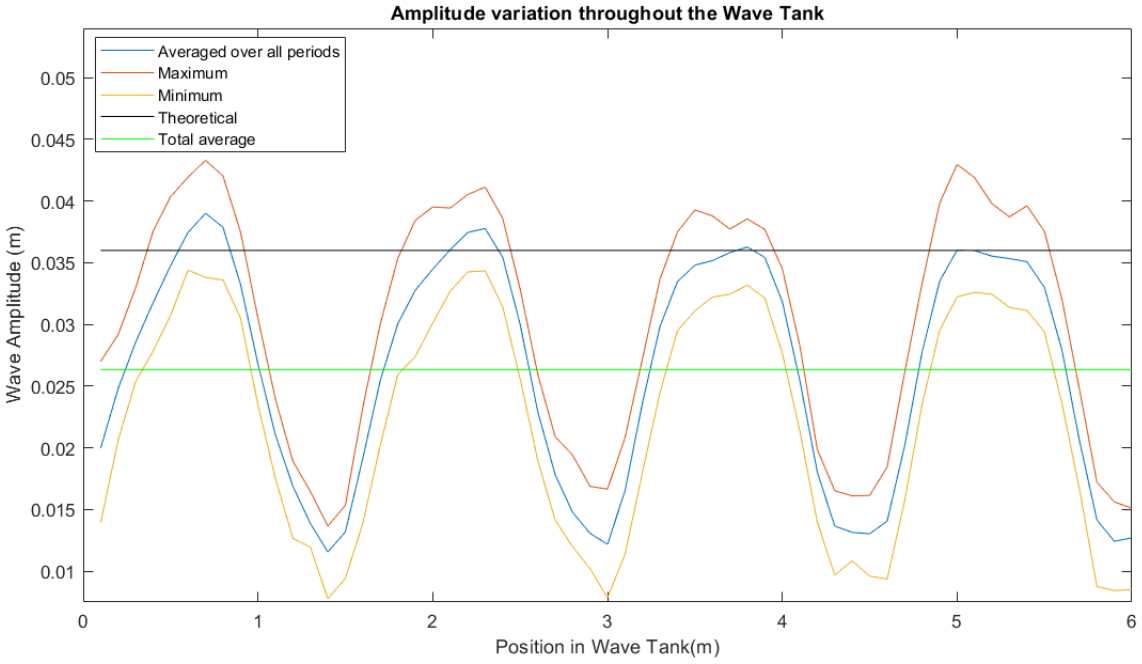

Figure 50: The wave amplitude variation throughout the wave tank of the resulting scaled waves corresponding to wave with $T = 12s$, $H = 5m$.

According to wavemaker theory, the expected wave amplitude is $0.036m$, which is the scaled wave amplitude of a wave with wave height $H = 5m$ at 1:70. However, the observed average wave height is $0.026m$, a difference of 18%. The overestimation of the wavemaker theory was also observed for the intermediate results, as well as for every following result, with the exception of the $8s, 1m$ waves. Again, the wavelength of the partial standing wave is half that of the waves. The reflection coefficient as a result of the partial standing wave was calculated to be 0.51.

7.1.3 Case 3: $T = 11s$, $H = 3m$

$T_{scaled}(s)$	$A_{theory}(m)$	$A_{avg}(m)$	$A1(m)$	$A2(m)$	R	$\lambda(m)$	$\lambda_{standing}(m)$
1.315	0.022	0.017	0.015	0.011	0.77	2.66	1.3±0.1

Table 11: Properties of the resulting scaled waves corresponding to a wave with $T = 11s$, $H = 3m$.

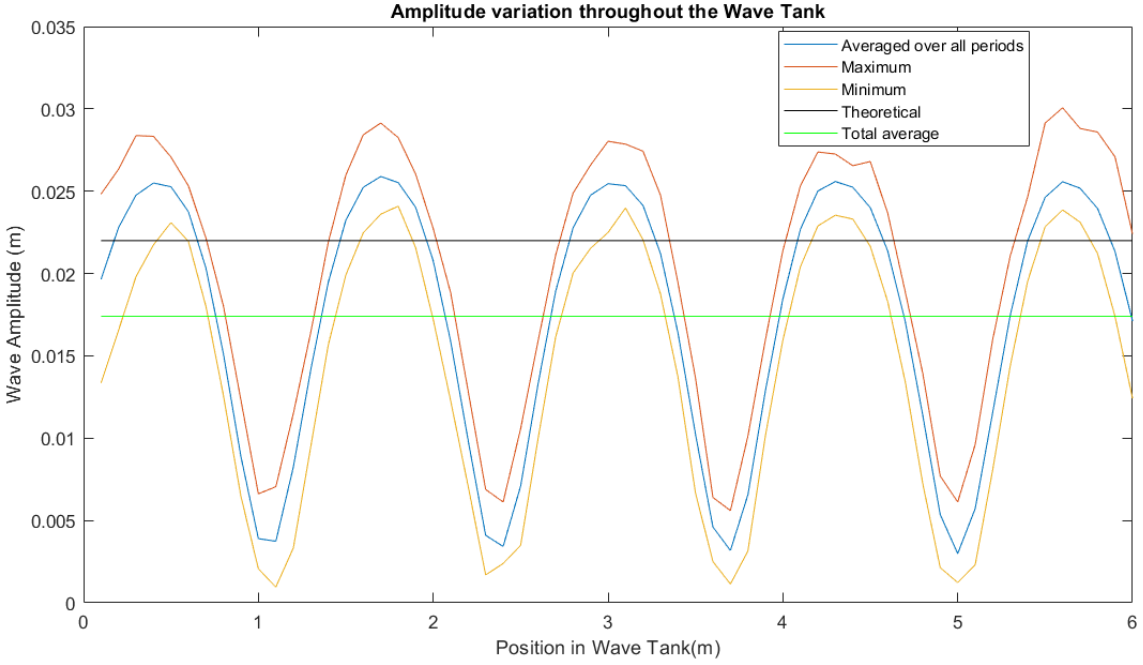

Figure 51: The wave amplitude variation throughout the wave tank of the resulting scaled waves corresponding to wave with $T = 11s$, $H = 3m$.

The difference between the observed average wave height for the $11s$, $3m$ waves is $0.05m$ or 23%. The wavelength of the partial standing wave is $1.3m$, which is again half the wavelength of the wave. For this case, however the partial standing wave is exceptionally well defined. Moreover, the reflection coefficient is notably higher than previous cases, with $R = 0.77$. It appears that the wavelength of the partial standing wave is commensurate with the length of tank. This causes the beach to behave more like a slope where the water is periodically pushed up and down, instead of crashing, as shown in Figure 52. This way, the water flows back and forth without the beach absorbing much energy. Therefore, the oscillation is unimpeded and an almost perfect standing wave is formed, as evident by the observed minima of the partial standing wave ($0.004m$). This would be zero for a perfect standing wave.

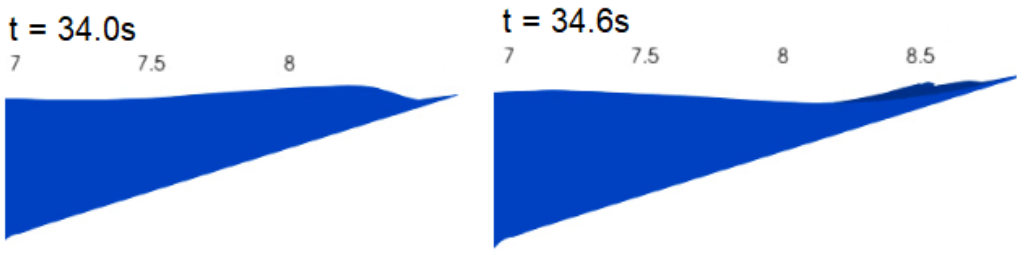

Figure 52: The waves periodically flowing up and down the slope without crashing.

7.1.4 Case 4: $T = 9s$, $H = 5m$

$T_{scaled}(s)$	$A_{theory}(m)$	$A_{avg}(m)$	$A1(m)$	$A2(m)$	R	$\lambda(m)$	$\lambda_{standing}(m)$
1.076	0.036	0.028	0.027	0.009	0.34	1.80	0.9±0.1

Table 12: Properties of the resulting scaled waves corresponding to a wave with $T = 9s$, $H = 5m$.

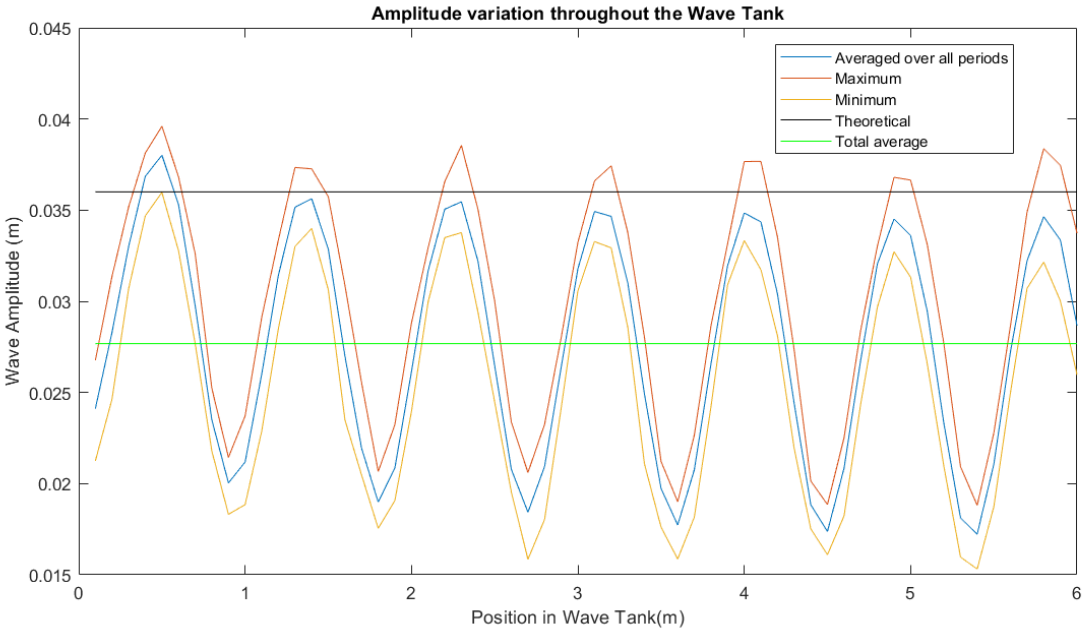

Figure 53: The wave amplitude variation throughout the wave tank of the resulting scaled waves corresponding to wave with $T = 9s$, $H = 5m$.

This case and the next are the first waves that are considered deep water waves, since their wavelengths are exactly twice the depth ($0.9m$). The particle motion plot validating that this is indeed deep water is performed for the next case, which has an identical period and wavelength. The aforementioned phenomena are again observed, with the average amplitude different from the theoretical value by 22%. The partial standing wave appears to be also well defined here, however the reflection coefficient is relatively small with $R = 0.34$.

7.1.5 Case 5: $T = 9s$, $H = 3m$

$T_{scaled}(s)$	$A_{theory}(m)$	$A_{avg}(m)$	$A1(m)$	$A2(m)$	R	$\lambda(m)$	$\lambda_{standing}(m)$
1.076	0.022	0.016	0.015	0.007	0.47	1.80	0.9±0.1

Table 13: Properties of the resulting scaled waves corresponding to wave with $T = 9s$, $H = 3m$.

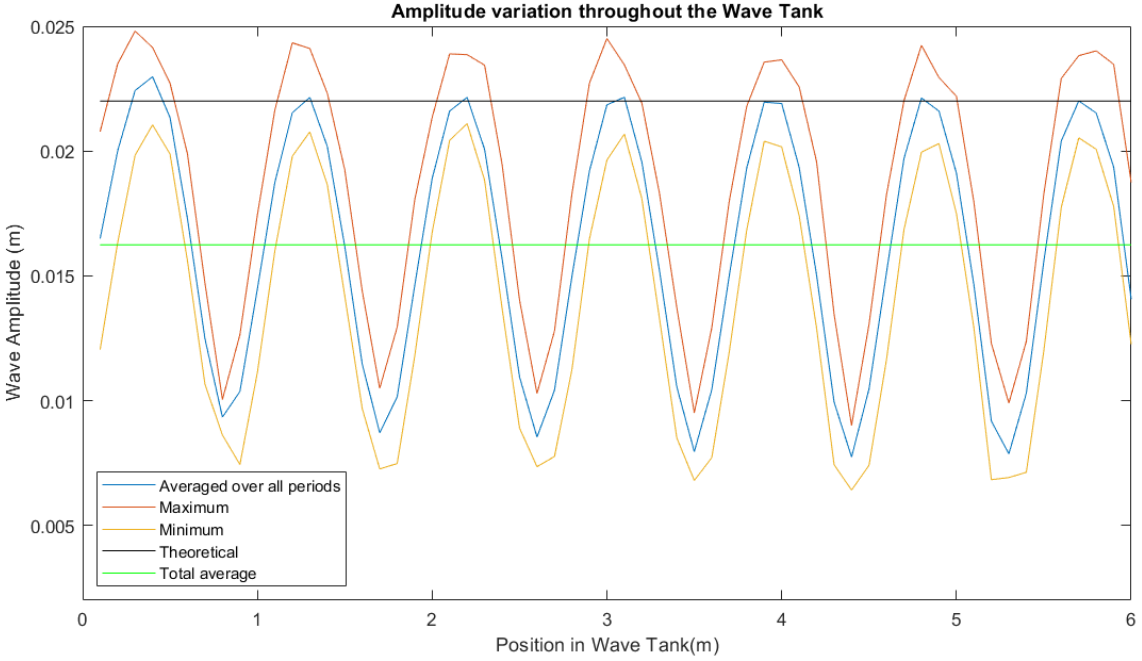

Figure 54: The wave amplitude variation throughout the wave tank of the resulting scaled waves corresponding to wave with $T = 9s$, $H = 3m$.

This case has the same period and wavelength as the previous case, however its amplitude is lower. The average amplitude in this case is 27% lower than the theoretical value. Its reflection coefficient $R = 0.47$, is significantly larger than for the previous case, even though only the wave height is different. Theoretically, the deep water condition is satisfied. The particle motion is plotted in Figure 55, where it can be seen that the particle velocity is uniform in all directions. The orbital motion of the particles is completely circular, and their radius decreases exponentially with depth, validating that the water is indeed behaving like deep water. This is true for all following cases, and is therefore omitted from their results. Another observation is that the surface layer still carries a small constant velocity in the wave propagation direction. In this case however, the magnitude is significantly smaller when compared to the $13s$, $7m$ wave.

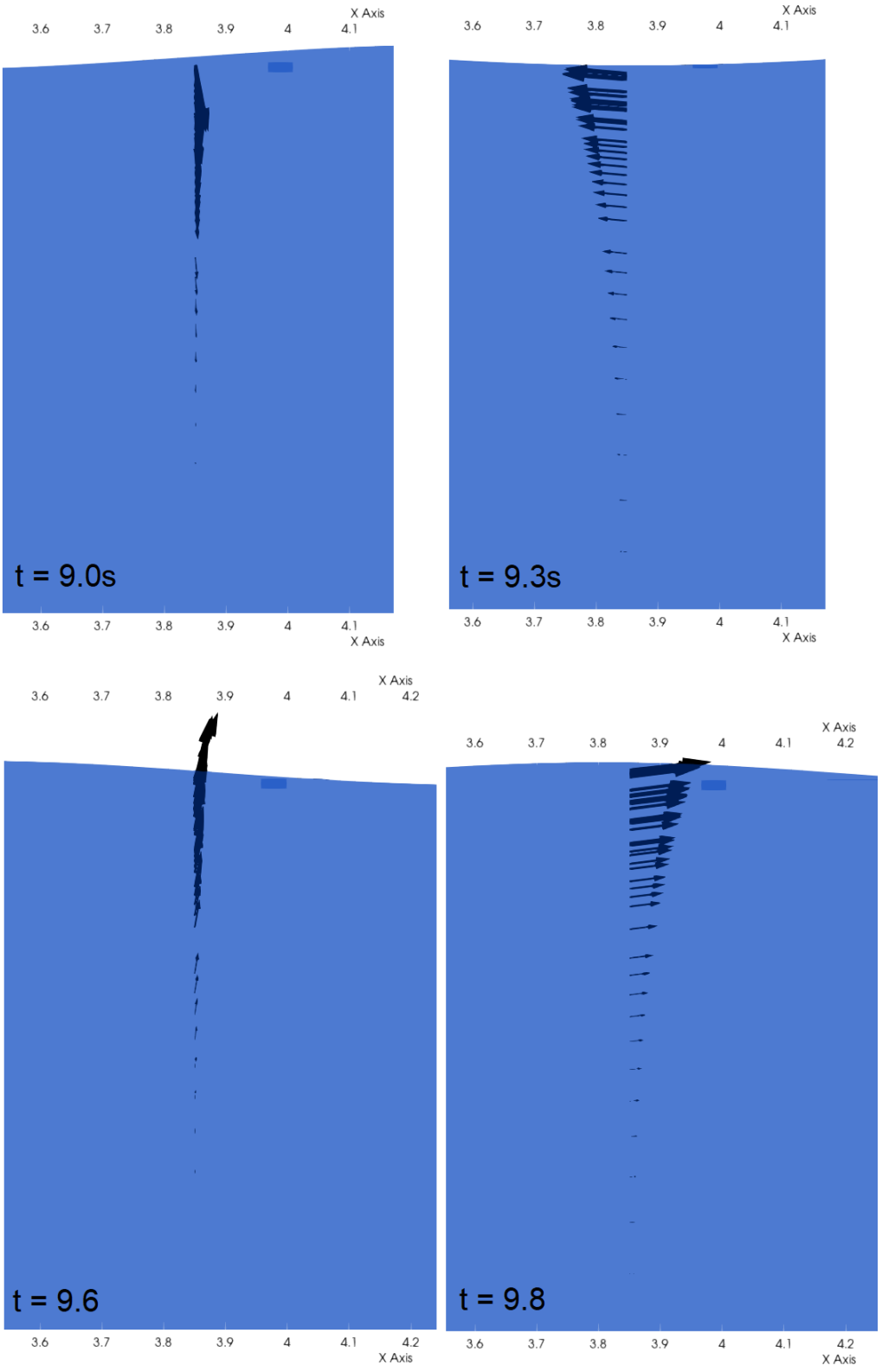

Figure 55: The velocity profile at a slice of the wave tank plotted at intervals of a quarter period (T=1.076s).

7.1.6 Case 6: $T = 8s$, $H = 1m$

$T_{scaled}(s)$	$A_{theory}(m)$	$A_{avg}(m)$	$A1(m)$	$A2(m)$	R	$\lambda(m)$	$\lambda_{standing}(m)$
0.956	0.007	0.009	0.009	0.005	0.60	1.43	0.7±0.1

Table 14: Properties of the resulting scaled waves corresponding to a wave with $T = 8s$, $H = 1m$.

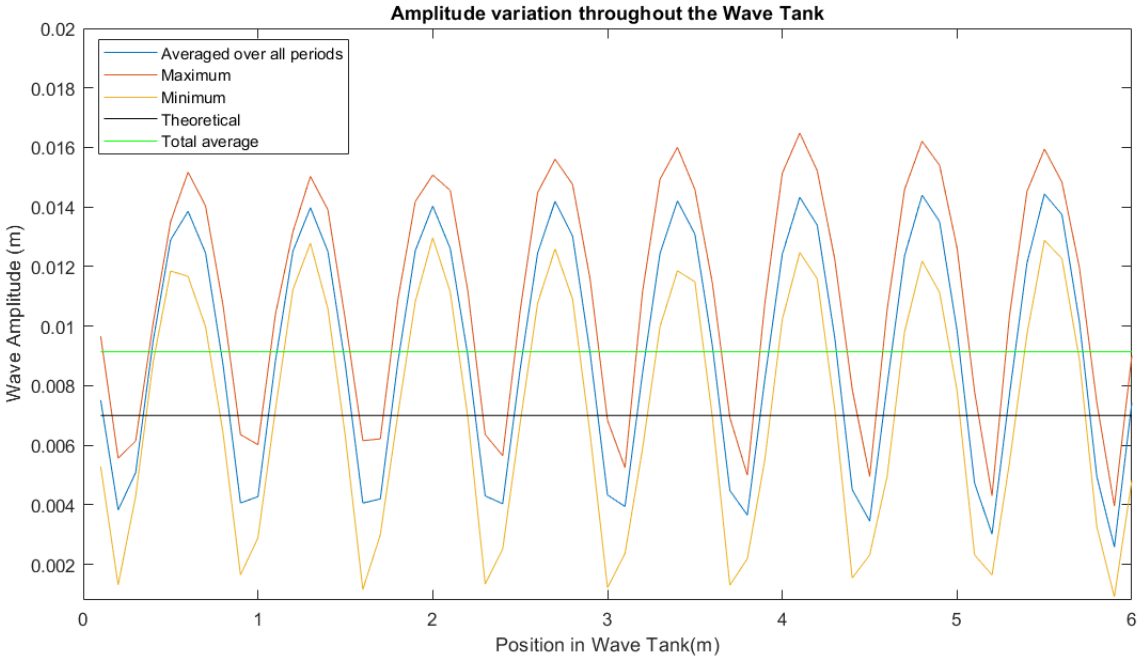

Figure 56: The wave amplitude variation throughout the wave tank of the resulting scaled waves corresponding to wave with $T = 8s$, $H = 1m$.

Contrary to other cases, the $8s, 1m$ wave's average wave amplitude is 29% larger than expected from theory. The reflection coefficient for this case was determined to be 0.60.

7.1.7 Case 7: $T = 7s$, $H = 3m$

$T_{scaled}(s)$	$A_{theory}(m)$	$A_{avg}(m)$	$A1(m)$	$A2(m)$	R	$\lambda(m)$	$\lambda_{standing}(m)$
0.837	0.022	0.016	N/A	N/A	N/A	1.09	0.5±0.1

Table 15: Properties of the resulting scaled waves corresponding to a wave with $T = 7s$, $H = 3m$.

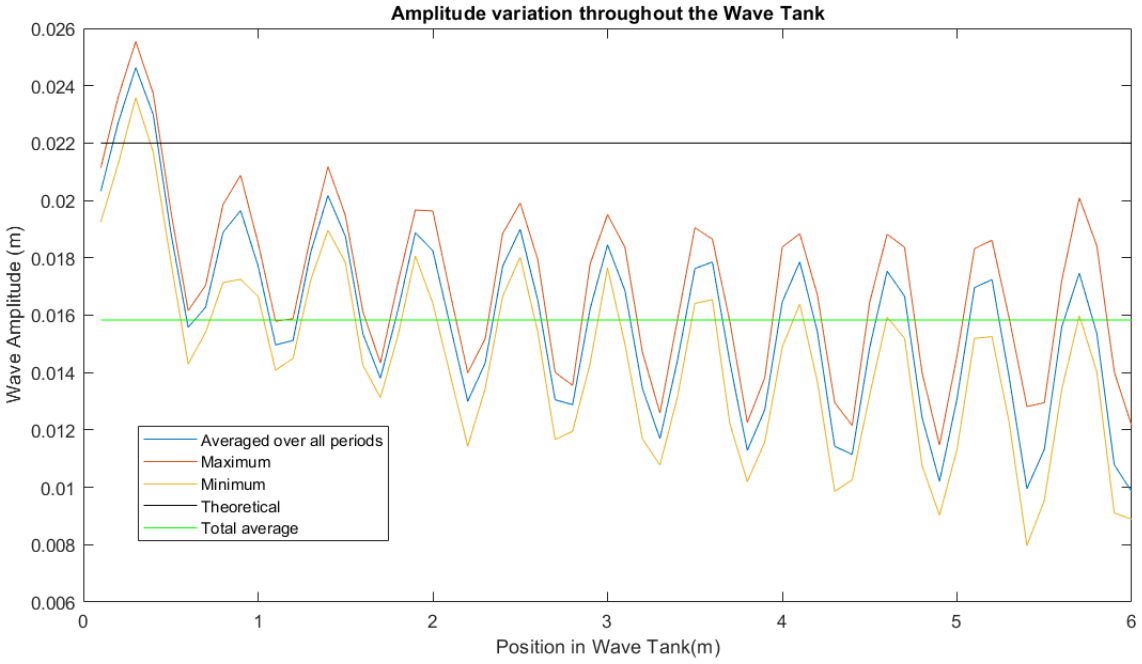

Figure 57: The wave amplitude variation throughout the wave tank of the resulting scaled waves corresponding to wave with $T = 7s$, $H = 3m$.

This case, and the following case both show a decrease in wave amplitude as a function of the position in the wave tank. The wave amplitude is the highest directly after the wavemaker and then decreases consistently. A partial standing wave is still observed, but due to the variation in wave height, it is not valid to extract data about the nodes and anti-nodes of the partial standing wave. Therefore, $A1$ and $A2$ cannot be defined, nor can the reflection coefficient. Once again, the average wave amplitude is lower than theory suggests, however in the beginning of the wave tank, the amplitude is much closer to the theoretical value than at the end of the tank.

7.1.8 Case 8: $T = 5s$, $H = 2m$

$T_{scaled}(s)$	$A_{theory}(m)$	$A_{avg}(m)$	$A1(m)$	$A2(m)$	R	$\lambda(m)$	$\lambda_{standing}(m)$
0.598	0.015	0.0048	N/A	N/A	N/A	0.56	N/A

Table 16: Properties of the resulting scaled waves corresponding to a wave with $T = 5s$, $H = 2m$.

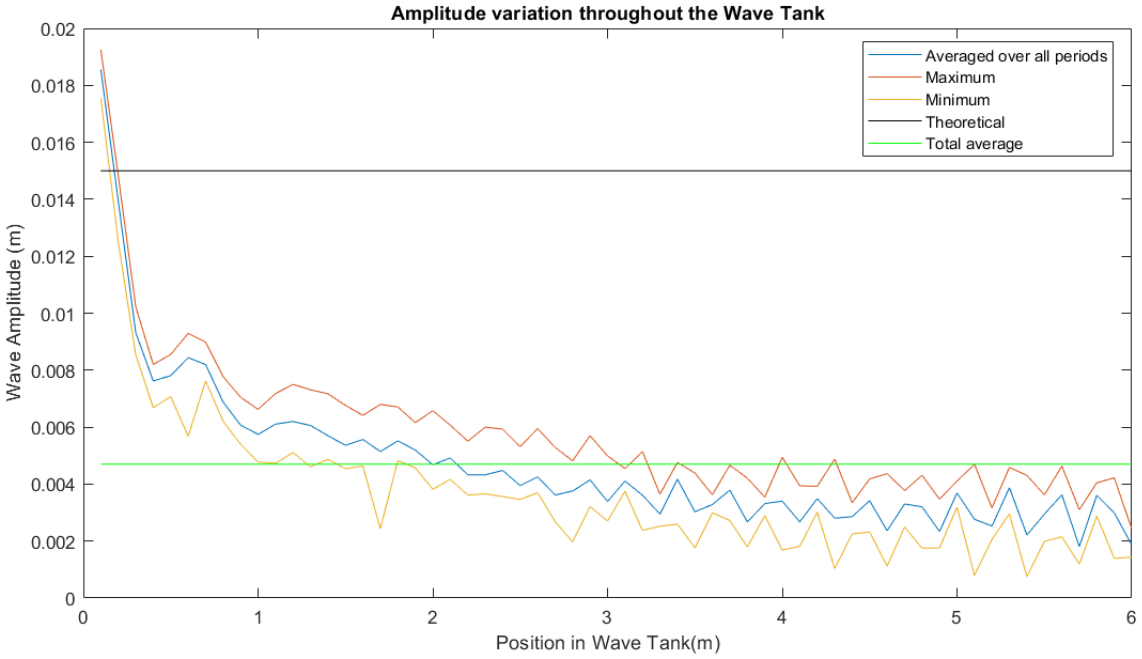

Figure 58: The wave amplitude variation throughout the wave tank of the resulting scaled waves corresponding to wave with $T = 5s$, $H = 2m$.

The last case, with the shortest waves, the decrease in wave height is even more severe. The wave amplitude decreases from the moment its generated till the end of the wave tank. At the end of the wave tank, a partial standing wave appears to be visible, but its periodicity or wavelength are not determinable.

7.2 Reflection Mitigation

In order to investigate the effect of reflection mitigation due to the foam layer that is present in the wave tank, four cases are set up. The foam layer's properties are unknown, therefore it was not possible to recreate the foam directly. Therefore, this study aims to investigate the effect of the thickness and denseness on the absorption. The thickness is defined as the height of the foam layer. The denseness is defined as the combination of porosity ϕ and mean nominal diameter D_{50}, the two parameters used in olaFlow to model a porous medium. The denseness is high for low porosity and small diameters. All four cases are run with the same model configuration, identical to the one described in the model description. This allows for a direct comparison to the intermediate results and should yield the best results, since the model and the mesh in particular, were optimized using this configuration. First of all, a base case is presented, in which default porosity model settings were applied. Consequently, two alterations are presented with varying denseness of the foam layer. One alteration will feature a thinner layer, with the porosity and nominal diameter increased with 50% so more water is allowed to flow through the material more easily. The denser case has both parameters decreased by 50%. For the final case, the base denseness is applied for a foam layer with a thickness of three times the original thickness. All configurations are then also compared to the initial model without foam layer, denoted "No Foam". The set of foam layer configurations is shown in Table 17.

Case	ϕ	$D_{50}(m)$	Thickness(m)
No Foam	N/A	N/A	N/A
Base	0.490	0.01590	0.07
Thinner	0.735	0.02390	0.07
Denser	0.245	0.00795	0.07
Thicker	0.490	0.01590	0.21

Table 17: The set of foam layer configurations.

In Table 18, the average amplitude A_{avg} throughout the wave tank is given, as well as $A1$, $A2$ and the reflection coefficient R as calculated from the observed partial standing wave for every case.

Case	$A_{avg}(m)$	$A1(m)$	$A2(m)$	R
No Foam	0.0398	0.0397	0.0210	0.529
Base	0.0517	0.0512	0.0117	0.228
Thinner	0.0503	0.0496	0.0128	0.257
Denser	0.0535	0.0534	0.0096	0.180
Thicker	0.0475	0.0474	0.0097	0.204

Table 18: The resulting average wave amplitude, calculated incident and reflected wave amplitudes and reflection coefficient of the investigated cases.

First of all, it appears that the foam layer absorbs a significant part of the energy of the wave that is otherwise reflected. The reflection coefficient as apparent from the partial standing wave is drastically reduced, when compared to the intermediate "No Foam" case. From the limited amount of cases presented, it can be seen that the densest foam layer reduces the reflection the best. The thinnest layer performs worst. For the case where the thickness was tripled, denoted "Thicker", the reflection is lower than for the base case, however the denser case performs better. Furthermore, we see that both the average amplitude A_{avg} and the determined incident wave amplitude $A1$ increase with better

wave absorption. This is also true for the thicker case, however not to the same extent as the other cases. Furthermore, it can be seen that with the inclusion of the foam layer, the average amplitude and the determined incident wave height $A1$ are now closer to, and sometimes higher than the wave amplitude of $0.05m$ as predicted by wavemaker theory.
For all cases, the wave amplitude variation is plotted in Figure 59. Note that the range on the $y-$axis is adapted per case. The first thing to observe is that the inclusion of a foam layer induces a phase shift of the partial standing wave towards the wavemaker. The phase shift appears to be larger for a denser foam layer. Remarkably, for the thicker case, a phase shift of half a wavelength is observed. The anti-nodes are now located where the nodes are in the other cases. Additionally, it can be seen that the inclusion of a foam layer decreases the spread of amplitudes at each location, shown in the convergence of the minima and maxima towards the average value. It is notable that even though the reflection coefficient was higher for the thicker case, its maximum wave heights are still lower than for the denser case. Finally, it is observed that the partial standing wave for the "Denser" case appears to be distorted.

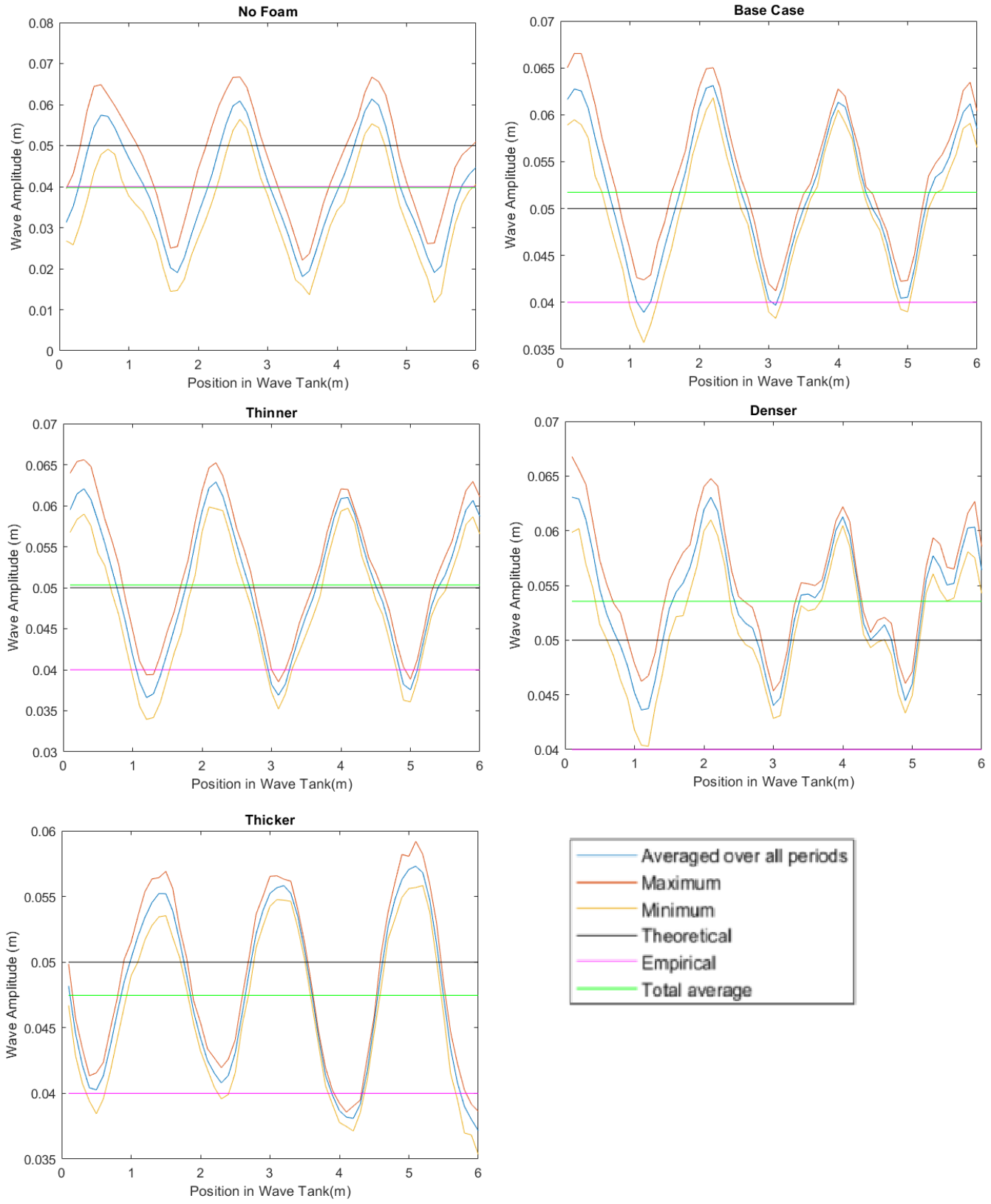

Figure 59: The wave amplitude variation plotted as a function of position in the wave tank for all cases presented.

8 Discussion

8.1 Wave Spectrum

In the first part of the results, a spectrum of 1:70 scaled waves are presented based on real wave data in order to investigate which relevant waves can be produced in the wave tank. The average amplitude, amplitude variation and reflection are investigated.

8.1.1 Limitations of the Mesh

First of all, it should be reiterated that the original mesh was used for all simulations. Based on the required amount of cells for wave dynamics simulations, only the results for waves higher than $2m$ and longer than $11s$ are accurate. Even so, these results are not able to be validated. It is observed that for the two shortest waves, ($7s$, $3m$ and $5s, 2m$), the average wave amplitude decreases over the length of the wave tank. This could indicate that these waves are too short, and the waves simply dissipate their energy as the wave progresses. This is also expected due to shear stresses in the fluid due to viscosity, however not in the order of magnitude as it is observed in these two cases. This dramatic decrease in wave amplitude is not visible in the other cases. It is reasonable to propose that the decrease in amplitude is caused by a coarse mesh. The cell length is $0.042m$ in the wave propagation direction. Therefore, only 26 and 13 cells are present in one wavelength of these cases, respectively. The solution is averaged over a large volume, thus losing some of the information otherwise contained in a finer mesh. This is known as numerical diffusion [33], in this case amplifying the dissipation of wave energy over distance. Even though this effect is exaggerated in the last two cases, it is not ruled out this is true for other cases too. Based on this observation the last two cases are not included with any conclusive arguments.

8.1.2 Performance

It was observed that the selected spectrum of waves was able to be generated at a 1:70 scale, excluding the smallest two cases. The waves perform well, however due to the invalidation of the smallest waves, no conclusions can be made on the performance of the last two cases. The generation of smaller waves is an important step for future validation and testing experiments, because the deep water condition is important in the simulation of ocean environments. At this scale, the deep water condition is only satisfied for periods up to and including $9s$. Therefore in order to include the largest waves in the deep water condition, the scale should become even smaller. In the future, the generation of a case specific mesh for the smaller cases could be beneficial to gain insight into the performance of smaller waves at this scale. In order to validate the observations made in this thesis, the waves should be recreated experimentally in the wave tank. Due to the aforementioned arguments on the mesh, no conclusions can be made on the scaling effects.

8.1.3 Reflection

It was found that a partial standing wave is formed as a consequence of the reflection for every case. The wavelength of the partial standing wave is consistently half that of the propagating wave, for all cases. The reflection coefficient between cases, as calculated from the partial standing wave amplitudes, ranges from 0.34 to 0.77. If we compare the $5m$ waves, we see that the shorter waves ($9s$) have a significantly lower reflection coefficient than the longer waves ($12s$), being 0.34 and 0.51, respectively. This is also observed for the $3m$ waves, where the shorter ($9s$) waves' reflection coefficient (0.47) is

lower than the longer ($11s$) waves' reflection coefficient (0.77). This is expected, since for wavelengths longer than $2.61m$, the beach is not sufficiently long to perform optimally. Therefore, the reflection is expected to be higher for waves with periods of $11s$ or longer. Based on the $9s$ period waves, it appears that smaller waves also tend to have a higher reflection coefficient, however from theory it is expected that the reflection should be equal, since it is only dependent on the wavelength.
The incident wave amplitude $A1$ was observed to be consistent with the average wave amplitude for all cases. This implies that the vast majority of the reflection is captured in the partial standing wave. Other reflections due to the crashing at the beach generating higher frequency waves are therefore likely to be negligible at this scale of simulations.

The highest reflection coefficient was found for the $11s$, $3m$ wave. It was suggested that the wavelength of the partial standing wave is commensurate with the length of the wave tank, oscillating at a resonance frequency. This is supported by the fact that the waves do not crash at the beach, but merely flow up and down. In order to confirm this theory, a study could be proposed where multiple $11s$ cases at 1:70 scale are performed with varying wave heights.

8.1.4 Wave Amplitude

It was observed that for all cases, with the exception of the $13s$, $7m$ and $8s$, $1m$ waves, the observed average amplitude is lower than expected by wavemaker theory by (18-27)%. This was also shown in the intermediate results, where the observed average amplitude was 20.0% lower. This is probably due to the influence of the reflection. Waves reflecting off the beach interfere with the propagating waves and suppress the waves. This hypothesis will be supported in the second part of the results.

The observation that the $13s$, $7m$ waves' average amplitude agree with theory, whereas others do not, is notable, because this case has arguably the best mesh, relatively. It is expected that the value for the average amplitude is lower than the theoretical value due to the reflection as observed in other cases. The value for the average amplitude A_{avg} is an outlier, since other observations are in line with what is seen in other cases.
Another outlier is the average amplitude for the $8s$, $1m$ wave, which is significantly higher than the theoretical value. This is most likely due to a coarse mesh. The cell height is $0.002m$, which is exactly the difference between the theoretical value ($0.007m$) and the observed value ($0.009m$). Only 8 to 10 cells are present in the wave height, as opposed to the required 15. Therefore, the average wave amplitude is probably overestimated as a consequence of the mesh.
Finally, it should be noted that these two outliers are the only cases where the partial standing wave starts with a node, whereas all other cases initiate with an anti-node. This will be elaborated on in Section 8.2 of the discussion.

8.2 Reflection Mitigation

In the second part of the results, the reflection mitigation of a foam layer is investigated. A total of five cases are analyzed, where the influence of denseness and thickness are observed based on the observed average amplitude, partial standing wave and the reflection.

8.2.1 Performance

First of all, the hypothesis that a foam layer decreases the reflection in the wave tank was supported, since every implementation of the foam layer yielded a lower reflection coefficient than the "No Foam" case. The observed reflections range from 0.257 to 0.180, where only 6.6% to 3.2% of the wave energy is present in the reflected wave, respectively. Furthermore, a trend was observed, where denser foam layers decrease the reflection the most. It is hypothesized this trend does not continue for increasingly dense foam layers, but that an optimal denseness exists. Foam layers that are denser than the optimal denseness will act progressively more like solid objects. Instead of slowing down the fluid flow, the flow will start to reflect off the foam. Future research could propose a study on the effect of increasingly dense foam layers to test this hypothesis.
Furthermore, it was found that a foam layer with triple the thickness performs better than the base case. A thicker layer means that more of the wave is absorbed initially, therefore less or no crashing of the wave can occur. This slows down the fluid flow even before reaching the solid beach. Additionally, the flow is also slowed down when flowing back. For optimal reflection mitigation, a future study could be performed on the effect of using a combination of a thicker and denser layer.

8.2.2 Partial Standing Wave

The partial standing wave is a result of reflection at the beach, and is dramatically reduced with the implementation of the foam layers. Furthermore, for the cases where the denseness is varied, a phase shift towards the wavemaker is observed. This could imply that the foam makes the effective length of the wave tank shorter, therefore shifting the resulting standing wave. This effect is stronger for denser foams, and weaker for thinner foams. For the thicker case, the phase shift is half a wavelength, switching the position of nodes and anti-nodes. In theory, this is possible for any case, since a standing wave typically has a preferred orientation in a fixed domain, and this orientation is the same for every phase shift of half a wavelength. Therefore, both orientations are equally likely. It is notable however, that this only occurs for the case where the thickness is altered. A study could be conducted to run the same simulations multiple times to observe whether this is consistently the case.
Additionally, it can be observed that when the denseness is sufficiently high, other distortions in the wave amplitude become apparent. This is the case for the "Denser" case, where the amplitude variation does not show a perfect partial standing wave anymore. The partial standing wave is distorted, and higher frequency effects become visible, especially towards the end of the wave tank. This indicates that the partial standing wave is not the only result of reflection in the wave tank. It could be the case that these reflections are either not adequately absorbed by the foam layer and beach, or that the foam layer denseness introduces new types of reflections.

8.2.3 Wave Amplitude

It was observed that the average wave amplitude and the determined incident wave amplitude $A1$ increases with better reflection mitigation for the cases where the denseness was altered. This supports the hypothesis that the waves are suppressed by the reflection. This is contradictory with partial standing wave theory. In theory, based on the nodes and anti-nodes, the wave amplitude of the original incident wave $A1$ can be calculated. This wave amplitude should be representative of the initial incident wave that is created, which is independent of the amount of reflection, only amplitude $A2$ should change and be dependent on the reflection. This is not what is observed. A strong dependence on the the reflection is observed. Therefore, it is concluded that the partial standing wave not only amplifies and destructs the wave height at certain locations, but also decreases the overall average wave amplitude throughout the tank. To validate this phenomenon, an experimental study should be

conducted to observe if the average amplitude does indeed decrease with high reflection.
For these cases, where the denseness was altered, it is notable that the densest cases' average amplitude exceed the theoretical value as predicted by wavemaker theory ($0.005m$). For the case where minimal reflection was observed, the average wave amplitude was $0.0035m$ or 0.07% higher than expected by theory. Based on the observed trend, it appears that for a case without any reflection, the wave amplitude will be significantly greater than the theoretical value. It should be noted that for these cases, the wavemaker movement was identical to the intermediate results. This movement is asymmetrical, and wavemaker theory assumes a symmetrical movement. This could explain the difference between theory and the model, however experimental validation should be performed to investigate the difference from wavemaker theory. This result does indicate that wavemaker theory is helpful in estimating what movement is required to generate a desired set of waves.

For the case where the layer was made thicker, the average amplitude is lower than the base case, however the reflection coefficient is also lower. This against the trend that was observed for the denser foams, where the wave amplitude increases with better reflection mitigation. It is probable that the change in average wave amplitude is due to the phase shift of the partial standing wave. This is supported if we take the first part of the results into account. In the first part of the results, the average amplitude is lower than the theoretical value for all cases, with two outliers. If we compare the phases of the partial standing waves, it can be seen that the phases of the two outliers start with a node, whereas the trend is observed for cases where the phase initiates with an anti-node. Therefore, it appears that the observed amplitude is dependent on the phase of the resulting partial wave. This is true for both the average amplitude as well as the amplitude $A1$, as calculated from the partial wave. For future studies, it should be investigated whether this is also observed experimentally.

8.3 Model Discussion

In this section of the discussion, the validity of the assumptions and limitations of model are discussed. Starting with the domain; the space before the wavemaker is neglected and the wavemaker is defined as a moving wall. In the physical wave tank, it is observed that for relatively large wavemaker movements, a significant flow develops along the sides of the wavemaker. This flow could induce small, non uniform oscillations at the surface of water. Also, due to the hinge in the experimental wave tank, the wavemaker's origin is not exactly at the bottom of the wave tank, but slightly above it. Moreover, water is allowed to flow underneath the wavemaker. These effects should only be minor and generally have no effect on the general behaviour of the waves.
For the wall conditions, no-slip conditions are applied, as a result a velocity boundary is formed. However, in the experimental wave tank along the length on one side, two acrylic glass panels are present. In reality, the boundary layer formed by these panels should be slightly different than for the regular walls. This could cause an asymmetric propagation along the width of the tank. This effect should be negligible however, since the boundary layers are very small and the walls and glass panels both are smooth surfaces.

An important influence of the quality of the results is the mesh. The mesh was made based on literature recommendations and has shown results that were able to be validated. The mesh was developed in several stages, up to a point where the solution was not mesh dependent anymore. Therefore, the trends observed in this thesis should also not be mesh dependent. However, for the smaller waves, a case specific mesh was required, as evident from the smallest cases where it is clear that the mesh does not suffice. Therefore, the absolute values provided for these cases are not representative. However, the trends observed are still valid and consistent with other observations.

Furthermore, it should be noted that a turbulence model is an approximation of what theoretically could happen. For this simulation, an k-ω SST model was used. This model was developed based on empirical observations, typically for cases where the flow is the main concern. In this case, the turbulence model was applied to approximate the crashing behaviour of the waves. Crashing of waves is such a chaotic process that it is impossible to model accurately. If there is a large deviation from what happens in the physical wave tank, the reflection could be dramatically different, especially for higher frequency effects. However, the general back flow, or direct reflection that forms the partial standing wave should show similar behaviours as to what is observed in the numerical model.

It should also be noted that the foam layers are approximated by the volume averaging method. In this way, the back flow through the foam layers is approximated by a general flow velocity rather than modelling the fluid flowing through the separate cavities. This could be a large deviation from reality or a valid approximation, depending on the micro structure of the foam. Moreover, the porosity model requires a few model parameters (α, β, C), which should ideally be obtained empirically for an accurate model. Finally, the porosity and nominal diameter of the used material should be investigated in order to accurately recreate the physical wave tank in a numerical model.

8.4 Post-Processing

A few general remarks on the data presented should be made. It should be reiterated that the data was extracted from the water surface at $0m - 6m$ from the wavemaker. It should be noted however, that waves develop after generation, and that the wave is not completely representative at small distances from the wavemaker. Also, the waves start to "feel" the beach quite early on in the wave tank already, especially for long wavelengths. This could lead to a shifted value for the observed average amplitudes.

Moreover, the data acquisition method should be discussed. First of all, the solutions of the numerical model were saved every $0.1s$. Therefore, effects at smaller timescales will not be observed in post-processing. The data was post-processed in Paraview, from which the surface elevation data was extracted. This was done at distance intervals of $0.1m$. Together with the time interval, this means that very high frequency effects with small wavelengths are not adequately represented in the post-processing. This is also a limitation of the aforementioned calculated values, and the cause of some distortions in the plots. All calculations were performed on this extracted data, therefore a significant uncertainty is still present. The calculations on the data were performed in MATLAB, for which the scripts are provided in Appendix B and C.

8.5 Implications and Recommendations

First of all, the intermediate results show an average wave amplitude of $0.0398m$, which is consistent with the observed empirical value of $0.004m$, as reported in previous work. Note that in the empirical experiment, a foam layer was present, whereas in the intermediate results there was not. Based on this observation, it could be hypothesized that the foam layer is really thin and absorb an almost negligible amount of the wave. Furthermore, it was concluded that a partial standing wave is developed in all of the cases. Partial standing waves alter the wave motion. The propagation of the wave is still present, however its amplitude is dependent on the location in the wave due to the reflected wave. If a perfect standing wave is developed, the net velocity of the wave is zero and no propagation occurs anymore. Moreover, the average wave amplitude was shown to decrease with increased reflection. This shows suppression of the waves as a result of the reflection. These conditions are vastly different from ocean

waves and should therefore be avoided for future validation and experiments.

It was shown that the reflection is very dependent on the type of wave. The reflection seems to increase with wavelength, with longer waves having higher reflection coefficients. In order to mitigate the increased reflection for longer waves, the beach should be made longer, such that the beach is at least half the wavelength of the longest desired wave. This should be done by reducing the inclination of the beach, such that a larger part of the beach is submerged.

In order to consistently satisfy the deep water condition, two options are available. One option is to reduce experiment scale even further. This is not recommended, because surface tension and viscous effects will have an increasing effect. Apart from those effects, additional scaling effects not mentioned in this thesis will have an increased effect such as mechanical friction. A better option is to allow for a deeper water depth d in the wave tank. Ideally, the depth d is sufficiently larger than half the wavelength of the largest desired scaled wave. Therefore, it is recommended to have a deeper wave tank in order to guarantee the deep water condition to validate experimental results.

Moreover, the addition of foam layers has shown to improve reflection mitigation, where denser layers appear to perform better. Therefore it is recommended to use a more dense foam layer than what is used currently. It was hypothesized that there is an optimal denseness for the foam. The best results in this thesis were obtained for a porosity of 0.0245, and a mean nominal diameter of $0.00795m$, reducing the reflected wave energy down to 3.24%. This value was obtained without any optimisation and suggests that better absorption values could be reached. Additionally, stacking of the layers should be considered. It was shown that a thicker foam layer shows amplified wave absorption. Possibly, a block of foam could be considered at the beach, with a denseness gradient. Towards the bottom of the beach, the denseness would be largest, and at the top it should be thinnest. This way the water should be slowed down gradually as it approaches the beach. As noted before, this thesis only investigated reflection in the form of a partial standing wave, as it is the most dominant and apparent type of reflection. If this phenomenon is sufficiently suppressed, other reflection effects may become dominant and influence the waves differently.

Another approach to avoid reflection is to have a sufficiently long wave tank, such that a few waves can be generated which can then propagate over a long distance, before hitting the beach. This avoids the waves reflecting back after a short while, whilst allowing the waves to develop without influence of the wavemaker or beach. This requires a wave tank with a length of several wavelengths of the longest desired wave. Note that longer waves also travel with a higher celerity than short waves.
Finally, it is recommended to generate a symmetrical wavemaker movement. This way, wavemaker theory can be properly validated and applied. This should provide more control over the generated waves and therefore more insight into experimental results.

9 Conclusion

In order to validate and optimize the novel technologies behind the Ocean Grazer, scaled-down experiments are required. For WEC systems in particular, the foundation of these experiments is the physical modelling of ocean waves in a wave tank. The goal of this thesis was to investigate whether the Ocean Grazer experimental wave tank can create adequate environments for future validation and testing experiments. The research was performed by developing a full-scale numerical model of the wave tank in OpenFOAM, using the olaFlow suite.

9.1 Validation and Intermediate Results

First of all, the model was created and configured by means of empirical data as described in previous theses on the wave tank. The foam layer was still excluded from this model. The results of the preliminary model were then validated using linear wave theory, wavemaker theory and empirical data.
The wavelength, pressure, turbulence and velocity were validated based on theory. It was concluded that the observed average amplitude was consistent with the empirical data. However, both values were significantly lower than expected from wavemaker theory. A partial standing wave was shown to develop as a result of the reflection. This was also confirmed by the observation of a second harmonic in the FFT plot, where the partial standing wave's frequency is twice the generated wave's frequency. The wavelength of the partial standing wave was found to be half of the wave's wavelength. Based on the observed partial standing wave, a reflection coefficient was defined to quantify the reflection. The reflection was presumably amplified by the fact that the beach was not performing optimally due to the length of the waves. Finally, based on the relative depth and the particle motion, it was concluded that the deep water condition was not satisfied for the generated waves.

9.2 Wave Spectrum

Based on the dissatisfaction of the deep water condition, 8 smaller scale waves were proposed, to investigate the performance of relevant ocean waves at a relevant scale. The spectrum of waves were selected by means of real wave data. Only the wavemaker movement was adapted to fit the smaller waves. The mesh was not adapted, which resulted in observable mesh dependent results for the smallest waves. No conclusive arguments could be provided about the scaling effects due to insufficient cell sizes. However, it was found that the reflection is wave dependent, and that longer waves typically have more reflection. This largely due to the length of the beach, which was found to be shorter than half the wavelengths for the longer waves, which restricts the amount of possible wave absorption. Similar to the intermediate results, it was found that a partial standing wave is formed with a wavelength of half the generated wave's wavelength. It was also concluded that the average wave height, as well as the determined incident wave height $A1$ were lower than the theoretical value. The two exceptions to this observation were found to have a deviating partial standing wave phase from the other cases.

9.3 Reflection Mitigation

In order to investigate the effectiveness of a foam layer to reduce the reflection, 5 cases were analyzed. Between cases, the foam layers' denseness and thickness were altered. First of all, it was shown that the reflection coefficient was reduced significantly with the introduction of foam layers. It was observed that the reflection reduces with increasing denseness, however it was hypothesized that an optimal denseness exists. Furthermore, it was found that a thicker layer reduces the reflections more when compared to the base layer. The reflection was still present in the form of a partial standing wave, however for the densest case, it was observed that its shape was distorted, presumably due to other effects introduced by the foam layer. It was observed that the average wave amplitude as well as the determined incident wave amplitude $A1$ increase with better reflection mitigation. It was concluded that the reflection not only generates a partial standing wave, but also suppresses the wave amplitude altogether. This also explains the discrepancy between wavemaker theory and the observed average amplitude in the previous results. However, a trend was found where the average amplitude exceeds the theoretical wave amplitude for zero reflection. It was hypothesized that this is due to the asymmetrical movement of the wavemaker, whereas theory is based on a symmetrical movement. The observed average amplitude for the case where thickness was altered was found to deviate from

the trend observed in the other cases. Notably, the partial standing wave for this case was also phase shifted with half a wavelength. Together with previous cases, it was hypothesized that the average wave amplitude is dependent on the phase of the formed partial standing wave. Additionally, it was found that the partial standing wave phase was shifted towards the wavemaker for increasingly denser foams.

9.4 Final Conclusion

In this thesis, it was found that the reflection of the incident propagating wave is reflected back at the beach, forming a partial standing wave for every relevant wave modelled in this research. Moreover, it was found that the reflection suppresses the average wave amplitude significantly. The reflection was found to be wave dependent, and increasing with larger wavelengths due to the length of the beach. The mitigation of reflection can be improved with the introduction of thick, dense foam layers which slow down the waves at the end of the wave tank.

By means of the observations and conclusions made in this thesis, a few statements can be made about the ability of the Ocean Grazer's experimental wave tank to create an adequate environment for future validation and testing experiments. First of all, the flap wavemaker that is present is ideal for the generation of deep water waves. However, the depth of the wave tank that is currently used ($0.9m$), is not sufficient to generate waves at relevant scales that satisfy the deep water condition. Moreover, the beach length is insufficient for the optimal absorption of relevant long period waves, however this limitation could be mitigated with the introduction of denser foam layers. Unfortunately, no conclusion can be made on the scaling effects, however it is recommended to perform experiments on the largest possible scale in any case.

For future experiments, it is recommended to take the limitations of the wave tank into account. Wavemaker theory can be used to configure the wavemaker to approximate the desired waves, however fine tuning is still recommended. A few adaptations could be considered to improve the performance of the wave tank. First of all, it should be considered to increase the depth of the wave tank, in order to satisfy the deep water condition more easily. Moreover, the inclination of the beach should be decreased in order to increase the effective length of the beach, in order for it to perform optimally. In order to decrease the reflection and thus the generation of a partial standing wave, the application of a denser, and possibly thicker foam layer should be considered. Finally, the total length of the wave tank could be drastically increased to gain the ability to generate a few freely propagating waves to perform experiments on. The length increase should include around ten wavelengths of the longest desired waves.

References

[1] A. Vakis, H. Meijer and W. Prins, "First Steps in the Design and Construction of the Ocean Grazer", *Dynamics, Vibration and Control; Energy; Fluids Engineering; Micro and Nano Manufacturing*, vol. 2, 2014.

[2] N. Kularatna, *Energy storage devices for electronic systems.* London, UK: Elsevier, 2015.

[3] A. Bechlenberg, "Performance Analysis and Comparison of the Floater Arrays in the Ocean Grazer 3.0 Design", Bachelor Thesis, University of Groningen, Groningen, 2018.

[4] J. Brenes, "Energy Extraction Analysis of the MP2PTO System and Floater Blanket of the Ocean Grazer WEC", Master Thesis, Rijksuniversiteit Groningen, Groningen, 2017.

[5] M. Manresa, "Analysis and comparison of wave energy extraction in the Ocean Grazer's wave tank experimental setup", Master Thesis, Rijksuniversiteit Groningen, Groningen, 2017.

[6] L. Holthuijsen, *Waves in oceanic and coastal waters.* Cambridge: Cambridge University Press, 2015.

[7] "Wave characteristics review", Khan Academy. [Online]. Available: https://www.khanacademy.org/science/high-school-physics/waves-and-sound/wave-characteristics/a/wave-characteristics-review-ap-physics-1. [Accessed: 15-Jan-2021].

[8] Y. Yang and S. Kwon, "Prediction for Irregular Ocean Wave and Floating Body Motion by Regularization: Part 1. Irregular Wave Prediction", *Transactions of FAMENA*, vol. 40, no. 4, 2016.

[9] W. Munk, *Origin and Generation of Waves.* Ft. Belvoir: Defense Technical Information Center, 1951.

[10] "Wave Generators", *Edinburgh Designs*, 2021. [Online]. Available: http://www4.edesign.co.uk. [Accessed: 28- Apr- 2021].

[11] N. Gao, J. Yang, W. Zhao and X. Li, "Numerical simulation of deterministic freak wave sequences and wave-structure interaction", *Ships and Offshore Structures*, vol. 11, no. 8, pp. 802-817, 2015.

[12] F. Ursell, R.G. Dean, Y.S. Yu. "Forced small-amplitude water waves: a comparison of theory and experiment", *J Fluid Mech.* vol. 7 no. 1, pp. 33–52, 1960.

[13] X. Ni, W. Feng, S. Huang, Y. Zhang and X. Feng, "A SPH numerical wave flume with non-reflective open boundary conditions", *Ocean Engineering*, vol. 163, pp. 483-501, 2018.

[14] R. Dean and R. Dalrymple, *Coastal processes with engineering applications.* Cambridge: Cambridge University Press, 2002.

[15] B. Holmes, "Tank Testing of Wave Energy", EMEC: European Marine Energy Centre [Online]. Available: http://www.emec.org.uk/tank-testing-of-wave-energy-conversion-systems/.

[16] M.J.J. Bögels. "Validating floater blanket models for the Ocean Grazer", Bachelor Thesis, Rijksuniversiteit Groningen, Groningen, 2017.

[17] O. Reynolds, "On the Dynamical Theory of Incompressible Viscous Fluids and the Determination of the Criterion", *Philosophical Transactions of the Royal Society of London A*, vol. 186, pp. 123–164, 1895.

[18] P. Higuera, olaFlow: CFD for waves, 2017.

[19] R. Courant, K. Friedrichs and H. Lewy, "On the Partial Difference Equations of Mathematical Physics", *IBM Journal of Research and Development*, vol. 11, no. 2, pp. 215-234, 1967.

[20] "Courant number in CFD", IdealSimulations, 2021. [Online]. Available: https://www.idealsimulations.com/resources/courant-number-cfd/. [Accessed: 20- May- 2021].

[21] P.Y. Chou, "On velocity correlations and the solutions of the equations of turbulent fluctuation", *Quarterly of Applied Mathematics*, vol. 3, pp. 38-54, 1945.

[22] P. Higuera, "Application of Computational Fluid Dynamics to Wave Action on Structures", doctoral dissertation, Universidad de Cantabria, 2015.

[23] F. Menter, "Two-equation eddy viscosity turbulence models for engineering applications", *AIAA Journal*, vol. 32, pp. 1598-1605, 1953.

[24] F. Engelund, "On the laminar and turbulent flow of ground water through homogeneous sand", *Transactions of the Danish Academy of Technical Sciences*, vol. 3, 1953.

[25] M. del Jesus, *Three-dimensional interaction of water waves with maritime structures*, PhD, University of Cantabria, 2011.

[26] S. Berg, A. Cense, J. Hofman and R. Smits, "Two-Phase Flow in Porous Media with Slip Boundary Condition", *Transport in Porous Media*, vol. 74, no. 3, pp. 275-292, 2008. [Accessed 9 June 2021].

[27] L. Huang, K. Ren, M. Li, Ž. Tuković, P. Cardiff and G. Thomas, "Fluid-structure interaction of a large ice sheet in waves", *Ocean Engineering*, vol. 182, pp. 102-111, 2019.

[28] M. Visser, "Wave tank experiments on the prototype of the floater blanket", Bachelor Thesis, Rijksuniversiteit Groningen, 2016.

[29] A. Rabinovich, "Seiches and Harbor Oscillations", *Handbook of Coastal and Ocean Engineering*, pp. 243-286, 2017.

[30] "What is a seiche?", Oceanservice.noaa.gov, 2021. [Online]. Available: https://oceanservice.noaa.gov/facts/seiche.html. [Accessed: 14- Jun- 2021].

[31] M. Longuet-Higgins, "Mass transport in water waves", *Philosophical Transactions of the Royal Society of London. Series A, Mathematical and Physical Sciences*, vol. 245, no. 903, pp. 535-581, 1953.

[32] S. Schipper, "The Influence of a Transmission System on the Ocean Grazer Wave Energy Converter Performance", Bachelor Thesis, Rijksuniversiteit Groningen, Groningen, 2021.

[33] V. Michalcová and K. Kotrasová, "The Numerical Diffusion Effect on the CFD Simulation Accuracy of Velocity and Temperature Field for the Application of Sustainable Architecture Methodology", *Sustainability*, vol. 12, no. 23, p. 10173, 2020.

Appendix A: Wavemaker Theory MATLAB Script

The wavemaker theory script takes full scale wave properties as input, as well as the desired scale and water depth. Based on those parameters, it will scale the waves and calculate the wavemaker angle and period based on the desired waves. Additionally, the script provides the wavemaker stroke, expected wavelength, wave amplitude and celerity of the wave.

```
clear all

%Real wave data (1:1)
H_real = 2; %waveheight in m
T_real = 5; %Period in s
scale = 70; %Scaling (1:x)

%Experiment data
d = 0.9; %water depth in wavetank in m
wavemaker = 1; %wavemaker type; 1 = flap, 0 = piston

%Calculations
H_exp = H_real/scale;
T_exp = 1/sqrt(scale) * T_real;
omega = 1/T_exp * 2 * pi;
g = 9.81;
xlim = [0, T_exp];
alpha = (omega^2 * d/g);
beta = alpha*((tanh(alpha))^(-1/2));
kd = (alpha + beta^2 * (cosh(beta))^(-2))/(tanh(beta)+beta*(cosh(beta))
    ^(-2)); %approximation of the wavenumber as a function of the period
    and the depth, as a result of the dispersion relation

if wavemaker == 1 %flap wavemaker
     Tr = 4 * sinh(kd)/kd * (kd * sinh(kd) - cosh(kd) + 1)/(sinh(2*kd)+2*
        kd); %transfer function H/S
     S = H_exp/Tr;
angle = atand((S/2)/d); %amplitude of wavemaker oscillation in degrees
wavemaker_func = @(t) angle * sin(2*pi/T_exp * t); %wavemakermovement
    over time in degrees
c = g/omega * tanh(kd); %celerity
lambda = c*T_exp; %wavelength in m
d_rel = d/lambda; %relative depth

sprintf("The flap wavemaker should move with T=%0.3f seconds, with a
    wavemaker stroke of %0.3f meters (angle amplitude of %0.3f degrees),
    which should produce waves of H=%0.3f meters", T_exp, S, angle, H_exp)
sprintf("The phase velocity (celerity) equals %0.3f m/s, with a
    wavelength of %0.3f m. The relative depth is %0.3f. (Should be >0.5
    for deep water)", c, lambda, d_rel)

```

```
34
35 fplot(wavemaker_func, xlim)
36 title("wavemaker movement to produce scaled waves")
37 xlabel("time (s)")
38 ylabel("angle (degrees)")
39
40 elseif wavemaker == 0 %pistonwavemaker
41     Tr = 2 * (cosh(2*kd) - 1)/(sinh(2*kd) + 2*kd); %transfer function H/S
42     S = H_exp/Tr %Stroke in m
43 else
44     print("wavemaker must be either 0 (piston) or 1 (flap)")
45 end
```

Appendix B: Wave Spectrum Evaluation MATLAB Script

```
1  close all
2
3  %Inputs
4  %Make sure to input your .csv via "Home" -> "Import Data"
5  avgSE = 0; %Average Surface Elevation in the data file in simulation
       units (mm, cm, m)
6  starttime = 30; %starttime in seconds
7  endtime = 50; %endtime in seconds
8  timestep = 0.1; %timestep in seconds
9  samplingrate = 1.0697*62.7; %sampling rate in Hz for the FFT Spectrum
10
11 period = 1.62; %period in seconds
12 cols = 85;
13 noperiods = 3;
14 Hth(1, 1:60)=0.05;
15 Hemp(1, 1:60)=0.04;
16
17
18 SE = wavedata(2:(500*cols +1), 1:cols); %Filename(rows, columns)
19 SE = table2array(SE);
20 SEsize = size(SE);
21 columns = SEsize(2);
22 for i=1:columns
23 SE_rev(:, i) = rmmissing(SE(:, i));
24 end
25 SE_rev2 = SE_rev(300:500, [1 12 23 34 45 56 67 78 cols 2:11 13:22 24:33
       35:44 46:55 57:60]);
26 columns = 60;
27 for n=1:columns
28 for j=1:(endtime-starttime)/period
29 SE_list(j, n) = max((SE_rev2(round((j-1)*(1/timestep*period))+1:round(j
       *(1/timestep*period)), n)));
```

```
30 end
31
32
33 avg_SE(n) = mean(SE_list(:, n));
34 max_SE(n) = max(SE_list(:, n));
35 min_SE(n) = min(SE_list(:, n));
36
37 end
38
39
40
41
42 avg_WT = avg_SE(:, 1:columns);
43 max_WT = max_SE(:, 1:columns);
44 min_WT = min_SE(:, 1:columns);
45 avgavg_WT = mean(avg_WT(:));
46
47
48 Havg(1, 1:60)=avgavg_WT;
49
50 figure(1)
51 xdistwt = [0.1:0.1:6.0];
52 xdistth = [0.1:0.1:6.0];
53 plot(xdistwt, avg_WT)
54 hold on
55 plot(xdistwt, max_WT)
56 hold on
57 plot(xdistwt, min_WT)
58 hold on
59 plot(xdistth, Hth, 'k')
60 hold on
61 plot(xdistth, Hemp, 'm')
62 hold on
63 plot(xdistwt, Havg, 'g')
64 title("Thicker")
65 %ylim([0.0008 0.02])
66 xlabel('Position in Wave Tank(m)')
67 ylabel('Wave Amplitude (m)')
68 legend('Averaged over all periods', 'Maximum', 'Minimum', 'Theoretical',
      'Empirical','Total average')
69 amplitudes = sort(avg_WT, 'descend');
70 A_high = sum(amplitudes(1:noperiods))/noperiods;
71 A_low = sum(amplitudes(end-(noperiods-1):end))/noperiods;
72 A1 = (A_high + A_low)/2;
73 A2 = (A_high - A_low)/2;
74 R = A2/A1
75
```

```
steps = (endtime-starttime)/timestep;
FFT = fft(SE_rev(:, 45));
P = abs(FFT/steps);
Y = P(1:steps/2+1);
Y(2:end-1) = 2*Y(2:end-1);
X_Hz = (samplingrate*(0:(steps/2))/(steps*10));
X_T = X_Hz;
figure(2)
plot(X_T, Y)
title(sprintf('Single-Sided Amplitude Spectrum of X(t) at 4m'))
xlabel('f[Hz]')
ylabel('|Y(f)|')
```

Appendix C: Surface Elevation and FFT Plot MATLAB Script

```
close all

%Inputs
%Make sure to input your .csv via "Home" -> "Import Data"
avgSE = 0; %Average Surface Elevation in the data file in simulation
    units (mm, cm, m)
starttime = 30; %starttime in seconds
endtime = 50; %endtime in seconds
timestep = 0.1; %timestep in seconds
datarows = (((starttime/timestep)+(1-(starttime/timestep))):(endtime/
    timestep)); %Leave this unchanged, it prepares row extraction from the
     datafile
datacolumns = [1:34]; %Indicate which columns contain the Surface
    Elevation data
SE = wavedata(2:30601, datacolumns); %Filename(rows, columns)
samplingrate = 1.0697*62.7; %sampling rate in Hz for the FFT Spectrum



%tableformatter
datasize = size(SE);
steps = (endtime-starttime)/timestep;
SE = table2array(SE);
SE = SE - avgSE;
cs = [18 19:34 17 16 15 14 13 12 11 10 9 8 7 6 5 4 3 2 1];
SE_rev = zeros(900, 32);
for i = 1:34
SE_rev (1:900, i) = SE(((i-1)*900+1):(i*900), cs(i));
end
SE_rev(starttime*10:endtime*10, 1:34) = SE_rev(starttime*10:endtime*10,
    [2:16 34 33 32 31 30 29 28 27 26 25 24 23 22 21 20 19 18 17 1]);
SE_rev2 = SE_rev(starttime*10:endtime*10, 1:32);
columnselect = [1:32];
```

```
typeinfo = ["Wavetank" "Absorption tank"];
posinfo = ["x=0.5m", "x=1m", "x=1.5m", "x=2m", "x=2.5", "x=3m", "x=3.5",
    "x=4m", "x=4.5" "x=5m", "x=5.5", "x=6m", "x=6.5", "x=7", "x=7.5", "x
    =8"];
for n = 1:2
for i = 1:16
time = (starttime:0.1:endtime);
figure(i+(n-1)*16)
subplot(2,1,1)
plot(time, SE_rev(starttime*10:endtime*10, i+(n-1)*16));
title(sprintf('Surface Elevation over time at %s', posinfo(i)))
xlabel('Time (t)')
ylabel('Surface Elevation')
hold on

FFT = fft(SE_rev(:, (i+(n-1)*16)));
P = abs(FFT/steps);
Y = P(1:steps/2+1);
Y(2:end-1) = 2*Y(2:end-1);
X_Hz = (samplingrate*(0:(steps/2))/(steps*10));
X_T = X_Hz;
subplot(2,1,2)
plot(X_T, Y)
title(sprintf('Single-Sided Amplitude Spectrum of X(t) at %s', posinfo(i)
    ))
xlabel('f[Hz]')
ylabel('|Y(f)|')



for j=1:(endtime-starttime)/1.62
SE_list(j, i+(n-1)*16) = max((SE_rev2(round((j-1)*16.2)+1:round(j*16.2),
    (i+(n-1)*16))));
end


avg_SE(i+(n-1)*16) = mean(SE_list(:, i+(n-1)*16));
max_SE(i+(n-1)*16) = max(SE_list(:, i+(n-1)*16));
min_SE(i+(n-1)*16) = min(SE_list(:, i+(n-1)*16));

end
end

avg_WT = avg_SE(:, 1:16);
avg_AT = avg_SE(:, 17:32);
max_WT = max_SE(:, 1:16);
max_AT = max_SE(:, 17:32);
```

```
72 min_WT = min_SE(:, 1:16);
73 min_AT = min_SE(:, 17:32);
74 avgavg_WT = mean(avg_WT(:));
75 avgavg_AT = mean(avg_AT(:));
76
77 figure(35)
78 xdistwt = [0.5:0.5:8];
79 plot(xdistwt, avg_WT)
80 hold on
81 plot(xdistwt, max_WT)
82 hold on
83 plot(xdistwt, min_WT)
84 title("Partial Standing Wave Amplitude in Wavetank")
85 ylim([0 0.08])
86 xlabel('x(m)')
87 ylabel('Wave amplitude(m)')
88 legend('average', 'maximum', 'minimum')
89
90 figure(36)
91 xdistat = [0.5:0.5:8];
92 plot(xdistat, avg_AT)
93 hold on
94 plot(xdistat, max_AT)
95 hold on
96 plot(xdistat, min_AT)
97 title("Partial Standing Wave Amplitude in Absorption Tank")
98 ylim([0 0.08])
99 xlabel('x(m)')
100 ylabel('Wave amplitude(m)')
101 legend('average', 'maximum', 'minimum')
102
103 amplitudes = sort(avg_WT, 'descend');
104 A_high = sum(amplitudes(1:3))/3;
105 A_low = sum(amplitudes(end-3:end))/3;
106 A1 = (A_high + A_low)/2;
107 A2 = (A_high - A_low)/2;
108 R = A2/A1
```